Investigations of nanocarbons and other inorganic nanomaterials

A thesis submitted in partial fulfillment
for the degree of

Master of Science

as a part of the

Integrated Ph. D. programme
(Materials Science)

by

Urmimala Maitra

Chemistry and Physics of Materials Unit
Jawaharlal Nehru Centre for Advanced Scientific Research
(*A Deemed University*)
Bangalore, India.

May 2010

Dedicated to my family

DECLARATION

I hereby declare that the matter embodied in this thesis entitled "***Investigations of nanocarbons and other inorganic nanomaterials***" is the result of investigations carried out by me under the supervision of Prof. C. N. R. Rao, FRS at the Chemistry and Physics of Materials Unit, JNCASR, Bangalore, India and that it has not been submitted elsewhere for the award of any degree or diploma.

In keeping with the general practice in reporting scientific observations, due acknowledgement has been made whenever the work described is based on the findings of other investigators.

_____

(Urmimala Maitra)

CERTIFICATE

I hereby certify that the matter embodied in this thesis entitled **"*Investigations of nanocarbons and other inorganic nanomaterials*"** has been carried out by Ms. Urmimala Maitra at the Chemistry Physics and Materials Unit, Jawaharlal Nehru Centre for Advanced Scientific Research, Bangalore, India under my supervision and it has not been submitted elsewhere for the award of any degree or diploma.

_____

Prof. C. N. R. Rao

(Research Supervisor)

Acknowledgements

At the very onset, I take my opportunity to express my deep sense of gratitude to Prof. C. N. R. Rao, FRS, my research supervisor, for introducing me to this fascinating field of Nanoscience. It was he whose enthusiasm (his age notwithstanding), instigated in me the desire to pursue science and has continued to inspire me ever since. His innovative ideas and ability to handle any problem in the simplest of the ways has been the strength behind the completion of this work. I shall remain ever indebted to him for bearing with me throughout the course of the work. It has been a fulfilling experience to work under his encouraging and full spirited guidance.

My sincere thanks to my collaborators Prof. U. Ramamurthy and Dr.T. Govindaraju for valuable discussions and help during the course of the experiments.

I use this opportunity to thank Dr. A. Govindaraj for helping me in innumerable ways in experimental and official work.

I shall remain ever thankful to all my seniors specially Sandeep, Claudy, Ramakrishna, Leela, Rakesh, Kalyan, Dinesh, Pranab for their valuable suggestions. It has been a wonderful experience working with all my labmates namely Neenu, Anupama, Bhatt, Subbu, Basant, Beloo, Dr. Prashant, Dr. Late, Dr. Angshuman, Joyti, Ajmala, Dr. Sudarayya, Dr. Vivekchand.

My work would have been incomplete without Gomati, Dr. Kanishka, Barun and K. Eswar (Mater. Eng. Dept. IISc) who helped me with different problems. Special thanks to them all.

I would like to thank Mrs. Rao for her high encouraging words and hospitality.

I thank the following faculties namely Prof. G. U. Kulkarni, Prof. S. Balasubramanian, Prof. A. Sundaresan, Prof. S. M. Shivaprasad, Prof. N. Chandrabhas, Dr. T. K. Maji, Dr. Eswaramoorthy and Prof. K. S. Narayan of CPMU, Dr. T. Govindaraju and Dr. S. J. George of NCU, Prof. S. K. Pati, Prof. Umesh V. Waghmare, Dr. S. Narasimhan and Dr. N. S. Vidhyadhiraja of TSU and Prof. S. Ranganathan of Materials Engineering(IISc) for their courses.

I thank the timely help of the technical staff namely Ms. N. R. Selvi (for FESEM), Mrs. T. Usha (for TEM), Mr. Vasu (for UV, PL, IR, TGA), Mr. Anil (for XRD), Mr. Srinath, Mr. Srinivasa Rao and Mr. Srinivas (for technical assistance). The assistance provided by Mr. Arokianathan and Mr. Moorthy is also appreciated.

I thank JNCASR and IISc for extending course work and research facilities.

Thanks to all my Int. PhD. batch mates and all my friends specially Datta, Saikrishna, Ankita, Dhiraj, Dinesh (EMU) whose refreshing company I have always cherished.

Finally I thank my family. It was my father who inculcated in me the love for science. But for him I would not have been here. Thanks to my mother and grandmother who are always ready with their encouraging words and definitely to my sister time spent with whom is the best time of my life. Thank you all for being what you are. This thesis is a humble offering to you.

PREFACE

Materials when reduced to nanoregime they start behaving differently from what they are in bulk; nanotechnology and science of nanomaterials thus attract a whole lot of attention. This thesis consists of seven chapters covering study of various properties of some nanomaterials. Chapter 1 presents a brief overview of inorganic nanomaterials with various aspects of synthesis, shape and size control and properties.

Chapter 2 deals with solubilization of nanodiamond by functionalization. We were able to get stable dispersions of nanodiamond in organic solvents by covalently functionalizing with organosilane and organotin or with long chain aliphatic amine through amide derivatization and in water by noncovalently functionalizing with surfactants.

In Chapter 3 we investigated mechanical properties of polymer nanocomposites containing single or two nanocarbons as nanofillers. Mechanical properties of composites with binary combinations of nanocarbons exhibited extraordinary synergy suggesting new ways of designing advanced materials incorporating more than one nanomaterial.

Study of surface-enhanced Raman scattering of adsorbed molecules on films of Au and Ag nanoparticles comprises Chapter 4. These films were produced at the organic-aqueous interface and show good enhancement factors.

We prepared nanocomposites of Au nanoparticles in polymer. Study of scaling behaviour of plasmon coupling with concentration variation is presented in Chapter 5.

In Chapter 6 we demonstrate successful generation of white light using nanoparticles of GaN and ZnO. Produced white light was of good quality and quantum yield.

Chapter 7 deals with work in progress which comprises of two works: first, study of the magnetic properties of thin films of Au nanoparticles formed at the organic-aqueous interface and second, covalently linking two nanocarbons.

Contents

CHAPTER 1

A brief overview of Inorganic nanomaterials

1.1. Perspective:

The word `nano' is derived from the Greek `nanos' or Latin `nanus', meaning "dwarf" and thus refers to something small. The term nanoscience is employed to describe creation and exploitation of materials with dimensions between atoms and bulk materials. Nanomaterials are materials with atleast one dimension in the nanometre (1nm = 10^{-9} m) range. Confining materials to such small dimension causes them to exhibit properties quite different from the bulk. Quantum phenomena begin to play its role and several new phenomenon and properties begin to appear. Suitable control of the properties of nanometer-scale structures can lead to new science as well as new products, devices and technologies.

Bulk shiny yellow gold when reduced to nanoregime loses its shine as well as yellow colour. It can then be used to produce any colour brown, burgundy, red, purple or blue. In as early as 4 AD Romans made the 'Lycrus cup' impregnated with Au and Ag nanoparticles that appeared red in transmitted light and green in reflected light. Tinted glasses that decorated ceilings of medieval century churches also used Au nanoparticle, only the phenomenon was not understood. The foundation of modern colloidal science was laid down by Michael Faraday [1]. He established that several dyes were indeed made of metal particles. After a thorough study of gold sols, Faraday concluded *". . . the gold is reduced in exceedingly fine particles which becoming diffuse, produce a beautiful fluid. . . the various preparations of gold, whether ruby, green, violet or blue. . . consist of that substance in a metallic divided state"* [2] . At its inception, the

science of colloids did not quite catch popular fancy. It remained the domain of a few individuals. For example, Ostwald's 1915 book on colloids is titled "The world of neglected dimensions" [3]. Thus successful predictions of optical properties and electronic structure of metal particles by Mie [4], Gans [5, 6] and Kubo [7] and Einstien's success in relating Brownian motion to diffusion coefficient [8] were largely ignored. It was Feyman who gave the essential idea when he stated "*There is Plenty of room at the bottom*" [9] and thus heralded a gradual revival of the science of colloids in 1980s which soon became popular as nanoscience. Nanomaterial research was initially motivated by an effort to understand the evolution of bulk structural and electronic properties from molecular scale. The past couple of decades have witnessed an exponential growth of activities in this field worldwide, driven both by the excitement of understanding new science and by the potential hope for applications and economic impacts.

Table 1.1 Examples of nanomaterials of different dimensionalities:

	Size (appox.)	***Materials***
0D-Nanocrystals and clusters (quantum dots)	Diam 1-10 nm	Metals, semiconductors, magnetic materials
Other nanoparticles	Diam 1-100 nm	Ceramic oxides
1D-Nanowires	Diam 1-100 nm	Metals,semiconductors,oxides,sulphides,nitrides
Nanotubes	Diam 1-100	Carbon, Layered metal chalcogenides.
Nanoporous solids	Pore diam 0.5-10 nm	Zeolites, phosphates etc.
2-D arrays of nanoparticles	Several nm^2- μm^2	Metals,semiconductors, magnetic materials.
Surfaces and thin flims	Thickness 1-1000nm	Variety of materials
3-D structures and superlattices	Several nm in three dimensions	Metals, semiconductors, magnetic materials.

Nanomaterials are defined based on their dimensionalities as ***(3-n)*** dimensional where ***n*** defines the number of dimensions in nano-regime. Accordingly nanomaterials are 0D (nanocrystals; n=3), 1D (nanorods, nanotubes; n=2) and 2D (nanofilms amd nanowalls; n=1). Table 1.1 lists the typical nanomaterials of different dimensions [10].

Much of the fascination in nanoscience is due to the fact that nanocrystals and other nano-objects such as tubes and wires possess properties that depend on the size of the system. Size plays a crucial role in determining the electronic, chemical, optical and magnetic

properties of nanomaterials. Nanocrystals measure a few nanometres in diameter and could contain up to few hundred of atoms. Electrons suffer quantum confinement in such small clusters and cause the nanocrystal to behave in a manner distinct from both the constituting atoms and the corresponding bulk. Moreover because of such small sizes they possess high surface to volume ratio, (which can reach upto 0.9 for a 1nm) which considerably alters their properties. Several innovative methods for the synthesis of nanoparticles and nanotubes and their assemblies, are now available. There is a better understanding of the size-dependent electrical, optical and magnetic properties of individual nanostructures of semiconductors, metals and other materials. Besides the established techniques of electron microscopy, crystallography and spectroscopy, scanning probe microscopes have provided powerful tools for the study of nanostructures. Novel methods of fabricating patterned nanostructures, as well as new device and fabrication concepts, are constantly being discovered. Nanostructures have also been ideal for computer simulation and modelling, their size being sufficiently small to accommodate considerable rigour in treatment. In computations on nanomaterials,[11] one deals with a spatial scaling from 1 A° to 1 μm and temporal scaling from 1 fs to 1 s, the limit of accuracy going beyond 1 kcal mol^{-1}.

1.2. Synthetic Strategy :

The largest activity in this field for the last two decades has been in the synthesis of new nanomaterials of different sizes and new shapes. In general nanomaterials can be synthesized by two approaches: by continuous division of matter in bulk (top down) and by controlled growth of constituents starting from atoms (bottom up). While nanomaterials have been generated by physical methods such as laser ablation, arc-discharge and evaporation, chemical methods have proved to be more effective, as they provide better control as well as enable different sizes, shapes and functionalization.
Chemical growth of particles be it bulk or nano, involves precipitation of solid phase from solution. Process of precipitation basically consists of nucleation followed by growth stages. Nucleation can be of three types: homogenous, heterogeneous and

secondary. Homogenous nucleation occurs in absence of solid interface, by the driving force of thermodynamics. The free energy change for nucleation is given by,

$$\Delta G = -\frac{4}{V}\pi r^3 k_B T \ln(S) + 4\pi r^2 \gamma \quad (1)$$

and by equating ΔG=0;

$$r* = \frac{2V\gamma}{3k_B T ln(S)} \quad (2)$$

where, V is the molecular volume of the precipitated species, r is the radius of the nuclei, r^* the critical radius, k_B is the Boltzmann constant, S is the saturation ratio and γ is the surface free energy per unit surface area. For a given value of S, all particles with $r > r^*$ will grow and all particles with $r < r^*$ will re-dissolve. From the above equation, it follows that the higher the saturation ratio S, the smaller the critical nuclei size r^* is (Fig. 1.1).

When the concentration drops below the critical level, nucleation stops and the particles continue to grow by molecular addition until the equilibrium concentration of the precipitated species is reached. Uniformity of the size distribution is achieved through a short nucleation period that generates all of the particles obtained at the end of the reaction followed by a self-sharpening growth process. At this stage, the smaller particles grow more rapidly than the larger ones because the free energy driving force is larger for smaller particles than for larger ones. Nearly monodisperse size distribution can be obtained at this stage by either stopping the reaction (nucleation and growth) quickly or by supplying reactant source to keep a saturated condition during the course of the reaction [12].On the other hand, when the reactants are depleted due to particle growth, Ostwald ripening or defocusing will occur, where the larger particles continue to grow and the smaller ones get smaller and finally dissolve. Because the saturation ratio (S) decreases now and the corresponding critical nuclei size (r^*) increases and any particles smaller than this new critical size will dissolve. If the reaction is quickly stopped at this stage, the particles will have a broad size distribution, which is featured by a distribution centering two size regimes, bigger ones and smaller ones [14, 15]. Other way of growth is growth by molecular addition in which soluble species grows on solid particles by aggregation (secondary growth). This generally leads to a greater size distribution.

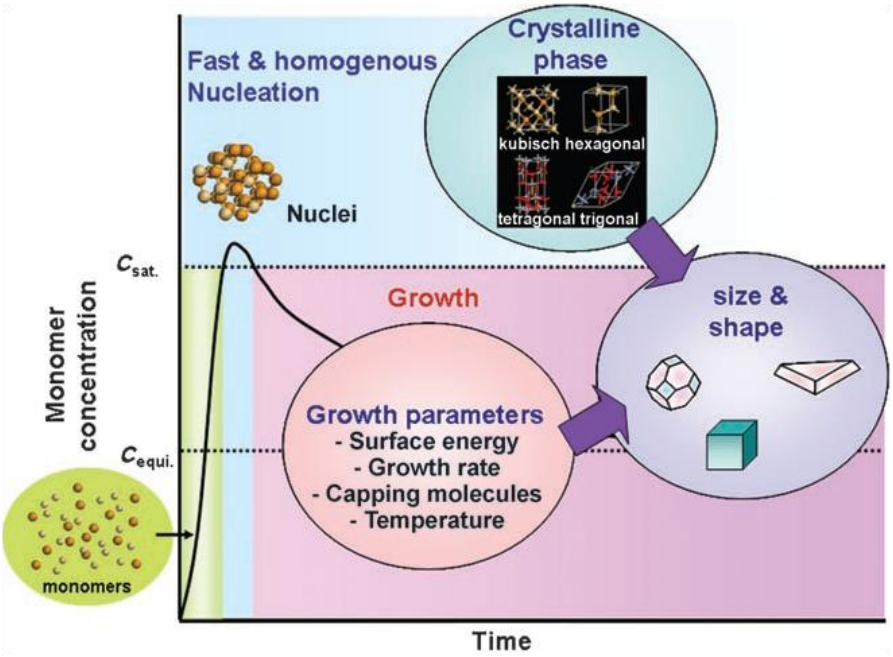

Figure 1.1 Crystal-growth diagram. When the monomer concentration reaches a super-saturation level, seed nucleation occurs and then monomer continuously aggregates onto the seeds, which results in the gradual decrease of monomer concentration. During these nucleation and growth stages, the control of growth parameters and crystalline phase is critical in determining the final size and shape of nanocrystals. Csat.=saturation concentration, Cequi.=equilibrium concentration. (From [13])

Nanoparticles are small and are not thermodynamically stable for crystal growth kinetically. To finally produce stable nanoparticles, these nanoparticles must be arrested during the reaction either by adding surface protecting reagents, such as organic ligands or inorganic capping materials, or by placing them in an inert environment such as an inorganic matrix or polymers. The nanocrystal (NC) dispersions are stable if the interaction between the capping groups and the solvent is favourable, providing an energetic barrier to counteract the van der Waals attractions between nanoparticles. To help arrest these nanoparticles, different solvents are also used to change the solubility or the reaction rate [16, 17, 18].

1.2.1 Synthetic Routes:

(A) Sol Process:

As discussed above general scheme for preparing monodisperse nanostructures require a single, temporally short nucleation event followed by slower

growth on the existing nuclei [19]. This may be achieved by rapid addition of reagents into a reaction vessel containing a hot, coordinating solvent. Rapid addition of reagents to the reaction vessel raises the precursor concentration above the nucleation threshold. If the temperature of the solution is sufficient to decompose the reagents, a supersaturation of particles in solution occurs. Upon a short nucleation burst, the concentration of these species in solution drops below the critical concentration for nucleation. Consumption of the reactants then occurs by the growth of the particles. Initial size distribution is largely determined by the time over which the nuclei are formed and begin to grow. If the time of nanoparticle growth during the nucleation period is short compared to the subsequent growth processes, the nanoparticles can become more uniform over time as size focusing takes place [19, 20, 21].

(B) Micelles:

When the surfactant concentration exceeds the critical micelle concentration (cmc) in water, micelles are formed as aggregates of surfactant molecules. In normal micelles, the hydrophobic hydrocarbon chains of the surfactants are oriented toward the interior of the micelle and the hydrophilic groups of the surfactants are in contact with the surrounding aqueous medium. On the other hand, reverse micelles are formed in non-aqueous medium where the hydrophilic head groups are directed toward the core of the micelles and the hydrophobic groups are directed outward. In both cases, the micelles exist only as a small amount of solubilized hydrophobic or hydrophilic material as illustrated in Fig. 1.2. If the concentration of surfactant is increased further the droplet size can be increased and because of this because the inside pool of water or oil is enlarged.

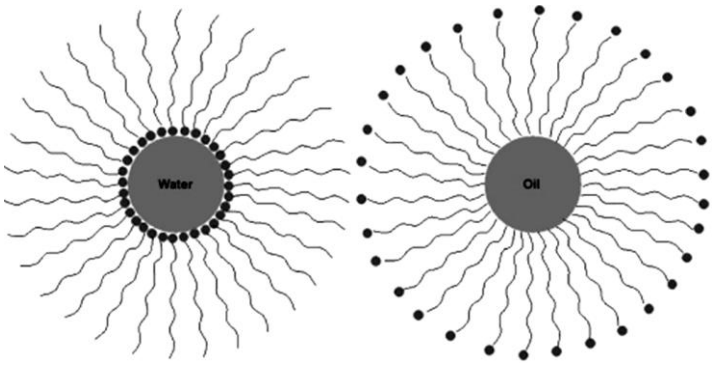

Figure1.2 Reverse micelle and normal micelle structures.

The general method of using reverse micelles to synthesize nanoparticles can be divided into two cases. The first case involves the mixing of two reverse micelles. Due to the coalescence of the reverse micelles, exchange of the materials in the water droplets occurs, which causes a reaction between the cores and nanoparticles are formed in the reversed micelles. The second case involves mixing one reactant that is solubilized in the reversed micelles with another reactant that is dissolved in water. The reaction can take place by coalescence or aqueous phase exchange between the two reverse micelles. For example, Cu nanoparticles are produced using reverse micelles, from copper diethyl sulfosuccinate, $Cu(AOT)_2$, in water-isooctane medium [22] . Two particle sizes could be produced by varying the concentration of surfactants. In contrast with reverse micelles, there is no confinement of reactants. Normal micelles act as a polymer that controls the nanoparticle size. CdS and Cu nanoparticles are successfully produced [23, 24] by using micelles.

(C) Sol-Gel Process:

The sol-gel method is based on inorganic polymerization reactions. The sol-gel process includes four steps: hydrolysis, polycondensation, drying and thermal decomposition. Precursors of the metal or nonmetal alkoxides hydrolyze with water or alcohols according to the hydrolysis process

$$M(OR)_X + m\,H_2O \rightarrow M(OR)_{x-m}.\,(OH)_m + m\,ROH \qquad (3)$$

where, if *m* is up to *x*, the reaction is total hydrolysis, followed by either a water condensation or alcohol condensation and the final equation is,

$$M(OR)_x + \frac{x}{2} H_2O \rightarrow MO_{x/2} + x\,HOR \qquad (4)$$

In addition to water and alcohol, an acid or a base can also help to hydrolyze the precursor. In the case of an acid, a reaction takes place between alkoxide and the acid.

$$\text{-M-OR} + AOH \rightarrow \text{-M-O-A} + ROH \qquad (5)$$

After the solution has been condensed to a gel, the solvent must be removed. Higher temperature calcination is needed to decompose the organic precursor. The size of the sol particles depends on the solution composition, pH and temperature. By controlling these factors, one can tune the size of the particles. This method has been used to

synthesize metal oxide nanostructures, such as TiO_2 [25-30], TnO_2 [31], ZrO_2 [32], SnO_2 [33], ZnO [34] and other nanostructures.

(D) Chemical Precipitation:

The kinetics of nucleation and particle growth in homogeneous solutions can be adjusted by the controlled release of the anions and cations. Careful control of the kinetics of the precipitation can result in monodisperse nanoparticles. It is essential to control the factors that determine the precipitation process, such as the pH and the concentration of the reactants and ions. Organic molecules are often used to control the release of the reagents and ions in the solution during the precipitation process. The particle size is influenced by the reactant concentration, pH and temperature. By engineering these factors nanoparticles of many complex systems with narrow size distributions, such as ZrO_2 [35], $BaTiO_3$ [36, 37], $YBaCu_3O_y$ [38], have been produced.

(E) Solvothermal Synthesis:

This method exploits the solubility of almost all inorganic substances in a solvent mostly water at elevated temperatures and pressures and subsequent crystallization of the dissolved material from the fluid. Solvothermal conditions afford high autogenous pressures inside the sealed autoclave that enable low boiling solvents to be heated to temperatures well above their boiling points. Products obtained are generally crystalline compared to those from other solution based reactions. The properties of the reactants, including their solubility and reactivity, also change at high temperatures. During the synthesis of nanocrystals, parameters such as solvent pressure, temperature, reaction time and the respective precursor product system can be tuned to maintain a high simultaneous nucleation rate and good size distribution as well as tuning of shape and size. Different types of nanoparticles such as TiO_2 [39], $LaCrO_3$ [40, 41], ZrO_2 [42], $BaTiO_3$ [43], $SrTiO_3$ [44], $Y_2Si_2O_7$ [45], Sb_2S_3 [46], CrN [47] and many more have been prepared.

(F) Pyrolysis:

Pyrolysis is a chemical process in which chemical precursors decompose under suitable thermal treatment into one solid compound and unwanted waste evaporates away. Generally, the pyrolytic synthesis of compounds leads to powders with a wide size distribution in the micrometer regime. To get a uniform nanosized material slowing of the reaction rate or decomposition of the precursor in the inert solvent is needed. MCO_3, MC_2O_4, $M(C_2O_2)$, $M(CO)_x$, MNO_3, glycolate, citrate and alkoxides are the common precursors that are used. Poly(vinyl alcohol) (PVA) and poly(ethylene glycol) (PEG) are commonly used as protecting agents. Pyrolysis can be used to prepare different kinds of nanoparticles including metals, metal oxides, semiconductors and composite materials such as Ag [48], Au [49], ZrO_2 [50], Al_2O_3, SnO_2 [51], TiO_2 [52], GaN [53], ZnS [54], $YBa_2Cu_3O_{7-x}$ [55], Ni [56] and carbon nanotubes [57-67]. Thus synthesized carbon nanotubes produced from (organometallic precursors) can be used to further prepare gallium nitride nanowires, silicon nitride nanotubes and boron nitride nanotubes [67-69].

(G) Vapour Deposition:

- **Chemical Vapour Deposition (CVD):**

In CVD, the vaporized precursors are introduced into a CVD reactor and adsorb onto a substance held at an elevated temperature. These adsorbed molecules will either thermally decompose or react with other gases/ vapours to form crystals. The CVD process consists of three steps: (a) mass transport of reactants to the growth surface through a boundary layer by diffusion, (b) chemical reactions on the growth surface and (c) removal of the gas-phase reaction byproducts from the growth surface. Nucleation in the gas phase is homogeneous, whereas nucleation on the substrate is heterogeneous. Catalysts, usually transition metal particles such as Fe, Ni and Co, are also used in the CVD process. Strained-induced Stranski-Krastanow growth is used to produce nanoparticles in the CVD process [70-74].

- **Physical Vapor Deposition (PVD):**

PVD involves condensation from the vapor phase. The PVD process is composed of three main steps: (a) generating a vapor phase by evaporation or sublimation of the material,

(b) transporting the material from the source to the substrate and (c) formation of the particle and/or film by nucleation and growth. Different techniques have been used to evaporate the source such as electron beam, thermal energy, sputtering, cathodic arc plasma and pulsed laser. Si nanowire [75, 76], GeO_2 nanowire [77], ZnO[78] nanorod etc.

1.2.2 Varieties of nanomaterials:

I. Nanocrystals:

(A) Metals:

Metal nanoparticles are generally prepared by reduction of metal salts in solution containing capping agents like PVP. Often solvothermal reaction is carried out in sealed reaction conditions and presence of organic reagents to reduce the possibility of atmospheric oxidation of the nanocrystals. Au nanocrystals of size 10-100 nm have been prepared by addition of choloroauric acid to boiling solution of sodium citrate [79, 80] or citric acid. Smaller 1-2 nm particles are obtained by using milder reducing agents like tetrakis(hydroxymethyl)phosphonium chloride (THPC) [81] . Jana and Peng [82] obtained monodisperse nanocrystals of Au, Cu, Ag and Pt by dispersing metal salts in toluene with the aid of long-chain quaternary ammonium salts and reduced with tetrabutylammonium borohydride. The reaction can be scaled up to produce gram quantities of nanocrystals. Often ionic liquid are used, for eg. Rh and Ir nanoparticles are prepared in t1-n-butyl-3-methylimidazoliumhexafluoro phosphate, in the presence of hydrogen [83]. Bimetallic nanoparticles like FePt [84], AuPt [85] have also been prepared.

(B) Metallic oxides:

Rockenberger *et al.* [86] described the use of cupferron complexes as precursors to prepare γ-Fe_2O_3, Cu_2O and Mn_3O_4 nanocrystals. Nanocrystals of CoO [87], CdO and CuO [88] are prepared by the solvothermal decomposition of metal-cupferronate in presence of trioctylphosphineoxide (TOPO) in toluene. Apart from solvothermal methods, thermolysis of precursors in high boiling solvents, the sol-gel method, hydrolysis and use of micelles have been employed to synthesize the metal oxide

nanocrystals. Thus, Park *et al.* [89] have used metaloleates as precursors for the preparation of monodisperse Fe_3O_4, MnO and CoO nanocrystals.

(C) Metal chalcogenides

Nearly monodisperse Cd-chalcogenide nanocrystals (CdE; E = S, Se, Te) have been synthesized by the injection of organometallic reagents such as alkylcadmium into a hot coordinating solvent in the presence of silylchalcogenides/ phosphinechalcogenides [17, 90]. Fig. 1.3 shows the TEM images of monodisperse CdSe nanocrystals. Organic-soluble CdS, PbS, PbSe nanocrystals are similarly prepared by the reaction of a cadmium salt with S and Se powder in toluene in the presence of tetralin [91, 92]. Homogeneously alloyed CdS_xSe_{1-x} (x = 0-1) nanocrystals are prepared by the thermolysis of metal–oleylamine complexes in the presence of S and Se [93]. Nanocrystals of Ni_3S_4 and $Cu_{1-x}S$ have been prepared by adding elemental sulphur to metal precursors dissolved in dichlorobenzene or oleylamine at relatively high temperatures [94].

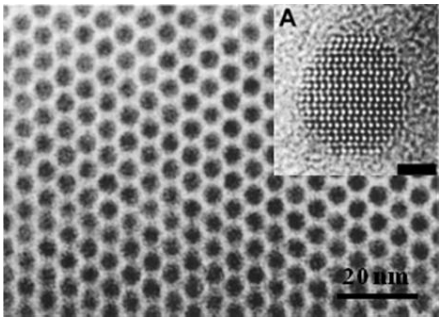

Figure 1.3 TEM image of 4.8 nm CdSe nanocrystals.(Inset) HRTEM image of a <100> oriented CdSe nanocrystals (scale = 1.5 nm) (From [17]).

(D) Metal pnictides:

GaN, AlN and InN nanocrystals of various sizes have been prepared under solvothermal conditions, by employing gallium cupferronate or chloride as the gallium source and 1,1,1,3,3,3-hexamethyldisilazane (HMDS) as the nitriding agent and toluene as solvent [95,96]. By employing surfactants such as cetyltrimethylammonium bromide (CTAB), the size of the nanocrystals could be controlled. Group 13 metal nitrides (GaN, AlN, InN) have also been prepared by a single source precursor route with the precursor as metal chloride-urea adduct. An early procedure for the preparation of phosphides and arsenides of gallium, indium and aluminium involved the dehydrosilylation reaction. Alivisatos and co workers [97] adapted this method to prepare

GaAs nanoparticles using $GaCl_3$ and $As(SiMe_3)_3$ in quinoline. Using a similar scheme, GeSb, InSb, InAs and InP nanocrystals were obtained [98].

(E) Core@shell nanocrystals

Core@shell particles involving two different materials forming the core and the shell have been investigated widely to tune various optical and other properties or combine more than one unrelated property in one particle. Metal on metal core@shell structures provide a means for generating metal nanocrystals with varied optical properties. Morriss and Collins [99] prepared Au@Ag nanocrystals by reducing Au with P by the Faraday's method and Ag with hydroxylamine hydrochloride. They observed a progressive blue shift of the Au plasmon band with incorporation of Ag, accompanied by a slight broadening. Nanoparticle of the core can be used as seeds for growth of shell particles on it. Often core@shell growth is achieved by injecting the precursors forming the shell materials into a dispersion containing the core nanocrystals. The injection is carried out at a slightly lower temperature and in a slow and controlled manner to force shell growth, avoiding independent nucleation. Thus, a mixture of diethylzinc and bis(trimethylsilyl)sulphide is injected into a hot solution containing the core CdSe nanocrystals to encase them with a ZnS layer [100]. Shell of oxide and Au has been coated on metallic oxides like ReO_3 [101].

II. Nanorods and nanotubes:

Nanorods have been prepared using vapour phase methods such as vapour-liquid-solid (VLS) growth (Fig. 1.4), vapour-solid (VS) growth, oxide-assisted growth and the use carbothermal reactions. A variety of solution methods such as seed-assisted growth, polyol method, template based growth and oriented attachment have also been developed for the synthesis of one-dimensional (1D) nanostructures. A popular method for the synthesis of metal nanowires is the use of the polyol process [102], wherein the metal salt is reduced in the presence of PVP to yield nanowires of the desired metal. CoNi nanowires are obtained by heterogeneous nucleation in liquid polyol [103]. Metal oxide nanowires and rods can also be prepared using similar synthetic stratigies [104]. Thermal

evaporation has been used for preparing 1-D metal chalcogenides like CdS, CdSe, ZnS, ZnSe [105]. An organometallic preparation of CdTe nanowires with high aspect ratios in the wurtzite structure has been described [106]. CVD, microwave assisted methods and single precursor source have also yielded high quality crystalline nanorods of various chalcogenides and oxides. Single crystalline AlN, GaN and InN nanowires can be deposited on Si substrates covered with Au islands by using urea complexes formed with the trichlorides of Al, Ga and In as the precursors [97].

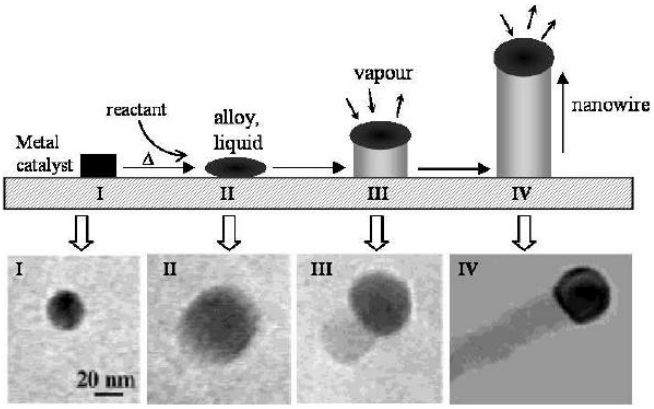

Figure 1.4. Schematic illustration of vapour-liquid-solid nanowire growth mechanismSchematic illustration of vapour-liquid-solid nanowire growth mechanism including three stages: alloying (II), nucleation (III) and axial growth (IV). In situ TEM images recorded during the process of Ge nanowire growth using Au as catalyst (From [12])

However all materials do not form nanotubes readily. Layered inorganic compounds such as metal dichalcogenides (sulfides, selenides and tellurides), halides (chlorides, bromides and iodides), oxides and boron nitride, which possess structures comparable to the structure of graphite are the most suitable candidates for synthesis of nanotubes. Tenne and co-workers [107] first recognized that nanosheets of Mo and W dichalcogenides are unstable against folding and closure and that they can form fullerene-like nanoparticles and nanotubes. Chemical routes for the synthesis of fullerenes and nanotubes of metal chalcogenides are more versatile and popular. Nanotubes of MoS_2, $MoSe_2$, WS_2 and WSe_2 can be obtained by heating MoO_3/WO_3 in a reducing atmosphere and then reacting with H_2S and HSe_2 [107]. Diselenide and disulfide nanotubes have been obtained by the decomposition of metal triselenides and trisulfides [108].

III. Organic – aqueous interface to synthesize ultra-thin flims of nanoparticles:

Interface of organic and aqueous layers have been used for the synthesis of variety of nanocrystalline flims. The method involves dissolving an organic precursor of the relevant metal in the organic layer and the appropriate reagent in the aqueous layer. The product formed by the reaction at the interface contains ultrathin nanocrystalline films of the relevant material formed by closely packed nanocrystals. This simple technique has been shown to yield nanocrystals of metals such as Au, Ag, Pd and Cu, chalcogenides such as CdS, CdSe, ZnS, CoS, NiS, CuS and PbS and oxides such as CuO [109]. The film is fairly continuous and extends over a wide area. The single crystalline and essentially defect-free nature of the film can be inferred from the HREM and the SAED pattern analysis. The authors have estimated the thickness of the film to be ~50 nm from AFM and ellipsometric studies. Thicker films were formed using higher concentration of reactants. The films prepared at higher temperatures were, however, less continuous and form flakes and rods. Using surfactants and capping agents fractals and other structures can be grown.

1.3 Properties of nanomaterials:

The interest in nanoscale materials stems from the fact that new properties are acquired at this length scale and, that these properties change with their size or shape. The changes in the properties at this length scale are not a result of scaling factors, but originate from different causes in different materials.

1.3.1 Electronic Structure:

Optical and electronic properties of nanomaterials are determined by their electronic energy levels and density of states. Metals when in bulk possess a partially filled electronic band and their ability to conduct electrons is due to the availability of a continuum of energy levels above the Fermi energy, E_F. However, at nanoscale continuum of electronic states breaks down making the material insulating

(Fig. 1.5). In the case of semiconductors in bulk state, the E_F is in between the filled and the unfilled levels (Fig. 1.5). Thus, excitation induces the formation of an electron and a hole, which are delocalized over a number of atoms or ions constituting the material. Since the material has high dielectric constant these delocalized pairs have relatively small binding energy. Such separated electron and hole bound by weak Coulombic attraction is also called a Wannier exciton. The distance between the hole and the electron is known as the Bohr radius and is on the nanometer length scale. The minimum amount

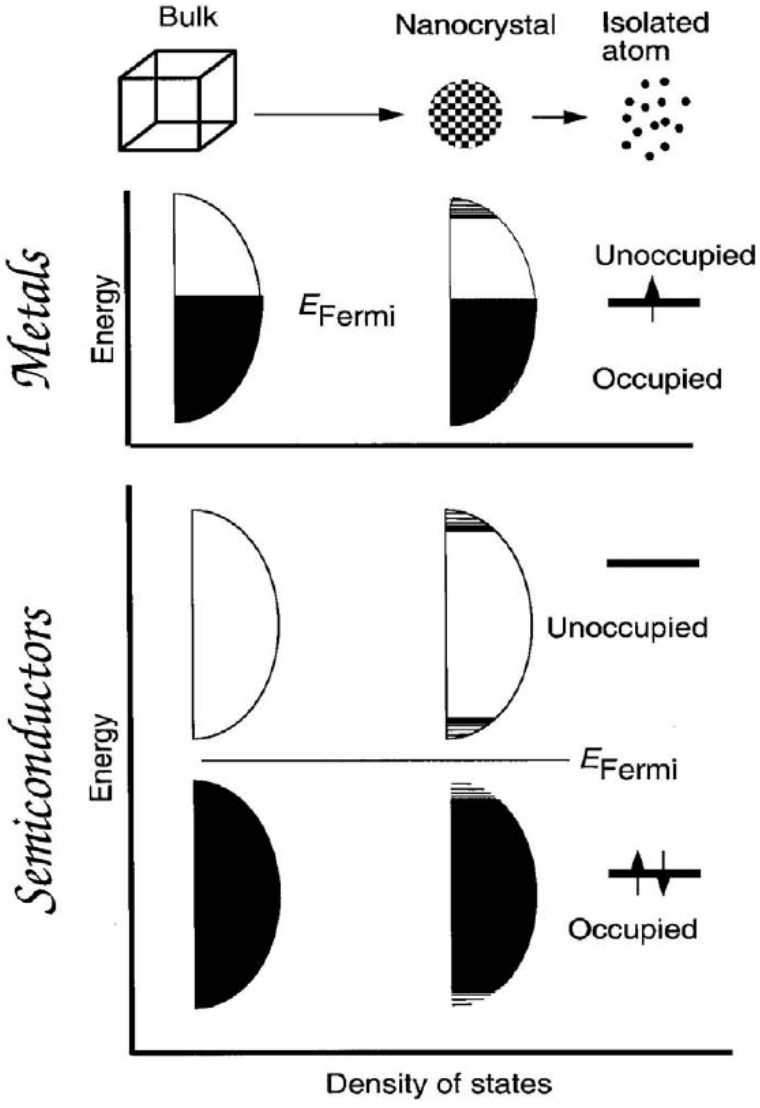

Figure 1.5. Schematic illustration of density of states of metal and semiconductors (From [1])

of energy required for the formation of these charge carriers is the band gap energy of the semiconductor. It is the energy difference between the top of the valence band and the bottom of the conduction band. When the size of the semiconductor material becomes smaller than the Bohr radius, it would decrease the space in which the charge carriers move and thus confine their motion. The situation is equivalent to the motion of an electron in a box. The solution to the Schrodinger equation of an electron in a box of length L gives the Eigen functions:

$$\varphi_n(x) = \sqrt{\frac{1}{L}}\,\sin(k_n\,x)\;; \qquad k_n = \frac{n\pi}{L} \tag{6}$$

whose corresponding energy eigenvalues are given by,

$$E_n = \frac{h^2 n^2}{8mL^2} \tag{7}$$

where m is the effective mass. As the size of the box is reduced, the energy level spacing increases since it is inversely proportional to L^2. Thus, the kinetic energy, E_n, and the excitation energy i.e. separation between two energy levels ($E_{n1} - E_{n2}$), of this particle increases upon confinement. Nanocrystals exhibiting quantum confinement are called quantum dots (QDs).

The density of states (DOS), *ρ(E)*, of inorganic crystals simultaneously evolve from continuous levels into discrete states as the dimensionality is decreased from 3D to 0D as described by the relationship:

$$\rho\,(E) \approx E^{D/2-1} \tag{8}$$

(where, *D* = dimensionality; see in Fig 1.5) [12]. In 3D crystals as in the case of bulk materials ρ*(E)* is a smooth square-root function of energy. The 2D crystals confined along a specific direction (e.g. z axis) and 1D crystals confined along two directions (e.g. x,y direction) show staircase and saw-tooth like DOS, respectively, while 0D crystals show a δ-function like DOS. (Fig. 1.6) This sudden variation of density of states with change of dimensionality imparts nanomaterials with interesting electrical and optical properties.

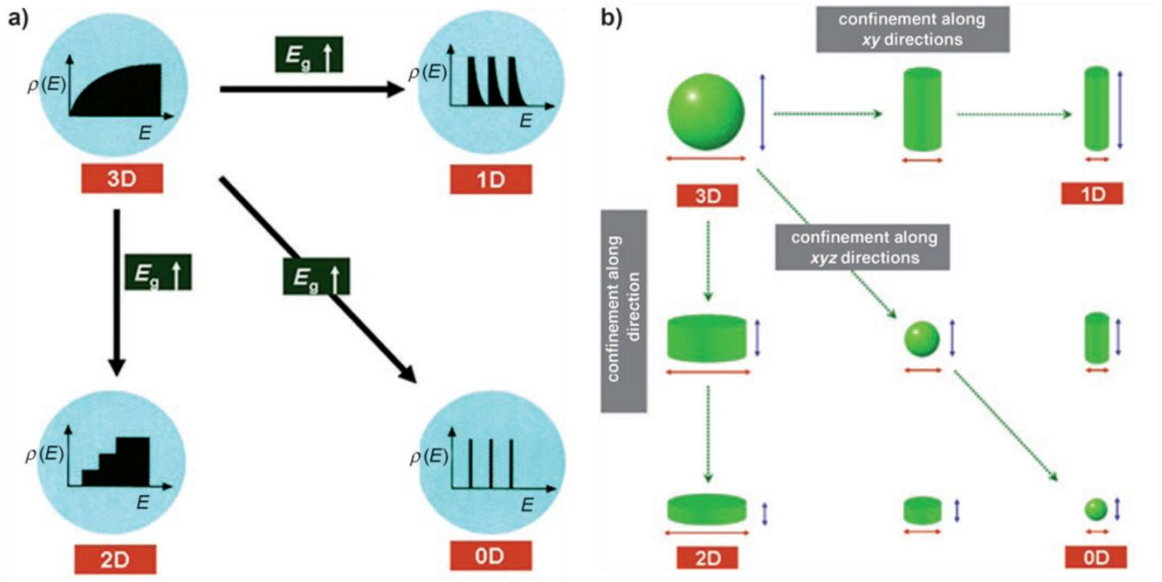

Figure 1.6 Shape evolution of crystals and their shape-dependent properties. Shape evolution of crystals and their shape-dependent properties. a) The plot of density of state (DOS) versus energy is a continuous curve for 3D crystals and changes to a discrete line for 0D crystals. The band-gap energy of semiconductors and metal oxides gradually increases as dimensionality and size reduces. b) Confinement of 3D crystals along one- (z), two- (xy), three (xyz) directions. (From [12])

1.3.2 Optical Properties:

The origin of unique optical properties of nanomaterials is different based on type of the material. Metal nanoparticles, are well known for their strong interactions with visible light through the resonant excitations of the collective oscillations of the conduction electrons within the particles. As a result, local electromagnetic fields near the particle can be many orders of magnitude higher than the incident fields and the incident light around the resonant-peak wavelength is scattered very strongly. This coherent oscillation of the metal electrons in resonance with light of a certain frequency constitutes what is known as localized surface plasmon resonance (LSPR).The surface plasmon resonance was theoretically explained by Mie in 1908. [4] The frequency and width of the surface plasmon absorption depends on the size and shape of the metal nanoparticles as well as on the dielectric constant of the metal itself and the surrounding medium [13-15]. Noble metals such as copper, silver and gold have a strong

visible light plasmon resonance, whereas most other transition metals show only a broad and poorly resolved absorption band in the ultraviolet region [15].

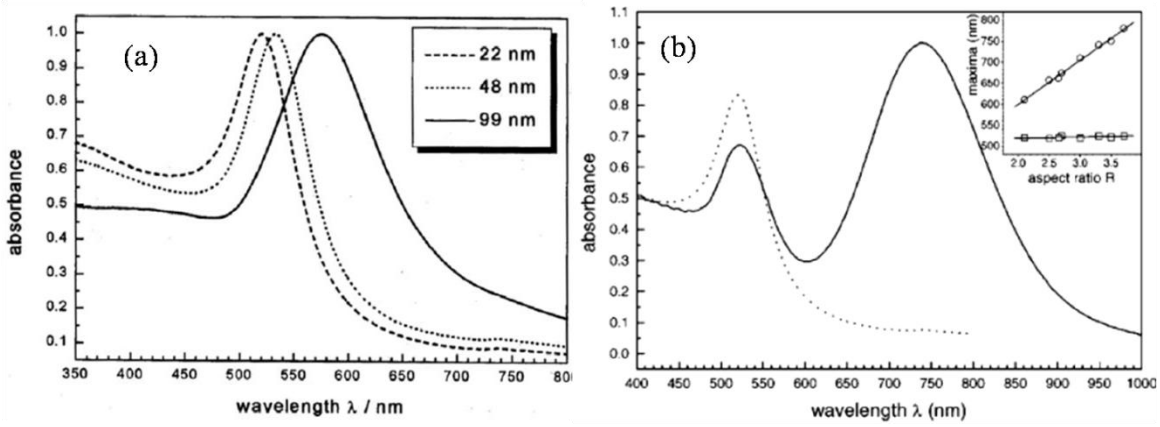

Figure 1.7 Optical absorption spectra of (a) Au nanoparticles of different sizes (From [13]) (b) Au nanorods having an aspect ratio 3.3 compared to 22 nm nanodots. (From [14]), inset shows how the maxima of the transverse (squares) and longitudinal (spheres) surface plasmon modes vary with aspect ratio.

Fig. 1.7(a) shows the absorption spectra of Au spherical nanocrystals with different sizes. Not only size but shape too plays a role in determining optical property. The plasmon resonance for nanorods splits into two bands. As the aspect ratio increases, the energy separation between the resonance frequencies of the two plasmon bands also increases [15]. The high energy band corresponds to the oscillation of the electrons perpendicular to the major axis of the rods and is referred to as the transverse plasmon absorption. The other absorption band, which is red-shifted to lower energies, is caused by the oscillation of the electrons along the minor axis of the nanorods and is known as the longitudinal surface plasmon absorption. Fig. 1.7(b) shows the experimentally observed absorption spectrum of a nanorod sample having an aspect ratio of 3.3 compared to the 22 nm nanodots [14]. The inset shows that transverse plasmon absorption band is relatively insensitive to the nanorod aspect ratio and coincides spectrally with the surface plasmon oscillation of the nanodots whereas longitudinal transverse plasmon mode varies linearly with aspect ratio.

In case of semiconductor nanocrystals discrete optical transitions along with band gap opening with size variation are observed in the absorption spectra [16, 17]. Fig. 1.8 shows the absorption spectra for a series of CdSe nanoparticles of different sizes.

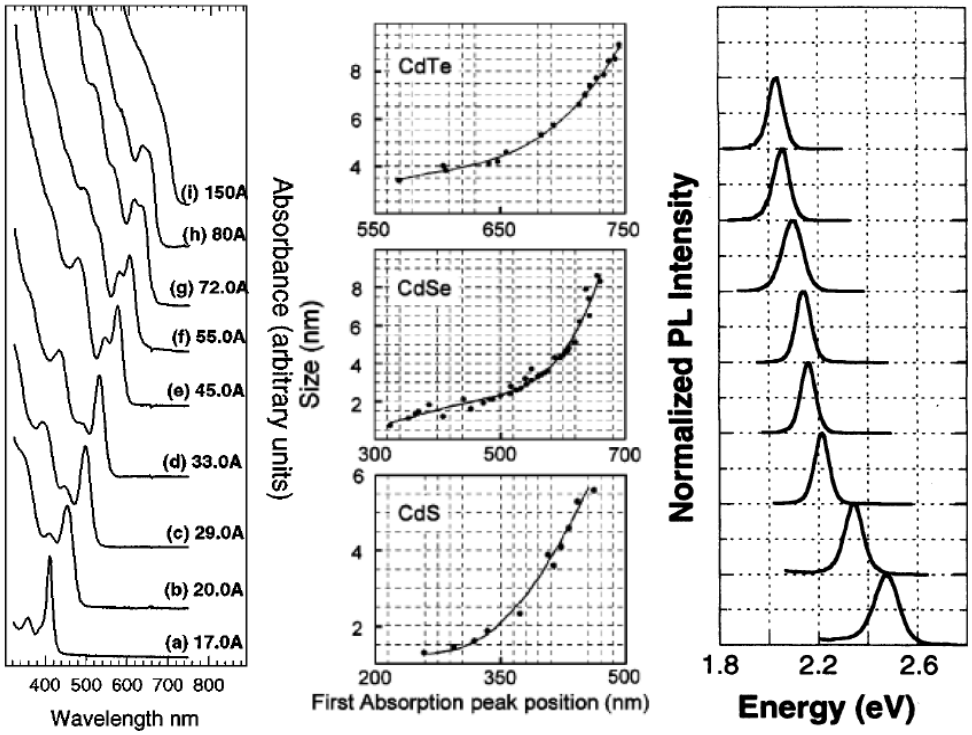

Figure 1.8 (Left) Optical absorption spectra for a series of sizes of monodisperse CdSe nanocrystals. Optical absorption spectra for a series of sizes of monodisperse CdSe nanocrystals. (From [17]). (Middle) First absorption peak change vs. the size of nanocrystals of CdSe, CdTe and CdS. (From [16]). (Right) PL spectra of different size of CdSe nanocrystals

In addition, it shows how the first absorption peak changes as the nanoparticle size changes for CdSe, CdS and CdTe QDs. The absorption spectra show a consistent red shift as the size of the particle increases and up to 10 discrete optical transitions can be resolved, which corresponds to the transitions between the discrete energy levels of the QDs. Thus, the excitonic nature of the absorption band permits direct correlation of the band gap of the semiconductor nanocrystal with the absorption edge. High-quality absorption spectrum for monodisperse QDs can be used to calculate and calibrate the size and size distribution of the synthesized nanoparticles directly (eg. of CdSe, CdTe and CdS in Fig. 1.8) [16].

1.3.3 Magnetic Properties:

Size effects were perhaps first noticed in magnetic measurements carried out on the so called "fine particles" - particles with diameters in the 10-100 nm range [113]. Magnetism of nanoparticles attracts attention due to their single domain nature, which simplifies the theoretical treatment and leads to experimental understanding. Superparamagnetism is one feature that originates because of this single domain nature. Superparamagnetic behaviour of ferromagnetic particles has set the limits on miniaturizing magnetic devices. Many metal oxides nanoparticles show evidence for the presence of ferromagnetic interactions at low temperatures. This is especially true of nanoparticles of antiferromagnetic oxides such as CoO [114]. The magnetic interaction typically causes the zerofield cooled and field-cooled magnetization curves to diverge at low temperatures. It is also possible to see ferromagnetic nature below the blocking temperature T_B For example Fig. 1.9(a) shows the temperature variation of susceptibility (χ) and the inverse susceptibility (χ^{-1}) of the 11.5 nm CoO nanoparticles.

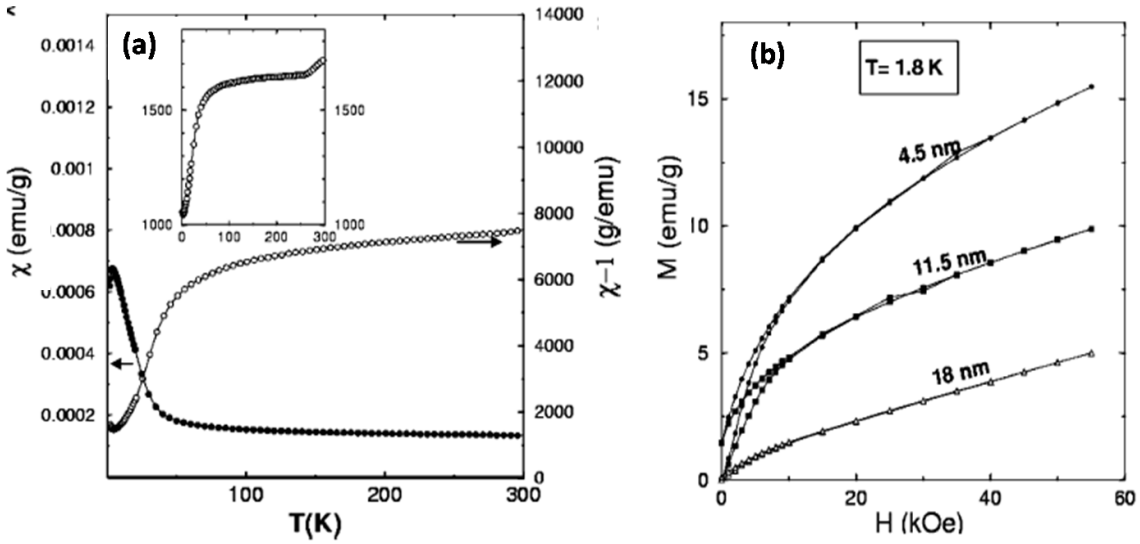

Figure 1.9 (a) The temperature dependence of dc magnetic susceptibility (χ) and inverse magnetic susceptibility (χ-1) of 11.5 nm CoO nanocrystals. The inset in (a) shows the inverse susceptibility vs. temperature curve of 16 nm CoO. (b) M vs. H at 1.8 K for 4.5, 11.5 and 18 nm CoO nanocrystals. (From [114]).

The inset in Fig. 1.9 (a) represents the inverse susceptibility (χ^{-1}) vs. temperature data of the 16 nm particles. The 16 nm as well as the 18-nm samples show the presence of an

antiferromagnetic transition as evidenced by the broad peak around 300 K in the inverse susceptibility data. The antiferromagnetic transition is wiped out as the particle size decreases, probably due to the increased ferromagnetic interaction with decrease in particle size. Accordingly, the magnitude of the Curie-Weiss temperature (Θp) obtained from the extrapolation of the high-temperature inverse susceptibility data decreases with the increase in particle size. Smaller particles tend to show low hysteresis at room temperature while larger particles do not (Fig. 1.9(b)). Recently room-temperature ferromagnetism has been observed in nanocrystals (7–30 nm diameter) of nonmagnetic oxides such as CeO_2, Al_2O_3, ZnO, In_2O_3 and SnO_2 [115,116,117]. As there were no magnetic impurities present, the origin of ferromagnetism may be the exchange interactions between localized electron spin moments resulting from anion or cation vacancies at the surfaces of nanocrystals. Thus, ferromagnetism may be a universal characteristic of nanoparticles.

1.3.4 Structure Related Properties:

Various physical properties of materials get affected drastically by reduction of size to the nanoregime. For example a decrease in melting temperature has been observed with decreasing nanocrystal size in the case of Au nanocrystals (Fig. 1.10) [118]. Such a phenomena can be explained on the basis of large number of surface atoms in the nanostructures which are coordinatively unsaturated. The surface atoms are highly energetic and hence require less thermal energy for melting. The smaller the nanocrystal, the larger the contribution from the surface to the overall energy of the system and thus, leading to further melting temperature depression. As the electron band becomes discrete energy levels, the above Ohm's law is no longer valid. Electrons

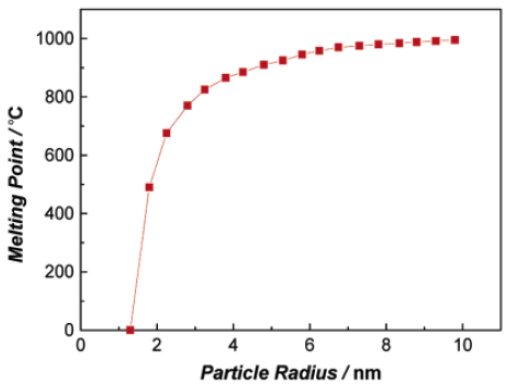

Figure 1.10. Relationship between the melting points and the sizes of gold. (From [84])

undergo what is known as Couloumb blockade. There are studies on pressure induced solid to solid phase transitions too, that demonstrate depression in the transition temperature with decreasing size of the nanocrystals.

1.4 Control over shape:

The ability to control and manipulate the physical and chemical properties of nano-materials is what we ultimately desire. This can be achieved by tuning shape and size of nanomaterials. In the last few years, researchers have been extensively studying efficient synthetic routes to well defined nanocrystals with controlled size and shape. These methods include gas-phase syntheses utilizing vapour-liquid-solid (VLS) methods, chemical vapour deposition (CVD), thermal evaporation and liquid-phase colloidal synthesis in aqueous or nonhydrolytic media [12, 15, 118-121]. Fig. 1.11 shows representative shapes of nanocrystals synthesized to date. The liquid-phase colloidal synthetic approach is an especially powerful tool for the convenient and reproducible shape controlled synthesis of nanocrystals because this method allows for the resulting nanocrystals to be precisely tuned in terms of their size and shape while maintaining them in dispersion form. Spheres are the most basic and symmetric motif among shaped nanocrystals. To grow nanocrystals with faceted faces or with shape anisotropy generally capping agents and surfactants are used. For example cube shaped $CoFe_2O_4$ is fromed under mild growth conditions from acetyl acetonate complexes of Co and Fe in

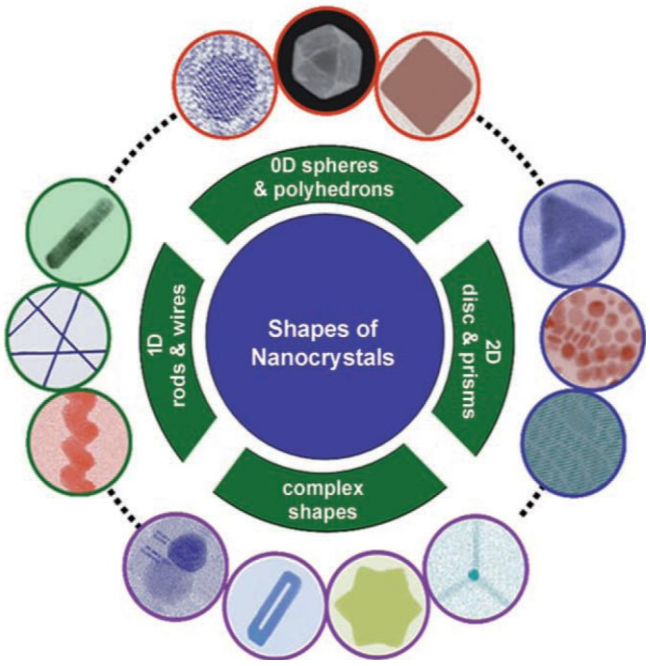

Figure 1.11 Different shapes of inorganic nanocrystals. (From [12])

presence of oleic acid and olyel amine as capping agents. Harsh growth conditions (high temperature and pressure leads to the formation of spheres (Fig. 1.12(a-c)). Similarly triangular metal oxides were produced from metal carboxylate precursors in organic solutions. Triangular, Diamond like, truncated octahedron etc. γ-Fe_2O_3 nanocrystals could be produced from $[Fe(CO)_5]$ using various concentrations of dodecyl amine as capping agent.

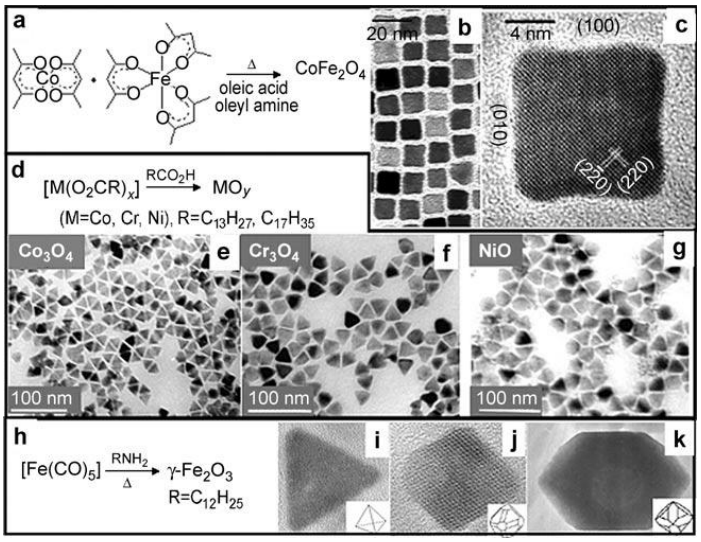

Figure 1.12 Isotropic 0D nanocrystals with distinctly faceted faces. (a–c) $CoFe_2O_4$ nanocubes obtained by thermal decomposition of [Co-(acac)$_2$]and [Fe(acac)$_3$]in a surfactant containing organic solution.b) TEM and c) HRTEM images of approximately 13-nm sized nanocubes.(d–g) Triangular shapes of metal oxides synthesized through the thermal decomposition of metal carboxylate precursors in a surfactant containing organic solution. TEM images of e) Co3O4, f) Cr2O3 and g) NiO (h–k) Various shapes of γ-Fe2O3 nanocrystals. i) TEM images of triangle, j) diamond and k) hexagon nanocrystals. These shapes are actually 2D projection of 3D shapes: tetrahedrons (i), truncated octahedrons (j) and icosahedrons, which are truncated by{111} and {110} faces (k, insets). (From [12])

Above cases are all examples of isotropic growth. It is anistropic growth that produces 1D nanocrystals. There are two representative shape-controlling mechanisms for this.

1. Shape transformation through oriented attachment.
2. Kinetically induced anisotropic growt

All of these growth mechanisms have the merit of facile separation between the nucleation and growth stages, which is a prerequisite for the shape-controlled nanocrystal fabrication.

(A)Oriented attachment

Owing to the high surface to volume ratio of nanocrystals, the surface energy significantly contributes to the total energy. Therefore, as the surface area is reduced by aggregation processes

(Fig. 1.13(a)), the total energy of the crystal will decrease. The concept of "oriented attachment" was first demonstrated by Banfield and co-workers in the hydrolytic synthesis of TiO_2 nanocrystals [122]. Truncated diamond- shaped anatase TiO_2 nanocrystals have three different faces: (001), (121) and (101). According to Donnay–Harker rules, the surface energy of the (001) is higher than those of the other surfaces [123]. Lower energy surface is thermodynamically favorable. Therefore, the fusion of diamond shaped nanocrystals along the [001] direction is facilitated by the oriented attachment process that results in a necklace-shaped nanocrystal (Fig. 1.13(b)).

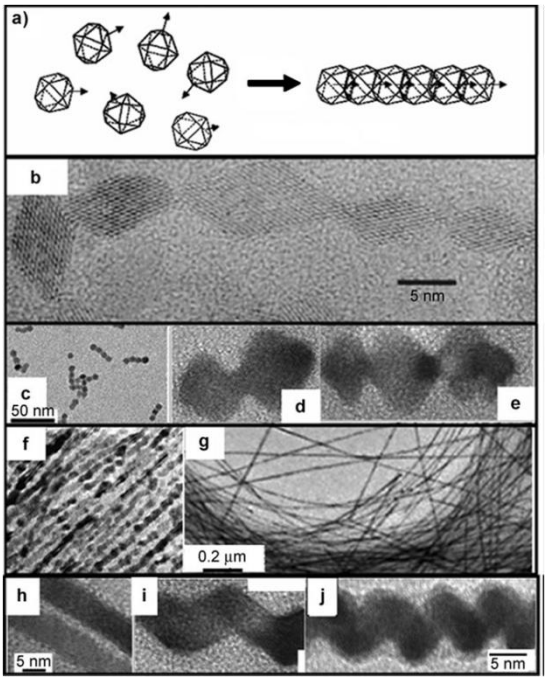

Figure 1.13 (a) Schematic representation of oriented attachment processes. The initial 0D nanocrystals align and come together along their dipole direction. After surface reconstruction to minimize the surface energy, 1D rod-based structures are obtained. (b) Aligned diamond shaped TiO_2 particles (c–e) Aggregated oligomers of PbSe nanocrystals which are intermediates during the oriented attachment processes. (f, g) Fused PbSe nanowires before (f) and after (g) surface reconstruction. By controlling the reaction parameters, various shapes of nanocrystals including straight (h) PbSe nanowires, (i) zigzag chains and (j) helices are obtained. (From [118], [119])

When there is a sufficient thermal energy in the system, the removal of high-energy there is through aging processes. PbSe nanocrystals are aligned and fused together along a specific axis (Fig. 1.13 (c–e)) and after surface reconstruction processes result in well defined nanowires (Fig. 1.13 (f, g)). Variations of either the shapes of the building blocks or the attachment directions yield a variety of nanocrystal shapes including wires, zigzags, helices, branches and rings (Fig. 1.13 (h–j)) [124].

(B) Kinetically induced anisotropic growth

The kinetically induced anisotropic growth from molecular precursors is highly effective for producing advanced shapes of nanocrystals. There are three important

key factors for determining nanocrystal shape: (1) surface energy and selective adhesion and (2) the influence of the phase of the crystalline seed. The surface energy of the crystallographic faces of a seed strongly affects the anisotropic growth patterns of nanocrystals. For example, the surface energy of the (001) face (e.g. ZnS) is larger than those of other faces [125]. Since the crystal growth rate is exponentially correlated to the surface energy, such surface-energy differences induce much faster growth along the <001> direction of ZnS than the other directions, resulting in formation of ZnS nanorods elongated along the <001> direction. The surface energy of the nanocrystals can be modulated by introducing surfactants that adsorb onto surfaces of growing crystallites. When surfactants stabilize a certain surface by "selective adhesion", the growth rate difference between different crystallographic directions can be accentuated. Selective adhesion of surfactants is critical in the synthesis of CdSe nanorods [126]. Another parameter responsible for shape control is the crystallographic phase of the nucleated seeds. When seed crystals are of the zinc blende phase, they tend to grow isotropically along the three crystallographic axes (a, b and c directions), resulting in 0D shapes, such as spheres and cubes. However, when seeds are formed in a wurtzite structure, crystals can grow anisotropically, resulting in shapes such as rods and discs. Hence, control of the key factors affecting the crystalline phases of seeds and subsequent growth is of particular interest. Crystal seeds can potentially have a variety of different crystallographic phases and the stable phase is highly dependent on the environment. For example, by adjusting the temperature during the nucleation processes, the crystalline phase may be controlled.

1.5 Concluding Remarks:

The last three decades have seen an explosion in the field of nanoscience research not only in terms of synthesis of nanomaterials but also in terms of fundamental understanding of nanomaterials. A large number of papers, reviews and books published in the last few years bear a testimony to this fact. Although the elemental composition and size control of nanostructures have been of major concern over the past decade, shape is the third major parameter in the chemistry of nanostructures. The last decade has witnessed applications of nanomaterials in catalysis, absorption, electronics

and biological tagging. However to bring nanomaterials into use in daily life, large scale synthesis and cost reduction of devices is essential. Though there has been significant effort towards end, this major progress is still awaited. It is clearly an exciting time to pursue work on synthesis properties and applications of inorganic nanomaterials.

Reference:

[1] C. N. R. Rao, A. Mueller, A.K. Cheetham, *The Chemistry of Nanomaterials*, Wiley-VCH, Weinheim **2004**, Vol. 1.

[2] M. Faraday, *Phil. Trans. R. Soc. London* **1857**,147, 145.

[3] W. Ostwald, *Die Welt Der Vernachlassigten Dimensions*, Steinkopf, Dresden, 1915.

[4] G. Mie, *Ann. Phys.* **1908**, 25, 377.

[5] R. Gans, *Ann. Phys.* **1911**, 31, 881.

[6] R. Gans, *Ann. Phys.* **1915**, 47, 270.

[7] R. Kubo, *J. Phys. Soc. Jap.* **1962**, 17, 975.

[8] A. Einstein, *Ann. Phys.* **1905**, 17, 549.

[9] R. P. Feynman, *Miniaturization*, Reinhold, New York, **1961**.

[10] C. N. R. Rao, A. K. Cheetham, *J. Mater. Chem.* **2001**, 11, 2887.

[11] G. M. Whitesides, *Nanotechnology: Art of the Possible, Technology, Review Inc.*, Cambridge, MA, Nov/Dec **1998**.

[12] Y-W. Jun, J-S. Choi, J. Cheon, *Angew. Chem. Int. Ed.* **2006**¸45, 3414.

[13] S. Link, M. A. El-Sayed, *Int. Rev. Phys. Chem.* **2000,** 19, 409.

[14] S. Link, M. A. El-Sayed, *Annu. Rev. Phys. Chem.* 54, 331 (2003).

[15] C. Burda, X. Chen, R. Narayanan, M. A. El-Sayed, *Chemical Reviews* **2005,** 105, 1025.

[16] X. Peng, J. Wickham, A. P. Alivisatos, *J. Am. Chem. Soc.* **1998**, 120, 5343.

[17] C. B. Murray, C. R. Kagan, M. G. Bawendi, *Annu. Rev. Mater. Sci.* **2000**, 30, 545.

[18] Y. Jiang, *Forced Hydrolysis and Chemical Co-Precipitation.* In *Handbook of Nanophase and Nanostructured Materials*; Z. L.Wang, Y. Liu, Z. Zhang (Eds.) , Kluwer Academic: New York, **2000,** p.59.

[19] C. B. Murray,D. J. Norris, M. G. Bawendi, *J. Am. Chem. Soc.***1993**, 115, 8706.

[20] Z. A. Peng, X. Peng, *J. Am. Chem. Soc.* **2001**, 123, 183.

[21] L. Qu, Z. A. Peng, X. Peng, *Nano Lett.* **2001**, 1, 333.

[22] J. Tanori, M. P. Pileni, *Langmuir* **1997**, 13, 639.

[23] C. Petit, T. K. Jain, F. Billoudet, M. P. Pileni, *Langmuir* **1994**, 10, 4446.

[24] I. Lisiecki, F. Billoudet, M. P. Pileni, *J. Phys. Chem.* **1996**, 100, 4160.

[25] Y. Li, T. White, S. H. Lim, *Rev. Adv. Mater. Sci.* **2003**, 5, 211.

[26] G. Coln, M.C. Hidalgo, J. A. Navo, *Catal. Today* **2002**, 76, 91.

[27] N. Uekawa, J. Kajiwara, K. Kakegawa, Y. J. Sasaki, *Colloid Interface Sci.* **2002**, 250, 285.

[28] J. Maira, K. L. Yeung, J. Soria, J. M. Coronado, C. Belver, C. Y. Lee, V. Augugliaro, *Appl. Catal. B* **2001**, 29 (4), 327.

[29] B. Li, X. Wang, M. Yan, L. Li, *Mater. Chem. Phys.* **2003**, 78,184.

[30] H. Parala, A. Devi, R. Bhakta, R. A. Fischer, *J. Mater. Chem.* **2002**, 12, 1625.

[31] W. Lackey, *J. Nucl. Technol.* **1980**, 49, 321.

[32] J. L. Woodhead, *Sci. Ceram.* **1983**, 12, 179.

[33] A. Jitianu, Y. Altindag, M. Zaharescu, M. Wark, *J. Sol-Gel Sci. Technol.* **2003**, 26, 483.

[34] D. Mondelaers, G. Vanhoyland, H. Van den Rul, J. D'Haen, M. K. Van Bael, J. Mullens, L. C. Van Poucke, *Mater. Res. Bull.* **2002**, 37, 901.

[35] Y. X. Huang, Guo, C. *J. Powder Technol.* **1992**, 72, 101.

[36] H. Yamamura, *Ceram. Int.* **1985**, 11, 72.

[37] H. S. Potdar, S. B. Deshpande, S. K. Date, *Mater. Chem. Phys.***1999**, 58, 121.

[38] S. Sheen, *Mater. Lett.* **1991**, 10, 489.

[39] J. Yang, S. Mei, J. M. F. Ferreira, *Mater. Sci. Eng. C* **2001**, 15,183.

[40] M. Yoshimura, S. Somiya, *Am. Ceram. Soc. Bull.* **1980**, 59, 246.

[41] S. Hirano, S. Somiya, *J. Am. Ceram. Soc.* **1976**, 59, 534.

[42] A. A. Burukhin, B. R. Churagulov, N. N. Oleynikov, *High Press.Res.* **2001**, 20, 255.

[43] S. W. Lu, B. I. Lee, Z. L. Wang, J. K. Guo, *J. Cryst. Growth* **2000**, 219, 269.

[44] C. C. Chen, X. Jiao, D. Chen, Y. Zhao, *Mater. Res. Bull.* **2001**, 36, 2119.

[45] I. Maclaren, P. A. Trusty, C. B. Ponton, *Acta Mater.* **1999**, 47, 779.

[46] S. H. Yu, L. Shu, Y.S.Wu, Y.T. Qian, Y. Xie, L. Yang, *Mater. Res. Bull.* **1998**, 33, 1207.

[47] X. F. Qian, X. M. Zhang, C. Wang, K. B. Tang, Y. Xie, Y. T. Qian, *Mater. Res. Bull.* **1999**, 34, 433.

[48] W. Cai, L. Zhang, *J. Phys. Condensed Matter* **1997**, 9, 7257.

[49] L. Maya, M. Paranthaman, T. Thundat, M. L. Bauer, *J. Vac. Sci. Technol. B* **1996**, 14, 15.

[50] W. Li, L. Gao, J. K. Guo, *Nanostruct. Mater.* **1998**, 10, 1043.

[51] D. Indackers, C. Janzen, B. Rellinghaus, *Nanostruct. Mater.* **1998**, 10, 247.

[52] L. E. Depero, P. Bonzi, M. Musci, C. Casale, *J. Solid State Chem.* **1994**, 111, 247.

[53] Y. Yang, V. J. Leppert, S. H. Risbud, B. Twamley, P. P. Power, H. W. H. Lee, *Appl. Phys. Lett.* **1999**, 74, 2262.

[54] K. Okuyama, I. W. Lenggoro, N. Tagami, *J. Mater. Sci.* **1997**, 32, 1229.

[55] J. R. Binder, H. Wedemeyer, *Adv. Mater.* **1997**, 9, 1049.

[56] A. Valentini, N. L. V. Carreno, L. F. D. Probst, E. R. E. Leite, Longo, *Microporous Mesoporous Mater.* **2004**, 68, 151.

[57] S. Jou, C. K. Hsu, *Mater. Science Eng. B* **2004**, 106, 275.

[58] F. Dumitrache, I. Morjan, R. Alexandrescu, R. E. Morjan, I. Voicu, I. Sandu, I. Soare, M. Ploscaru, C. Fleaca, V. Ciupina, G. Prodan, B. Rand, R. Brydson, A. Woodword, *Diamond Relat. Mater.* **2004**, 13, 362.

[59] R. Sen, A. Govindaraj, C. N. R. Rao, *Chem. Phys. Lett.* **1997**, 267, 276.

[60] R. Sen, A. Govindaraj, C. N. R. Rao, *Chem. Mater.* **1997**, 9, 2078.

[61] C. N. R. Rao, A. Govindaraj, R. Sen, B. C. Satishkumar, *Mater. Res. Innovations* **1998**, 2, 128.

[62] B. C. Satishkumar, A. Govindaraj, R. Sen, C. N. R. Rao, *Chem. Phys. Lett.* **1998**, 293, 47.

[63] B. C. Satishkumar, A. Govindaraj, C. N. R. Rao, *Chem. Phys. Lett.* **1999**, 307, 158.

[64] C. N. R. Rao, R. Sen, B. C. Satishkumar, A. Govindaraj, *Chem. Commun.* **1998**, 15, 1525.

[65] B. C. Satishkumar, P. J. Thomas, A. Govindaraj, C. N. R. Rao, *Appl. Phys. Lett.* **2000**, 77, 2530.

[66] F. L. Deepak, A. Govindaraj, C. N. R. Rao, *Chem. Phys. Lett.* **2001**, 345, 5.

[67] C. N. R. Rao, A. Govindaraj, *Acc. Chem. Res.* **2002**, 35, 998.

[68] G. Gundiah, G. V. Madhav, A. Govindaraj, C. N. R. Rao, *J. Mater. Chem.* **2002**, 12, 1606.

[69] F. L. Deepak, C. P. Vinod, K. Mukhopadhyay, A. Govindaraj, C. N. R. Rao, *Chem. Phys. Lett.* **2002**, 353, 345.

[70] T. Fukui, S. Ando, Y. Tokura, T. Toriyama, *Appl. Phys. Lett.* **1991**, 58, 2018.

[71] S. Tanaka, H. Hirayama, Y. Aoyagi, Y. Narukawa, Y. Kawakami, S. Fujita, S. Fujita, *Appl. Phys. Lett.* **1997**, 71, 1299.

[72] H. Hirayama, A. Tanaka, P. Ramvall, Y. Aoyagi, *Appl. Phys. Lett.* **1998**, 72, 1736.

[73] S. Ishida, Y. Arakawa, K. Wada, *Appl. Phys. Lett.* **1998**, 72, 800.

[74] T. Tachibana, T. Someya, Y. Arakawa, *Appl. Phys. Lett.* **1999**, 74, 383.

[75] Z. G. Bai, D. P. Yu, J. J. Wang, Y. H. Zou, W. Qian, J. S. Fu, S. Q. Feng, J. Xu, L. P. You, *Mater. Sci. Eng. B* **1999**, 72, 117.

[76] D. P. Yu, X. S. Sun, C. S. Lee, I. Bello, X. S. Sun, Y. H. Tang, G. W. Zhou, Z. G. Bai, Z. Zhang, S. Q. Feng, *Solid State Commun.* **1998**, 105, 403.

[77] Z. G. Bai, D. P. Yu, H. Z. Zhang, Y. Ding, Y. P. Wang, X. Z. Gal, Q. L. Hang, G. C. Xiong, S. Q. Feng, *Chem. Phys. Lett.* **1999**, 303, 311.

[78] P. X. Gao, Y. Ding, Z. L. Wang, *Nano Lett.* **2003**, 3, 1315.

[79] E. A. Hauser, J. E. Lynn, *Experiments in Colloid Chemistry*, McGraw- Hill, New York **1940,** p. 18

[80] (a) J. Turkevich, P. C. Stevenson, J. Hillier, *J. Discuss. Farad. Soc.* **1951,** 11, 55 ; (b) J. Turkevich, *Gold. Bull.* **1985**, 18, 86.

[81] D. G. Duff, A. Baike, P. P. Edwards, *Langmuir* **1993,** 9, 2301.

[82] N. R. Jana, X. Peng, J. Am. Chem. Soc. **2003,** 125, 14280.

[83] G. S. Fonseca, A. P. Umpierre, P. F. P. Fichtner, S. R. Teixeira, J. Dupont, *Chem. Eur. J.* **2003,** 9, 3263.

[84] M. Chen, J. Kim, J. P. Liu, H. Fan, S. Sun, *J. Am. Chem. Soc.* **2006,** 128, 7132.

[85] G. De, C. N. R. Rao, *J. Mater. Chem.* **2005,** 15, 891.

[86] J. Rockenberger, E. C. Scher, A. P.Alivisatos, *J. Am. Chem. Soc.* **1999,** 121, 11595.

[87] M. Ghosh, E. V. Sampathkumaran, C. N. R. Rao, *Chem. Mater.* **2005,** 16, 2348.

[88] M. Ghosh and C.N.R. Rao, *Chem. Phys. Lett.* **2004,** 393, 493.

[89] J. Park, K. An, Y. Hwang, J. G. Park, H. J. Noh, J. Y. Kim, J. H. Park, N. M. Hwang, T. Hyeon, Nature Mater. **2004,** 3, 891.

[90] C. B. Murray, D. J. Norris, M. G. Bawendi, *J. Am. Chem. Soc.* **1993,** 115, 8706.

[91] U. K. Gautam, R. Seshadri, C. N. R. Rao. *Chem. Phys. Lett.* **2003,** 375, 560,.

[92] U. K. Gautam, R. Seshadri. *Mater. Res. Bull.* **2004,** 39, 669.

[93] L. A. Swafford, L. A. Weigand, M. J. Bowers II, J. R. McBride, J. L. Rapaport, T. L. Watt, S. K. Dixit, L. C. Feldman, S. J. Rosenthal, *J. Am. Chem. Soc.* **2006,** 128, 12299.

[94] A. Ghezelbash, B. A. Korgel, *Langmuir* **2005,** 21, 9451.

[95] (a) U. K. Gautam, K. Sardar, F. L. Deepak , C. N. R. Rao, *Pramana* **2005,** 65, 549. (b) K. Sardar, C.N.R. Rao, *Solid State Sci.* **2005,** 7, 217. (c) K. Sardar, F. L. Deepak, A. Govindaraj, M. M. Seikh, C. N. R. Rao, *Small* **2005,** 1, 91.

[96] K. Sardar, M. Dan, B. Schwenzer, C. N. R. Rao, *J. Mater. Chem.* **2005,** 15, 2175.

[97] A. A. Guzelian, J. E. B. Katari, A. V. Kadavanich, U. Banin, K. Hamad, E. Juban, A. P. Alivisatos, R. H. Wolters, C. C. Arnold, J. R. Heath, *J. Phys. Chem.* **1996,** 100, 7212.

[98] (a) O. I. Mícíc, C. J. Curtis, K. M. Jones, J. R. Sprague, A. J. Nozik, *J. Phys. Chem.* **1994,** 98, 4966; (b) O. I. Mícíc, J. R. Sprague, C. J. Curtis, K. M. Jones, J.

L Machol, A. J. Nozik, H. Giessen, B. Fluegel, G. Mohs, N. Peyghambarian, *J. Phys. Chem.* **1995, 99**, 7754.

[99] R. H. Morriss, L. F. Collins, *J. Chem. Phys.* **1964,** 41, 3357.

[100] X. Peng, M. C. Schlamp, A. V. Kadavanich, A. P. Alivisatos, *J. Am. Chem. Soc.* **1997,** 119, 7019.

[101] S. Ghosh, K. Biswas and C. N. R. Rao, *J. Mater. Chem.* **2007,** 17, 2412.

[102] (a) Y. Sun, B. Gates, B. Mayers, Y. Xia, *Nano lett.* **2002,** 2, 165; (b) Y. Chen, B. J. Wiley, Y. Xia, *Langmuir* **2007,** 23, 4120.

[103] D. Ung, G. Viau, C. Ricolleau, F. Warmont, P. Gredin, F. Fievet, *Adv. Mater.* **2005,** 17, 338.

[104] (a) P. X. Gao, Y. Ding, W. Mai, W. L. Hughes, C. Lao, Z. L. Wang, *Science* **2005,** 309, 1700; (b) Q. Li, V. Kumar, Y. Li, H. Zhang, T. J. Marks, R. P. H. Chang, *Chem. Mater.* **2005,** 17, 1001; (c) F. L. Deepak, G. Gundiah, Md. M. Shiekh, A. Govindaraj, C. N. R. Rao, *J. Mater. Res.* **2004,** 19, 2216.

[105] (a) S. Kar, S. Chaudhuri, *J. Phys. Chem. B* **2005,** 109, 3298; (b) J. Hu, Y. Bando, D. Goldberg, *Small* **2005,** 1, 95; (c) S. Kar, S. Chaudhuri, *J. Phys. Chem. B* **2006,** 110, 4542.

[106] S. Kumar, M. Ade, T. Nann, *Chem. Eur. J.* **2005,** 11, 2220.

[107] (a) R. Tenne, L. Margulis, M. Genut, G. Hodes, *Nature* **1992,** 360, 444; (b) Y. Feldman, E. Wasserman, D. J. Srolovitch, R. Tenne, *Science*, **2000**, 267, 222; R. Tenne, *Chem. Eur. J.* **2002,** 8, 5296.

[108] (a) M. Nath, C. N. R. Rao, *J. Am. Chem. Soc.* **2001,** 123, 484 ; (b) M. Nath, C. N. R. Rao, *Chem. Commun.* **2001,** 21, 2336; (c) M. Nath, C. N. R. Rao, *Angew. Chem. Int. Ed.* **2002,** 41, 3451.

[109] (a) C. N. R. Rao, K. P. Kalyanikutty, *Acc. Chem. Res.* **2008,** 41, 489. (b) C. N. R. Rao, G. U. Kulkarni, V. V. Agrawal, U. K. Gautam, M. Ghosh, U. Tumkurkar., *J. Colloid. Interface Sci.* **2005,** 289, 305; (c) C. N. R. Rao, G. U. Kulkarni, P. J. Thomas, V. V. Agarwal, P. Saravanan. Curr. Sci. 85, 1041 (2003). (d) C. N. R. Rao, G. U. Kulkarni, P. J. Thomas, V. V. Agarwal, P. Saravanan. *J. Phys. Chem. B* **2003,** 107, 7391. (e) V. V. Agrawal, G. U. Kulkarni, C. N. R. Rao, *J. Phys. Chem. B* **2005**, 109, 7300

[110] Z. G. Bai, D. P. Yu, H. Z. Zhang, Y. Ding, Y. P. Wang, X. Z. Gal, Q. L. Hang, G. C. Xiong, S. Q. Feng, *Chem. Phys. Lett.* **1999**, 303, 311.

[111] H. Z. Zhang, D. P. Yu, Y. Ding, Z. G. Bai, H. L. Hang, S. Q. Feng, *Appl. Phys. Lett.* **1999**, 73, 3396.

[112] P. X. Gao, Y. Ding, Z. L. Wang, *Nano Lett.* **2003**, 3, 1315.

[113] J. L. Dormannn, D. Fiorani Ed. *Magnetic properties of Fine Particles*, North-Holland, Amsterdam **1992**.

[114] M. Ghosh, E. V. Sampathkumaran, C. N. R. Rao, *Chem. Mater.* **2005,** 17, 2348.

[115] A. Sundaresan, R. Bhargavi, N. Rangarajan, U. Siddesh, C. N. R. Rao, *Phys. Rev. B* **2006**, 74, 161306 (R).

[116] C. Madhu, A. Sundaresan, C. N. R. Rao, *Phys. Rev. B,* **2008, 77**, 201306.

[117] G. Schmid, *Metals. In Nanoscale Materials in Chemistry*; K. J. Klabunde Ed., Wiley-Interscience, New York, **2001**, Ch. 2, p 15.

[118] C. N. R. Rao, A. Muller, A. K. Cheetham Ed. *Nanomaterials Chemistry: Recent Developments*, Wiley-VCH Verlay, Weinheim **2007**.

[119] C. N. R. Rao, A. Govindaraj, *Nanotubes and Nanowires*, RSC series on Nanoscience, London **2005**.

[120] C. N. R. Rao, A. Govindaraj, S. R. C. Vivekchand, *Ann. Rep. Prog. Chem.*, Royal Society of Chemistry, London **2006,** 102, 20.

[121] C. N. R. Rao, P. J. Thomas, G. U. Kulkarni, *Nanocrystals: Synthesis, Properties and Applications*, Springer series on material science, **2007,** 95.

[122] R. L. Penn, J. F. Banfield, *Geochim. Cosmochim. Acta* **1999,** 63, 1549.

[123] K.S. Cho, D. V. Talapin, W. Gaschler, C. B. Murray, *J. Am. Chem. Soc.* **2005,** 127, 7140.

[124] H. Zhang, F. Huang, B. Gilbert, J. F. Banfield, *J. Phys. Chem. B* **2003,** 107, 13051.

[125] L. Manna, E. C. Scher, A. P. Alivisatos, *J. Am. Chem. Soc.* **2000,** 122, 12700.

CHAPTER 2

Solubilization of Nanodiamond by Covalent and Noncovalent Functionalization

*Summary**

Covalent solubilization of nanodiamond has been carried out by employing several methods. One of them involves reaction of acid-treated nanodiamond with thionyl chloride followed by reaction with long chain aliphatic amine to produce amide derivative. The second method involves reaction of acid-treated nanodiamond with organosilicon and organotin reagents such as hexadecyltrimethoxysilane (HDTMS), dibutyldimethoxytin (DBDMT) and perfluoro-octyltriethoxysilane (PFOTES). The products so obtained produce excellent dispersion in CCl_4 and toluene. SiO_2 and SnO_2 covered nanodiamond were obtained by heating the nanodiamond coated with organosilane and organotin reagents. The interaction of nanodiamond with various surfactants gave good dispersions of nanodiamond both in water as well as organic solvent like toluene with even low concentrations of surfactants.

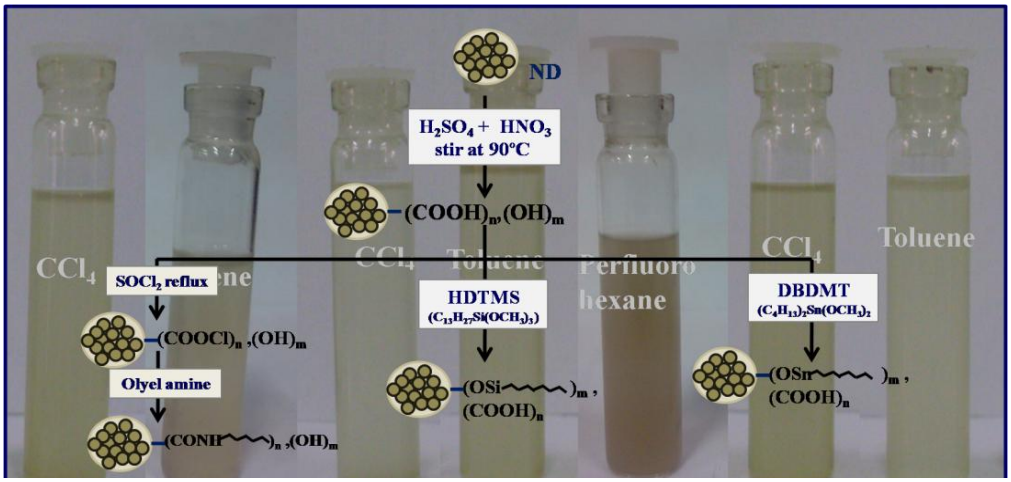

Schematics of covalent functionalization with images of solubilization in the background

***** *A paper based on this study has appeared in* ***: J. Exp. Nanosci., (2008).***

2.1 Introduction:

In recent years diamond has become a widely investigated material for its remarkable properties, for example, hardness, thermal conductivity, dopability or optical transparency over a wide spectral range, to name only a few [1]. Diamond films, in particular, have become a focus of interest. Their production by chemical vapour deposition (CVD) [2] and detonation[3] has evolved into a commercially available technique that is able to produce industrial amount of surface coatings and freestanding films for a broad range of applications, such as electronic and electrochemical devices, sensors, protective coatings and optical windows [4]. Diamond structures at the nanoscale (length ~1 to 100nm) include pure-phase diamond films, nanocrystalline diamond particles (called *'nanodiamond'* or '*ultra-nanocrystalline diamond*'), recently fabricated 1-D diamond nanorods and 2-D diamond nanoplatelets. Of all these materials nanodiamond (nanoscopic versions of sp^3 carbon) have come into focus in the last decade due to its unique properties originating from the lattice structure, large surface area and sometimes functionalised surface. This material is not only interesting for the basic understanding of the universe of carbon modifications, but it has a multitude of potential applications in the macroscopic world. While retaining the merits inherent in the diamond, nanodiamond (ND) exhibits a number of remarkable features both in their structure and in their physicochemical properties. These features give us the ground to consider ND as a specific nanocarbon material belonging to the popular family of nanocarbons which include fullerenes, nanotubes, graphene and nanoonions.

ND synthesized by detonation method consists of clusters of 3-5nm primary particles covered by graphitic shells forming micron sized aggragates. Commercially available detonation ND powder under goes several purification cycles which includes heating with oxidizing mineral acids to selectively oxidize existing graphitic material, amorphous soot and metal impurities [5]. Additionally functional groups are installed on the surface of primary particles and also on the outer side of larger agglomerates. Figure 2.1 shows a schematic view of commercial ND with several functional groups on the surface [6].

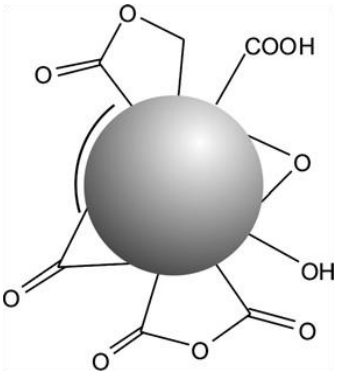

Figure 2.1 The diamond surface is covered with a variety of functional groups as determined by IR spectroscopy and TPD-MS (temperature programmed desorption-mass spectrometry).

Non-covalent or covalent modification of these surface functional groups can change the properties of these materials [7]. Several chemical approaches have been developed to modify the surfaces of the ND powder by the covalent attachment of various functional groups [8-14]. These materials can then be modified in a secondary step with more complex moieties. These compounds can be used for the covalent grafting of bioactive structures, such as peptides [15] or biotin [16]. Because of having several functional groups on the surface it has strong non-covalent interaction via hydrogen bonding or other electronic interaction. Based on this various polar biological compounds such as peptides and enzymes, for example, cytochrome c, poly-L-lysine, or apoobelin have been non-covalently linked to the surface [16]. Further functionalization, for example, free amino groups, gives the possibility to graft DNA pieces onto the coated diamond particles. It has been shown that the activity of the adsorbed biological moieties is largely conserved and that these are promising materials for sensing and separation applications [17]. Owing to its biocompatibility [18] ND is an attractive candidate for a variety of biological applications like targeted drug delivery. Lattice defects in ND like N-V centers have non-blinking, non-bleaching fluorescence in the red and infrared, which is very valuable for biolabeling purposes. Other properties like mechanical properties of polymer nanocomposites have been found to enhance significantly with diamond as nanofillers [19].

2.2 Scope of the present investigation:

Commercially available ND has a variety of functional groups on its surface (as seen in schematic Fig. 2.1). Inhomogenity of surface functional groups stands as a major obstacle in using ND for covalent grafting of molecules, noncovalent interactions or solubilisation. It is therefore necessary to achieve a homogenized surface structure by

chemical modification. Solubilisation is necessary for majority of the applications discussed above. For example, for use in biological systems stable dispersion of ND in water is necessary. Surface functionalization and dispersion is necessary for interaction of ND with polymer in case of polymer nanocomposites so as to achive superior mechanical properties.

Even though there have been many reports on reactions of ND surfaces with several chemicals or compounds, covalent functionalization of ND is not fully accomplished. Further more clear evidence for functionalization has not been provided by spectroscopic, microscopic, and other physical measurements. Solubilization in different solvents has also not been reported. In the view of the importance of functionalizing ND, with the objective of solubilizing it in polar and non-polar solvents as well as water, we wanted to carry out careful investigations making use of the literature on solubilization of inorganic nanotubes, carbon nanotubes and graphene using organosilane and organotin reagents [20-24] . These stable dispersions then can be used to prepare polymer composites.

2.3 Experimental Section :

2.3.1 Surface Homogenization of Nanodiamond:

Nanodiamond (ND) with phase purity higher than 98% and an average particle size of around 5 nm (Tokyo Diamond Tools, Tokyo, Japan) was used for the studies. The sample was first characterized to check particle size, crystallinity and surface functional groups. To get homogenous functional groups on the surface it was treated with strong oxidizing acids. For this purpose, 100 mg of the ND was refluxed with 5 ml conc. HNO_3 and 45 ml conc. H_2SO_4 for 12 h [25]. The acid-treated ND was washed with distilled water and dried under vacuum. This should generate carboxyl and hydroxyl groups homogenously on the surface of ND. Further functionalization of these acid treated species with thionyl chloride generates –COCl groups on the surface. For this the acid-treated ND was reacted with excess of thionyl chloride for 12 h in a nitrogen atmosphere. Care is to be taken to prevent exposure to moisture (exposure to moisture converts –COCl back to –

COOH).This was then reacted with an excess of oleyl amine refluxed for 12 h, washed with toluene, and dried under vacuum overnight.

2.3.2 Functionalization with organotin and organosilane reagent:

Hexadecyltrimethoxysilane (HDTMS), dibutyldimethoxytin (DBDMT) and perfluoro-octyltriethoxysilane (PFOTES) were purchased from Sigma Aldrich and used without any further purification. The solvents used were distilled and stored over sodium. All air and moisture sensitive compounds were handled under a nitrogen atmosphere. In a typical experiment to coat the ND with the organosilicon or an organotin reagent, about 30 mg of the acid treated ND were ground using an agate mortar and pestle and placed in a clean and dry round-bottomed flask. To this 20 ml of dry toluene was added and the mixture was placed in a sonic bath for 30 minutes. Organosilane or organotin reagent was then added to the nanoparticles at a 1:1 (organosilane or organotin : ND) molar ratio by micropipette in a nitrogen atmosphere. The mixture was refluxed at 373 K for 12 h after which the mixture was cooled down and the residue washed with dry hexane and then with water–acetone mixture (20% of H_2O). The functionalized ND was dried in vacuum for one day under ambient temperature. Dispersion studies were carried by sonication of the functionalized ND in an organic solvent for 5 minutes. Excess ND was removed by centrifugation and the dispersion kept undisturbed to check stability.

2.3.3 Functionalization with Surfactants:

Surfactant-induced noncovalent dispersions of ND were obtained as follows. Surfactant solutions of 20 mM strength were prepared in different solvents. A known quantity of the ND (5 mg) was dispersed in 20 ml of the solution and sonicated in a water bath for 1 h. The dispersion was allowed to stand for 24 h and then characterized. In the case of IGEPAL, 1 mM solution was prepared in water to which this 5 mg of acid-treated ND was added and sonicated for 30 min. The dispersion thus obtained was left undisturbed for 24 hours to study the stability of the dispersion.

2.3.4 Preparation of Composites:

Polymer nanocomposite with PVA and PMMA were prepared. In order to prepare PVA-ND composite, required quantity of PVA and ND were added to warm water (50 ml) and the mixture was heated at 70 °C until the polymer dissolved forming a dispersion of the ND. The dispersion was dried in Petri dishes at 50 °C over a period of 3 days [26]. PMMA-ND composites were prepared by dissolving PMMA and HDTMS-coated ND in toluene by sonication. The film was grown on water in a Petri dish maintained at 50 °C for a day.

2.3.5 Charecterization:

X-ray Diffraction: X-ray diffraction (XRD) patterns were recorded using Cu Kα radiation on a Rich-Siefert XRD-3000-TT diffractometer.

Field emission scanning electron microscopy: Field emission scanning electron microscopy (FESEM) images were obtained using a FEI NOVA NANOSEM 600. A drop of dispersions of as obtained and funtionalized ND were dried over aluminium stub for FESEM imaging. For polymer nanocomposites the flims were redissolved in respective solvent and were drop coated on the aluminum stub. Energy dispersive x-ray spectra (EDAX) were also recorded along with FESEM imaging.

Transmission electron microscopy: For transmission electron microscopy the samples were dispersed in ethanol or CCl_4 and dropped on to the holey carbon-coated copper grids. The grids were allowed to dry in the air. For polymer-ND films, the films were re-dissolved in respective solvent and a drop of this was dried over holey carbon copper grid. Transmission electron microscope (TEM) images were obtained with a JEOL JEM 3010, operating with an accelerating voltage of 300 kV.

Infrared spectroscopy: Infrared spectra were recorded using Bruker IFS 66v/S spectrometer.

Thermogravimetric analysis: Thermogravimetric analysis (TGA) was carried out on a Mettler-Toledo-TG-850 instrument

2.4 Results and Discussion:

2.4.1 Covalent Functionalization and Solubilization:

Stepwise functionalization of ND has been carried out. One important thing to remember is that ND remains as aggregates of 20-100 nm. Even when functionalization is carried out it is the aggregate as a whole that gets functionalized. Scheme 2.1 shows a schematic representation of stepwise funtionalization adopted.

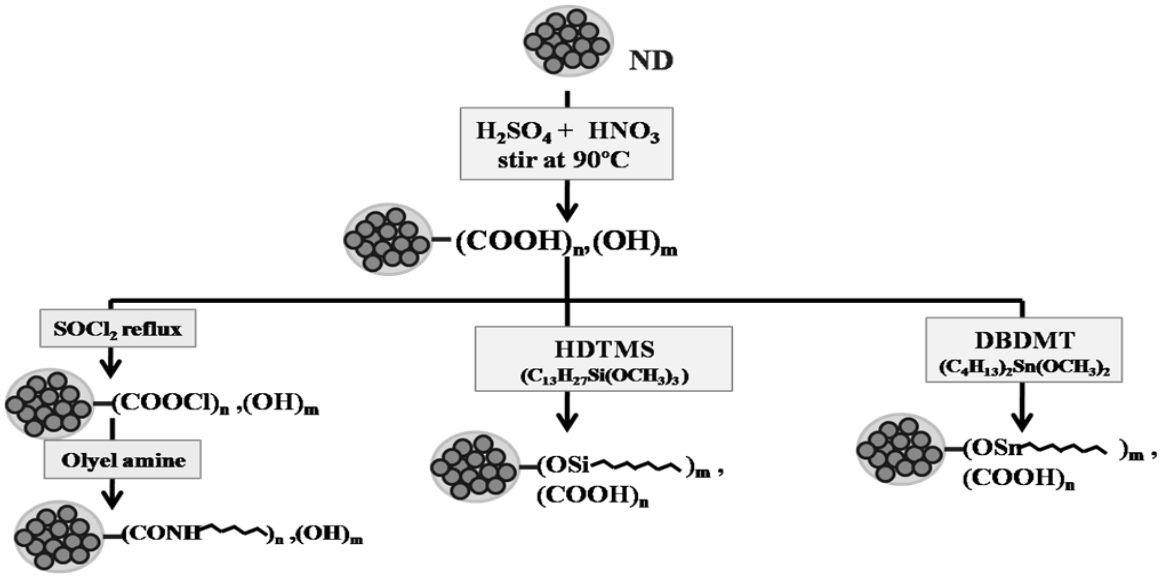

Scheme 1.1 Schematics of functionalization of ND.

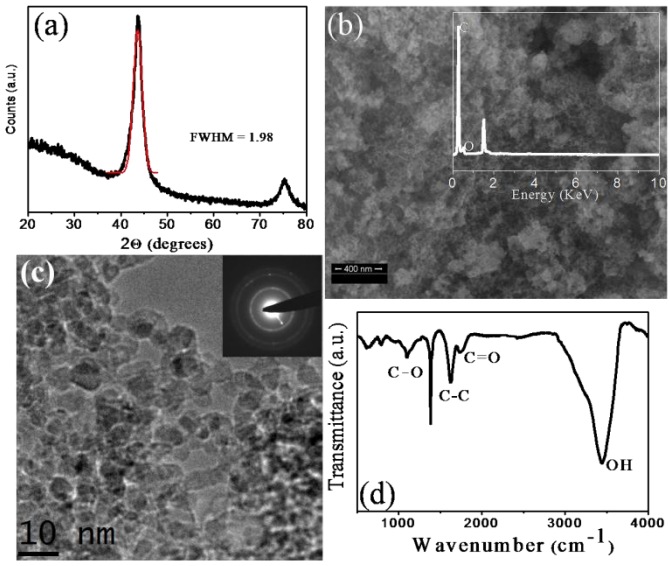

Figure 2.2. (a) XRD pattern along with Gaussian fit to determine the FWHM, (b) FESEM image with EDAX as inset, (c) TEM image with ED pattern as inset, (d) IR spectra of as obtained ND.

As obtained ND samples were first charecterized using XRD, TEM, FESEM and IR spectroscopy. XRD pattern of ND in Fig. 2.2(a) shows that as obtained ND is crystalline. Broadness of the peak is because of smaller crystallite size. FESEM image (Fig. 2.2(b)) show agglomerates of ND. EDAX spectra of ND (inset of Fig 2.2(b)) show presence of only C and O. In TEM image (Fig. 2.2(c)) it is seen that the pristine ND has an average diameter of 5 nm. Sharp lines in the electron diffraction pattern shown in the inset of Fig. 2.2(b), adds to the proof of crystallinity of ND. IR spectra in Fig 2.2 (d) shows the presence of C=O, C-O O-H and C-C stretches thus proving the presence of acid, ester, alcohol and aldihydic groups on the surface of as obtained ND.Acid-treated ND would be expected to have carboxyl and hydroxyl groups on the surface. Accordingly the IR spectrum of the ND after acid treatment, shown in Figure 2.3(b), shows carbonyl band at 1720 cm^{-1} and hydroxyl band at 3400 cm^{-1}. For comparison IR spectra of ND has been plotted in Fig 2.3(a). It is clear that on acid functinalization the Figure 2.3(c) shows the IR spectrum of amide derivative of ND which shows amide I band at 1710 cm^{-1} and amide II band at 1540 cm^{-1} and bands due to alkyl groups at 2850 and 2950 cm^{-1}.

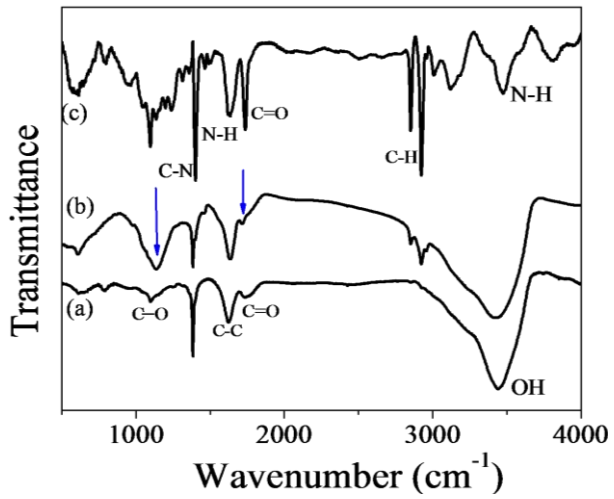

Figure 2.3 IR spectra of (a) as obtained, (b) acid treated, (c) oleyl amine treated ND. The blue arrows are used to indicate peaks with marked increase of transmittance.

In Figures 2.4 (a) and (b), we compare the TEM image of the acid functionalized ND with that of amide derivative. From the figure it is clear that diameter is not affected by amidation. The EDAX spectrum at the inset of Figure 2.4 (b) shows presence of nitrogen. The amide-derivatized NDs were soluble in non-polar solvents like toluene and CCl_4. In Fig. 2.4(c-(ii)), we show the photograph of the dispersions of amide-derivatized ND in

non-polar solvents taken after 4h. For comparison an image of as obtained ND dispersed in organic solvents is put in Fig. 2.4 (c-(i)) The XRD pattern of the amide-derivatized residue after evaporating the solvent gave characteristic (111) and (220) peaks of diamond (Fig. 2.4(d)).

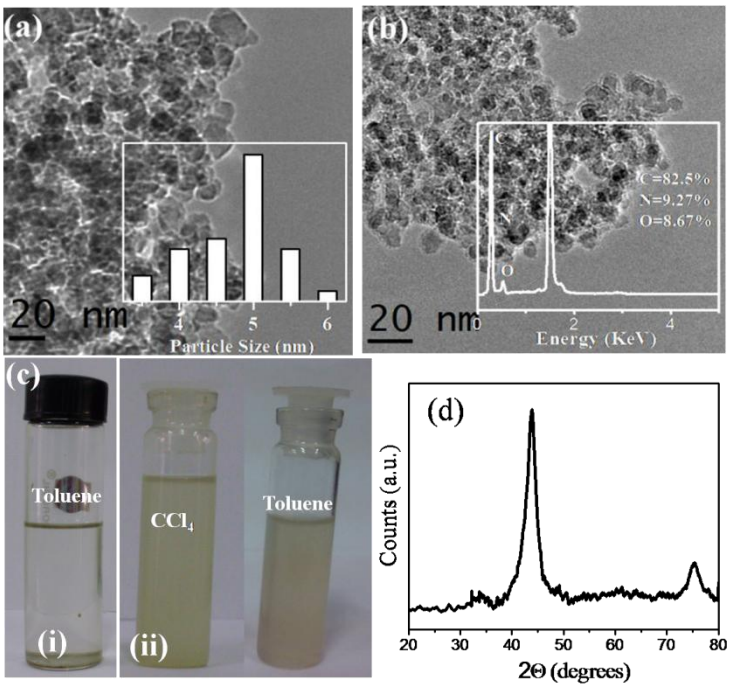

Figure 2.4 TEM image of the (a) acid functionalized ND (b) amide derivative (c) images of dispersions of (i) as obtained and (ii) amide derivetized ND in organic solvents taken after 4 hrs, (d) XRD pattern of amide derivatized ND.

Functionalization of ND with organosilane and organotin reagents was established through IR spectroscopy. In Figures 2.5(a) and (b) we show the IR spectra of organosilane and organotin coated NDs. HDTMS-coated ND show a band at 1100 cm^{-1} due to the Si-O stretching along with bands due to the alkyl groups around 2850 and 2950 cm^{-1} [27]. DBDMT-coated ND shows characteristic Sn-O stretching band at 500-600 cm^{-1} along with C-H stretching bands for the alkyl groups [28]. The product of the reaction between acid-treated ND with PFOTES shows strong C-F stretching bands in the region 1130-1230 cm^{-1} in the IR spectrum as can be seen from Figure 2.5(c). The likely reaction between acid-treated ND and organosilane and organotin reagents is as follows.

$$ND\text{-}COOH + CH_3(CH_2)_{11}CH_2Si(OCH_3)_3 \longrightarrow ND\text{-}O\text{-}Si\text{-}CH_2(CH_2)_{11}CH_3(OCH_3)_2 + CH_3OH \quad (1)$$

$$ND\text{-}COOH + (C_4H_{13})_2Sn(OCH_3)_2 \longrightarrow ND\text{-}O\text{-}Sn\text{-}(C_4H_{13})_2(OCH_3) + CH_3OH \quad (2)$$

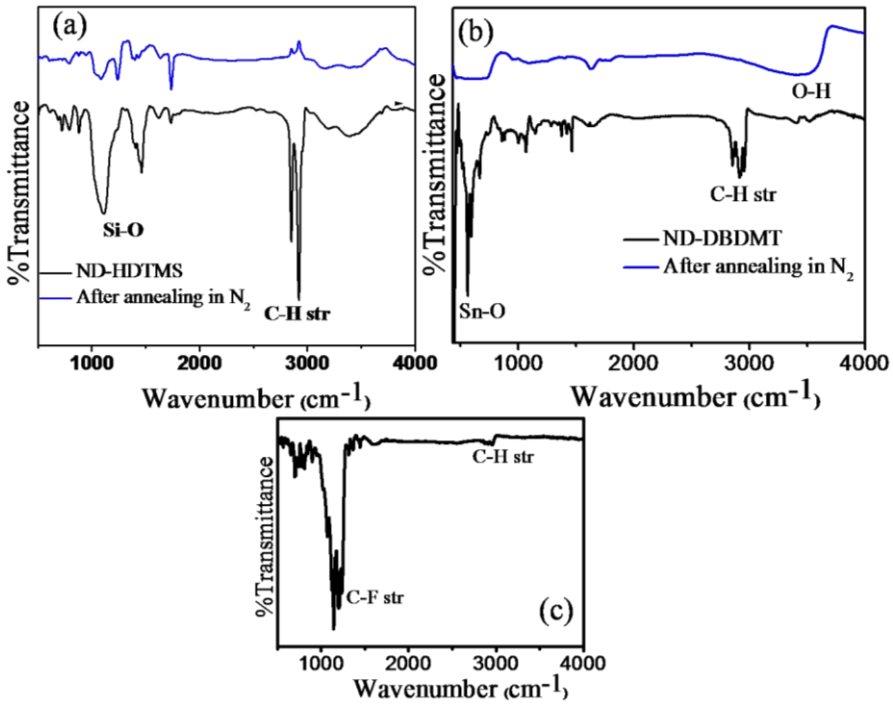

Figure 2.5 IR spectra of (a) organosilane treated ND with the sample annealed in air in blue, (b) organosilane treated ND with the sample annealed in air in blue, (c) perflurosilane (PFTEOS) treated ND.

TEM images of HDTMS-coated and DBDMT-coated ND are shown along with the EDAX spectra in Fig. 2.6 (a) and (b) respectively. From the TEM images it can be seen that the ND is coated with the organosilane or organotin reagent. The presence of the organosilane and organotin coating is confirmed by EDAX analysis. Thus the EDAX spectrum of HDTMS-coated ND (inset in Fig. 2.6(a)) shows the presence of silicon and that of the DBDMT-coated ND (inset Fig. 2.6(b)) shows the presence of tin. In Fig. 2.6(d)-(f) we show the photographs of the dispersions of the HDTMS, PFOTES and DBDMT-coated ND respectively. The photographs were taken 4h after preparation of dispersions. Interestingly, we could obtain stable dispersions of ND in the highly polar solvent perfluorohexane by using PFOTES. It appears that functionalization of ND with the long-chain oleyl amine or

treatment with HDTMS and DBDMT and PFOTES renders the surface hydrophobic which in turn induces the dispersion in non-polar solvents. The XRD patterns of HDTMS and DBDMT-coated ND (Fig 2.6.(c)) obtained after solvent evaporation were similar to that of diamond with characteristic peaks of (111) and (220) planes.

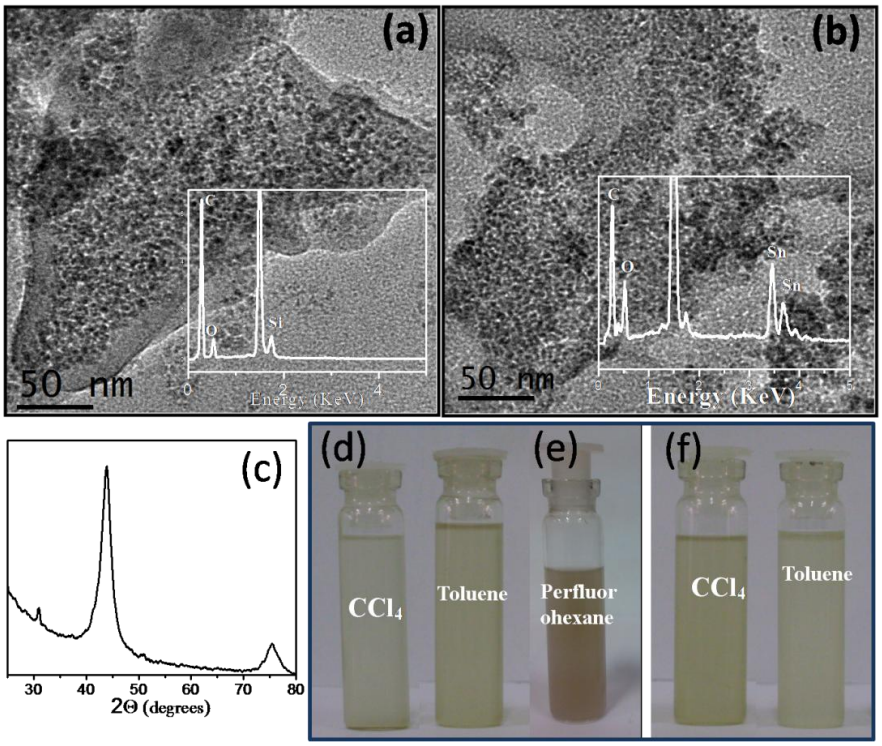

Figure 2.6 TEM image of (a) HDTMS coated and (b) DBDMT coated ND with EDAX spectra in the inset, (c) XRD spectra HDTMS coated ND obtained after solvent evaporation. Photographs of the dispersions of the (d) HDTMS, (e) PFOTES and (f) DBDMT-coated ND in different solvents (marked along with the photograph).

Funtionalized ND	Solvent	Dispersibility
ND-$CONH_2$	CCl_4	1 mg/ 6 ml
	Toluene	1mg / 8 ml
ND-HDTMS	CCl_4	1 mg / 4 ml
	Toluene	1 mg / 5 ml
ND-PFOTES	Perflurohexane	1 mg / 6 ml
ND-DBDMT	CCl_4	1 mg / 5ml
	Toluene	1mg / 6 ml

Table 2.1. Dispersibity of functionalized ND in various organic solvents.

In Table 2.1 lislisted the dispersibility (in g/ml) of ND functionalized with various reagents in toluene and CCl_4. The dispersions were checked for minimum of 6 hrs. It is clear that in general CCl_4 is a better solvent for dispersions. Dispersibility of perflurosilane treated sample in perfluro solvents is also quite good. It appears that silane treated ND with CCl_4 is the best combination.

On heating the silane-coated ND in nitrogen atmosphere at 400 °C for 1h, silica-coated ND was obtained. The presence of silica coating was confirmed by EDAX (Fig 2.7(a)) spectrum which showed the presence of silicon. The IR spectrum (Fig 2.5(a)) also shows that the Si-O stretching band at 1100 cm^{-1} is retained while the bands due to the alkyl groups have disappeared. The silica coating is, however, X-ray amorphous. Heating the organotin-coated ND produces SnO_2- coated ND. This is confirmed by the EDAX spectrum (Fig 2.7(b)) which showed the presence of tin and the IR spectrum shown in Fig. 2.5(b) which shows that the band due to Sn-O stretching around 500-600cm^{-1} is retained. The XRD pattern (Fig. 2.7 (c)) of SnO_2-coated ND showed peaks characteristic of tetragonal SnO_2 which crystallizes in the space group $P4_2/mnm$ with lattice parameters (a = 4.71 Å, c = 3.17 Å, JCPDS card no: 01-0657).

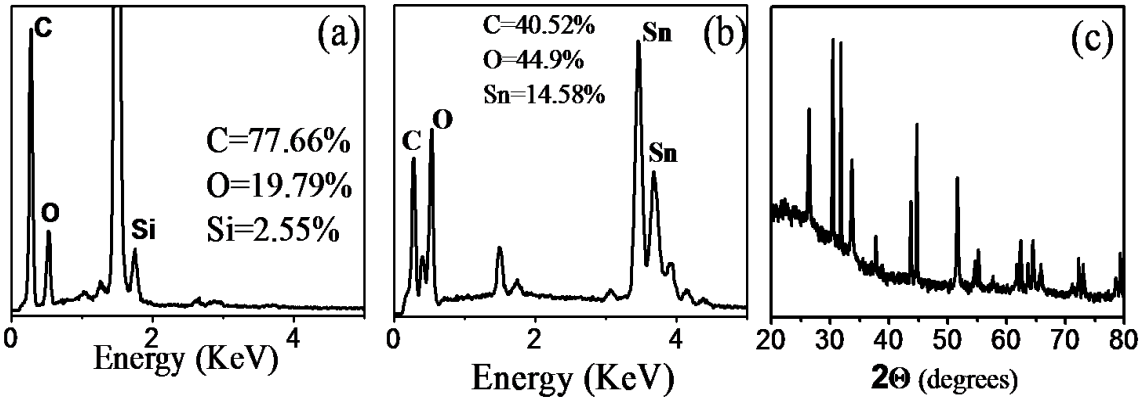

Figure 2.7 EDAX spectrum of (a) ND_HDTMS and (b) ND-DBDMT after annealing in N_2, (c) XRD pattern ND-DBDMT after annealing in N_2.

2.4.2 Noncovalent Functionalization:

ND treated with acids readily disperse in water. However the dispersions are not very stable for long periods. In order to obtain stable dispersion of ND in water, noncovalent functionalization using various surfactants have been carried out. We have used several surfactants. Fig. 2.8(a)–(e) show photographs of surfactant-induced dispersions of acid treated ND in water taken 24 h after preparation. The surfactants which hold the NDs in water for long periods are sodium bis(2-ethylhexyl) sulphosuccinate (AOT), Triton X-100 (TX-100), polyvinyl alcohol (PVA), cetyltrimethylammonium bromide (CTAB) and tert-octylphenoxy poly(oxyethylene)ethanol (IGEPAL).

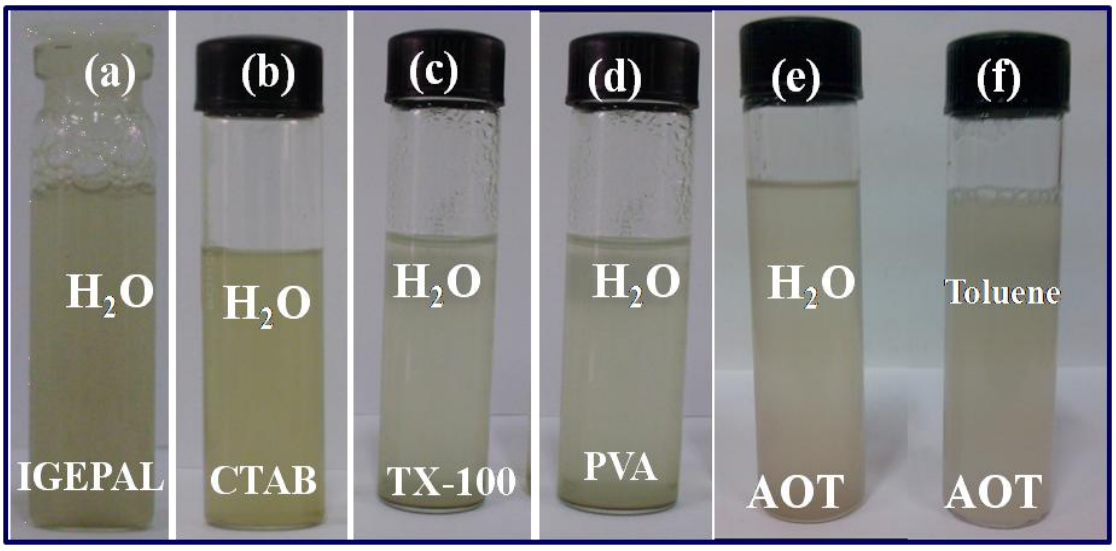

Figure 2.8 Photographs of dispersions of ND induced by (a) IGEPAL, (b) CTAB, (c) TX-100, (d) PVA and (e) AOT in water and (f) AOT in toluene.

Surfactant	Solvent	Concentration of surfactant
IGEPAL	Water	1 mM
CTAB	Water	20 mM
TX-100	Water	20 mM
PVA	Water	20 mM
AOT	Water	20 mM
	Toluene	20 mM

Table 2.2
Dispersibility of 5 mg ND non-covalently functionalized with various surfactants and polymers in water as well as toluene. Concentration of surfactant required for stable dispersion is also noted down.

Interestingly AOT can produce stable dispersions in water as well as toluene which is shown in Fig. 2.8(e) and (f). All these dispersions were stable for a week. All the surfactants invariably required a concentration of 20 mM of the surfactants to produce stable dispersion. In case of IGEPAL stable dispersions in water were obtained at a much less concentration of about 1 mM. The dispersion was stable for longer durations compared to other surfactants (Table 2.2).

We have carried out some preliminary investigations on ND-polymer composites work using ND dispersions in water and toluene. Thus it has been possible to obtain films of the ND-PVA composite by mixing aqueous solutions of PVA and acid-treated ND. Similarly the poly (methyl methacrylate) (PMMA) composite was obtained by mixing toluene solutions of PMMA and HDTMS-coated ND in toluene. In Figure 2.9, we show a TEM image of the PMMA-ND composite.

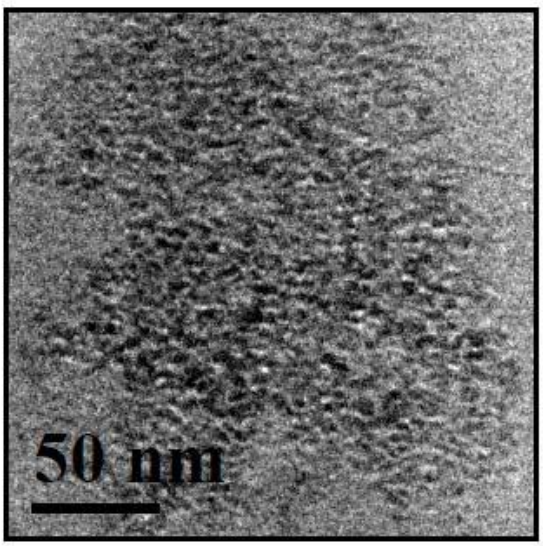

Figure 2.9 TEM image of the PMMA-ND composite.

2.5 Conclusions:

Nanodiamond can be functionalized both by covalent and noncovalent means just as in the case of single walled carbon nanotubes or grapheme. The covalently functionalized ND can easily be solubilized in nonpolar solvents like CCl_4 and toluene. Surfactant wrapped ND forms good dispersions in water. Dispersions of ND would be of

great use in the preparation of ND polymer composite films. Functionalized ND can be linked to other inorganic materials with different structures to prepare nanocomposites.

Reference:

[1] G. E. Harlow, R. M. Davies, *Elements* **2005**, 1, 67.

[2] M. Dekker, M. P. D.M. Evelyn *in Handbook of Industrial Diamonds and Diamond Films*, M. A. Prelas, G. Popovici, L. K. Bigelow, Eds. New York **1998**

[3] (a) A. I. Lymkin, E. A. Petrov, A. P. Ershov, G. V .Sakovitch, A. M. Staver, V. M. Titov , *Dokl. Akad. Nauk* **1988**, 302, 611; (b) N. R. Greiner, D. S. Philips, J. D. Johnson, F. Volk, *Nature* **1988**, 333, 440.

[4] (a) T. Soga, Y. Hayashi, T. Sharda, in A. A. Balandin, K. L. Wang, *Handbook of Semiconductor Nanostructures and Nanodevices*, American Scientific, Stevenson Ranch, USA **2006**,2, p. 149; (b) N. Ali, E. Titus, J. Gracio, W. Ahmed, E. Ahmed, *Recent Res. Dev. Mater. Sci.* **2004**, 5, 55; (c) O. A. Williams, M. Nesladek, *Phys. Status Solidi A* **2006**, 203, 3375.

[5] (a) O. A. Shenderova, V. V. Zhirnov and D. W. Brenner, *Crit. Rev. Solid State Mater. Sci.*, **2002**, 27, 227. (b) T. Daulton, D. D. Eisenhour, T. J. Bernatowicz, R. S. Lewis and P. R. Buseck, *Geochim. Cosmochim. Acta* **1996**, 60, 4853; (c) K. V. Volkov, V. V. Danilenko and V. I. Elin, *Fiz. Goreniya Vzryva* **1990**, 26, 123; (d) V. Yu. Dolmatov, *Russ. Chem. Rev.*, **2001**, 70, 607.

[6] Yang, W.; Auciello, O.; Butler, J. E.; Cai, W.; Carlisle, J. A.; Gerbi, J. E.; Gruen, D. M.; Knickerbocker, T.; Lasseter, T. L.; Russel, J. N., Jr.; Smith, L. M.; Hamers, R. J. *Nat. Mater.* **2002**, 1, 253.

[7] J. B. Miller, D. W. Brown, *Langmuir* **1996**, 12, 5809.

[8] V. S. Smentkowski, J. T. Jr. Yates, *Science* **1996**, 271, 193.

[9] C. S. Kim, R. C. Mowrey, J. E. Jr. Butler, J. N. Russell, *J. Phys. Chem. B* **1998**, 102, 9290.

[10] T. Nakamura, M. Ishihara, T. Ohana, Y. Koga, *Chem. Commun.* **2003**, 7, 900

[11] Y. Liu, Z. Gu, J. L. Margrave, V. N. Khabashesku *Chem. Mater.* **2004,** 16, 3924.

[12] A. Krueger, Y Liang, G. Jarre, J. Stegk, *J. Mater. Chem.*, **2006**, 16, 2322.

[13] B. Spitsyn, J. L. Davidson, M. N. Gradoboev, T. B. Galushko, N. V. Serebryakova, T. A. Karpukhina, I. I. Kulakova, N. N. Melnik, *Diamond Relat. Mater.*, **2006**, 15, 296.

[14] G. V. Lisichkin, V. V. Korol'kov, B. N. Tarasevich, I. I. Kulakova, A. V. Karpukhin, *Russ. Chem. Bull.*, **2006**, 55, 2212.

[15] A. Krueger, J. Stegk, Y. Liang, L. Lu and G. Jarre, *Langmuir* **2008**, 24 , 4200.

[16] (a) V. S. Bondar', I. O. Pozdnyakova, A. P. Puzyr', *Phys. Solid State* **2004**, 46, 758. (b) L. C. L. Huang, H. C. Chang, *Langmuir* **2004**, 20, 5879; (c) P. H. Chung, E. Perevedentseva, J. S. Tu, C. C. Chang, C. L. Cheng, *Diamond Relat. Mater.* **2006**, 15, 622; (d) T. T. B.Nguyen, H. C. Chang, V. W. K. Wu, *Diamond Relat. Mater.* 2007, 16, 872.

[17] A. P. Puzyr', I. O. Pozdnyakova, V. S. Bondar', *Phys. Solid State* **2004**, 46, 761.

[18] (a) K. Bakowicz, S. Mitura, *J. Wide Bandgap Mater.* **2002**, 9, 261; (b) A. M. Schrand, H. Huang, C. Carlson, J. J. Schlager, E. Osawa, S. M. Hussain, L. Dai, *J. Phys. Chem. B* **2007**, 111, 2.

[19] L. Li, J. L. Davidson, C. M. Lukehart, **Carbon**, 2006, 44, 2308.

[20] C. N. R. Rao, A. Govindaraj, *Nanotubes and Nanowires*, RSC Series on Nanoscience, Royal Society of Chemistry, London, 2006.

[21] K. S. Subhramanium, S. R. C. Vivekchand, A. Govindaraj , C. N. R. Rao, *J. Mater. Chem.*, 2008, 18, 1517.

[22] A. Gomathi, S. J. Hoseini and C. N. R. Rao, *J. Mater. Chem.* **2009,** 19, 988.

[23] S. Ghosh, A. Gomathi and C. N.R. Rao, *J. Nanosci. Nanotech.* **2009**, 9, 5214.

[24] K.S. Subrahmanyam, A. Ghosh, A. Gomati, A. Govindaraj, C.N.R. Rao, *Nanosci. Nanotech. Letts* **2009,** 1, 28.

[25] (a) A. Krueger, J. Stegk, L. Lu, Y. Liang, G. Jarre, *Langmuir* **2008**, 24, 4200; (b) F. Neugart, A. Zappe, F. Jelezko, C. Tietz, J. P. Boudou, A. Krueger, J. Wrachtrup, *Nano Lett.* **2007**, 7, 3588.

[26] S. R. C. Vivekchand, U. Ramamurty, C. N. R. Rao, *Nanotechnology*, **2006**, 17, S344.

[27] T. H. Benny, S. S. Wong, *Chem. Mater.* **2006**, 18, 4827.

[28] P. Siciliano, *Sensors and Actuators B* **2000**, 70, 153.

CHAPTER 3

Mechanical Properties of Polymer Nanocomposites of Nanodiamond and other Nanocarbons

*Summary**

Poly(vinyl alcohol)-matrix reinforced with nanodiamond (ND) particles, with ND content up to 0.6 wt%, were synthesized. Nano-indentation technique employed to assess the mechanical properties of composites show that even small additions of ND lead to significant enhancement in the hardness and elastic modulus of PVA. Interaction of ND with PVA matrix is supposed to be the cause of such enhancements.

Binary combinations of nanodiamond, few layer graphene, and single-walled nanotubes have been used to reinforce polyvinyl alcohol. The mechanical properties of the resulting composites show extraordinary synergy, improving the stiffness and hardness properties by as much as 400% compared to those obtained with single nanocarbon reinforcements.These results suggest a way of designing advanced materials with extraordinary mechanical properties by incorporating small amounts of two nanomaterials.

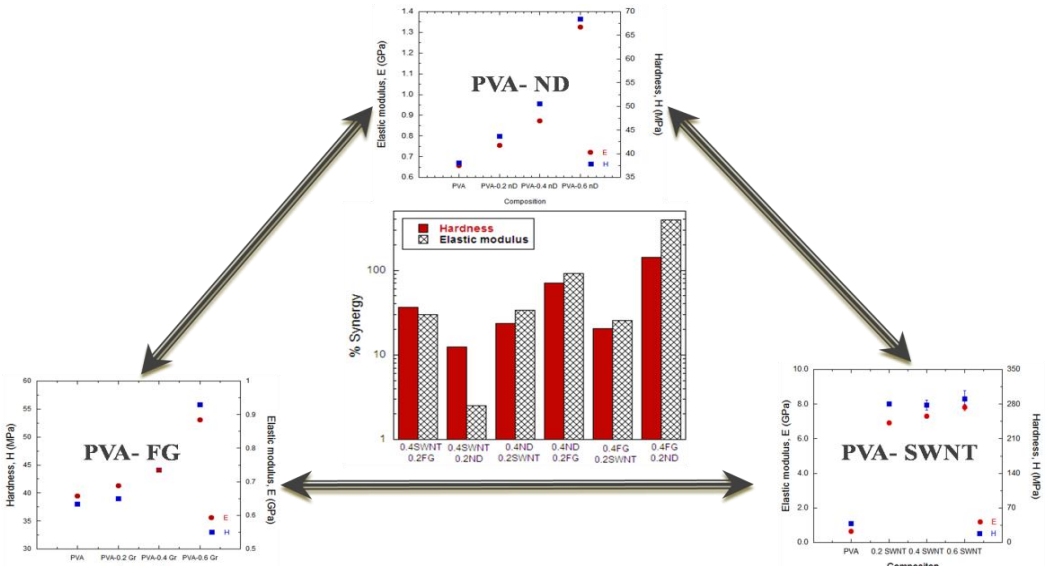

Schematic representation of obtaining synergistic effects with adding two nanocarbon fillers into polymer matrix composites

---

Papers based on this study have appeared in:* ***Solid State Commun., (2009); Proc. Natl. Acad. Sci., (USA), (2009).*

3.1 Introduction:

On December 15, 2009 world's most fuel efficient aircraft, 'Boeing 787 Dreamliner', went for its first flight. Most of its parts were made up of carbon fibre reinforced polymer matrix composites. Slowly all traditional materials specially metals are giving way to polymer matrix composites as engineer materials. This is because of its high strength to weight ratio and ease of processibility. Use of nanoscale fillers push this strategy to the next level by exploiting the advantages that nanometre-size particulates offer as compared to macro- or microscopic fillers, such as huge surface area per unit mass, ultra-low filler levels required for connectivity through the sample (low percolation threshold), extremely small interparticle separations in a polymer matrix, and often very high length-to-width, or aspect, ratios. Polymer nanocomposites have been known since decades. For example, the clay reinforced resin known as Bakelite was introduced in the early 1900's as one of the first mass-produced polymer-nanoparticle composites [1]. Even before Bakelite, nanocomposites were finding applications in the form of nanoparticle-toughened automobile tires prepared by blending carbon black, zinc oxide, and/or magnesium sulfate particles with vulcanized rubber [2]. However this field remained largely ignored until Toytota researchers revealed that adding mica to nylon produced a five-fold increase in the yield and tensile strength of the material [3, 4]. Last decade has seen an upsurge in this field. In particular, the growing availability of nanoparticles of precise size, varieties of dimensionalities and the development of instrumentation to probe small length scales, such as scanning force, laser scanning fluorescence, and electron microscopes, have spurred research aimed at probing the influence of particle size and shape on the properties of nanoparticle-polymer composites. Research has focused around designing composites that combine the desirable properties of nanoparticles and polymers. The ensuing research revealed a number of key challenges in producing nanocomposites that exhibit a desired behavior. The greatest stumbling block to the large-scale production and commercialization of nanocomposites is the dearth of cost effective methods for controlling the dispersion of the nanoparticles in polymeric hosts. It is a general tendency of nanoparticles to form aggregates thus negating any benefits associated with the nanoscopic dimension. There is a critical need for establishing processing techniques that are effective on the nanoscale yet are applicable to macroscopic processing.

3.2 Scope of the present investigation:

One way of classifying nano-filler materials is on the basis of their dimensionality (zero, one or two). Some examples are nanoclay or nanodiamond (zero-dimensional), single- or multi-walled carbon nanotubes and inorganic nanowires (one-dimensional) and single- or few-layer graphenes (two-dimensional). The mechanical properties of PMCs that are reinforced with one- or two dimensional nanofillers have received considerable attention recently [5-10]. There have been very few studies on zero dimensional nanofiller reinforced composites, except those of nano-clay reinforced ones [1, 11]. Keeping this in view, we have examined the effectiveness of nanodiamond (ND), in enhancing the mechanical properties of PVA. Choice of ND is based on the fact that it can be obtained in large quantities by detonation synthesis and is relatively inexpensive with broad applicability. Dolmatov [12] have studied the effect of ND (~2 wt%) addition on the mechanical properties of rubber. The particle size they used is about 44 nm. Kurin *et al.* [13] have made PVA-7wt% ND fiber coatings and observed ~200% increment in stiffness and large enhancement in breaking strength. But these composites suffer from poor ductility, which could be due to the large ND content. Behler et al. [14] have recently reported a ~400% increase of Young's modulus and a ~200% increase of hardness by dispersing ND (~20 wt%) into electro spun polyamide11 fibers. However, higher concentrations of ND lead to agglomeration of the powders. One way to avoid this problem is using lower filler additions, so that the properties of the polymers are preserved with moderate enhancement in mechanical properties. Furthermore, the rate of enhancement in the mechanical properties is highest when the nanofiller concentration is at the dilute limit. There are very few recent studies on the effectiveness of ND in enhancing the mechanical properties, when ND concentration is around 1 wt% [15, 16]. The objective was to investigate the mechanical properties of PVA-ND composites with small additions of ND (0.2, 0.4 and 0.6 wt%).

Again one of the hurdles to the broader use of nanocomposites is the absence of understanding of structure-property relationships. While there have been some studies to correlate the morphology of the nanocomposites with the macroscopic performance of the materials [5-10] none have discussed in detail variation of nature of interaction of

nanofillers based on its diamentionality. Of the variety of nanomaterials synthesized and characterized in recent years, nanocarbons of different dimentionalities are of particular interest, as exemplified by nanodiamond, nanotubes and graphene with dimensionalities of 0, 1, and 2, respectively [17-20]. We would expect the nature of interaction of the nanocarbon constituent with the matrix to vary with the dimensionality. For example, carbon nanotubes added to a polymer can interact over the length of the polymer chain whereas a nanodiamond particle can interact only at a point, possibly at the ends of a polymer chain. While each of the nanocarbons improves the mechanical properties of the polymer matrix, we felt intuitively that incorporation of 2 nanocarbons could lead to synergistic effects in the mechanical properties, as each of them interacts with the matrix differently. We have, therefore, carried out an investigation of the effect of incorporation of different binary combinations of the nanocarbons, nanodiamond (ND), single-walled nanotube (SWNT), and few-layer graphene (FG), on the mechanical properties of polymer matrix composites (PMCs) formed with polyvinyl alcohol (PVA). We have examined all of the 3 possible combinations of reinforcements, ND plus FG, FG plus SWNT, and ND plus SWNT. The results have been truly exciting and not entirely expected.

3.3 Experimental Section:

FG was prepared by the exfoliation of graphite oxide following the procedure described recently [19]. SWNTs were prepared by DC arc-discharge process. After preparation, the SWNTs were treated with HCl and heated in H_2 several times to remove the metal nanoparticles and amorphous carbon [19]. ND with phase purity higher than 98%and an average particle size of around 5 nm was purchased from Tokyo Diamond Tools.

3.3.1 Functionalization of nanofillers:

As the mechanical properties of the polymer-matrix composites depend on the efficient interaction between the polymer matrix and the filler material, the nanofillers were functionalized to create surface carboxyl and hydroxyl groups [7, 8], which interact with the PVA at molecular level. For this purpose, 100 mg of the ND was refluxed with 5 ml conc. HNO_3 and 45 ml conc. H_2SO_4 for 12 h. The acid-functionalized

ND was washed with distilled water and dried under vacuum. ND so prepared was dispersed in aqueous media. FG and SWNT were functionalized by acid treatment by the following procedure. A mixture of concentrated HNO_3, concentrated H_2SO_4, water, and corresponding nanocarbon was heated in a microwave oven for about 5–8 min under hydrothermal conditions. The mixture was heated at 100 °C for 6–8 h in an oven. The product thus obtained was washed with distilled water and filtered through a sintered glass funnel. The product so obtained was functionalized with -COOH and -OH groups **[18, 21]**.

3.3.2 Preparation of composites:

The composites of PVA with the functionalized nanocarbon were prepared in aqueous media. First we prepared composites containing only one nanofillers with 0.2, 0.4, and 0.6 wt% of each nanofillers in PVA matrix. Next step was to make all permutations of these nanofillers of wt% 0.2, 0.4 and 0.6 and add them to PVA. To prepare PVA-nanocomposites, 2 g of PVA was first dissolved in water. It was heated to 70-80 ºC for complete dissolution. Required amount of nanofiller was dispersed in distilled water by sonication for 15-20 min. It was then added to the PVA solution followed by sonication for 20-30 min. The mixture was then dried in Petri dishes at 35-40 ºC over a period of 3 days. Since the mechanical properties of the PVA are sensitive to the moisture content, the composites were desiccated over $CaCl_2$ for 7 days or more before performing nanoindentation experiments.

3.3.3 Charecterization:

Funtionalized nanofillers were charecterized by IR sprctroscopy using Bruker IFS 66v/S spectrometer. For transmission electron microscopy the samples were dispersed in ethanol and dropped on to the holey carbon-coated copper grids. The grids were allowed to dry in the air. For polymer-nanocomposite films, the films were re-dissolved in water and a drop of this was dried over holey carbon copper grid.Transmission electron microscope (TEM) images were obtained with a JEOL JEM 3010, operating with an accelerating voltage of 300 kV. X-ray diffraction (XRD) patterns were recorded using Cu Kα radiation on a Rich-Siefert XRD-3000-TT diffractometer.

Differential scanning calorimetry (DSC) was performed (8 mg) at a scan rate of 0.16 K/s from 50-250 ºC. For PVA-ND composites SAXS measurements were carried out, to see the interparticle distances in polymer films of different concentrations. For SAXS measurements Bruker-AXS NanoSTAR instrument was used. The instrument has X-ray tube (Cu Kα radiation, operated at 45 kV/35 mA), cross-coupled Göbel mirrors, threepinhole collimation, evacuated beam path, and a 2D gas-detector (HI-STAR) [22]. SAXS data were recorded in the *q* range of 0.007 to 0.21 $Å^{-1}$ (i.e, 2θ = 1-3º).

3.3.4 Mechanical properties:*

(****Nanoindentation measurements and analysis were carried out by Mr. K. Eswar Prasad and Prof. U. Ramamurty in Dept. of Materials Engineering, Indian Institute of Science)***

Mechanical properties of the PVA-nanocomposites were determined using nano-indentation technique. Thin films of 0.5 mm in thickness (10mm×10mm area) were used for indentation. These films are stuck to a steel plate with a thin layer of glue which dried thoroughly. Quasi-static nano-indentation was carried out using Hystiron Triboindener with a Berkovich tip (a three sided pyramidal diamond tip). Since the hardness, *H*, and the Young's modulus, *E*, obtained from the instrumented indentation experiments are sensitive to the area function of the indenter, it was first calibrated by employing a quartz standard sample. Since the loads that are used are small, the area function is calibrated at the low depth range. With the new area function, the *H* and *E* values measured on the standard Al and quartz samples were found to be within the 5% standard deviation given by the manufacturer, validating the calibration. The mechanical properties of polymers are sensitive to the loading rate and the pause time at the peak load. Therefore, these indentation parameters were optimized until *H* and *E*, obtained from the nano-indentation are comparable with the available literature data [23]. A peak load of 1mN was chosen, such that the substrate does not influence the measured properties. The loading and the unloading rates used were 0.1 mN/s with a hold time of 10 s at the peak load. Ten indentations are made on each sample and the average values of the *E* and *H* from these measurements are reported. In all of the cases, care was taken that the penetration depth was 1000 nm. Hardness and elastic modulus were determined by the Oliver-Pharr method [24].

3.4 Results and discussion:

Stiffness (*E*) is determined by the atomic bonding characteristics as well as the structure of the material. Polymers suffer from poor stiffness because *E* of a polymer is determined by the van der Waals bonding that exists between different polymer chains, which allows for relative sliding of the polymer chains rather easily. Functionalized nanocarbons form chemical bonds with the polymer chains, and affect the inter-chain bonding characteristics, making it difficult for the relative sliding to take place. Hardness (*H*) reflects the resistance of the composite to plastic deformation. The controlling characteristic is the efficiency with which the applied load is transferred from the softer matrix phase to the stronger reinforcement phase. Strong adhesion between nanocarbons and polymer and also their crystallinity favor effective load transfer.

3.4.1. PVA-Nanodiamond composites:

TEM images of as received (AR_ND) and after functionalization (AF-ND) and PVA-0.6 wt% ND are shown in Fig. 3.1(a), (b) and (c) respectively. Both AR-ND and AF-ND have an average diameter of 5 nm.

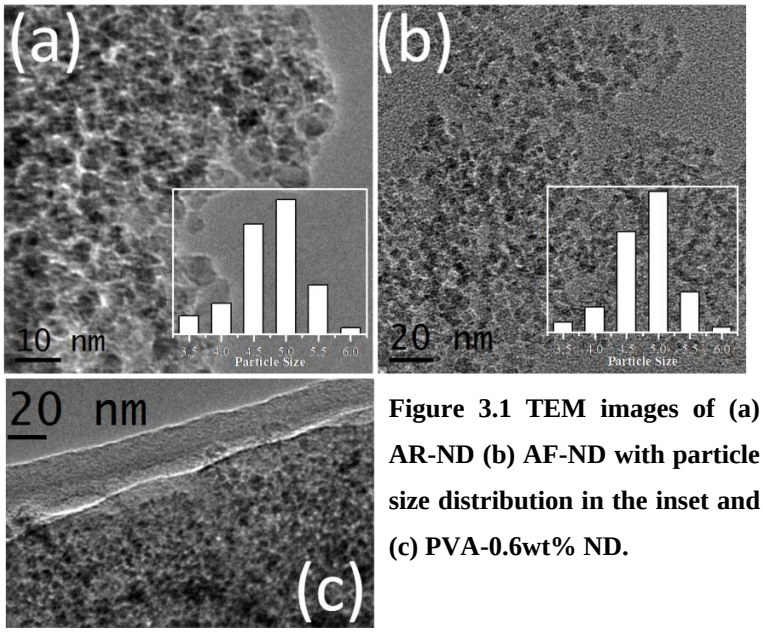

Figure 3.1 TEM images of (a) AR-ND (b) AF-ND with particle size distribution in the inset and (c) PVA-0.6wt% ND.

The inset shows the particle size range and their distribution. Neither a change in the average diameter of the particles nor further agglomeration on acid functionalization was noted. The TEM image of PVA-0.6 wt% ND in Fig. 3.1(c) shows that the dispersion is uniform. Thin film of polymer can be seen in the image.

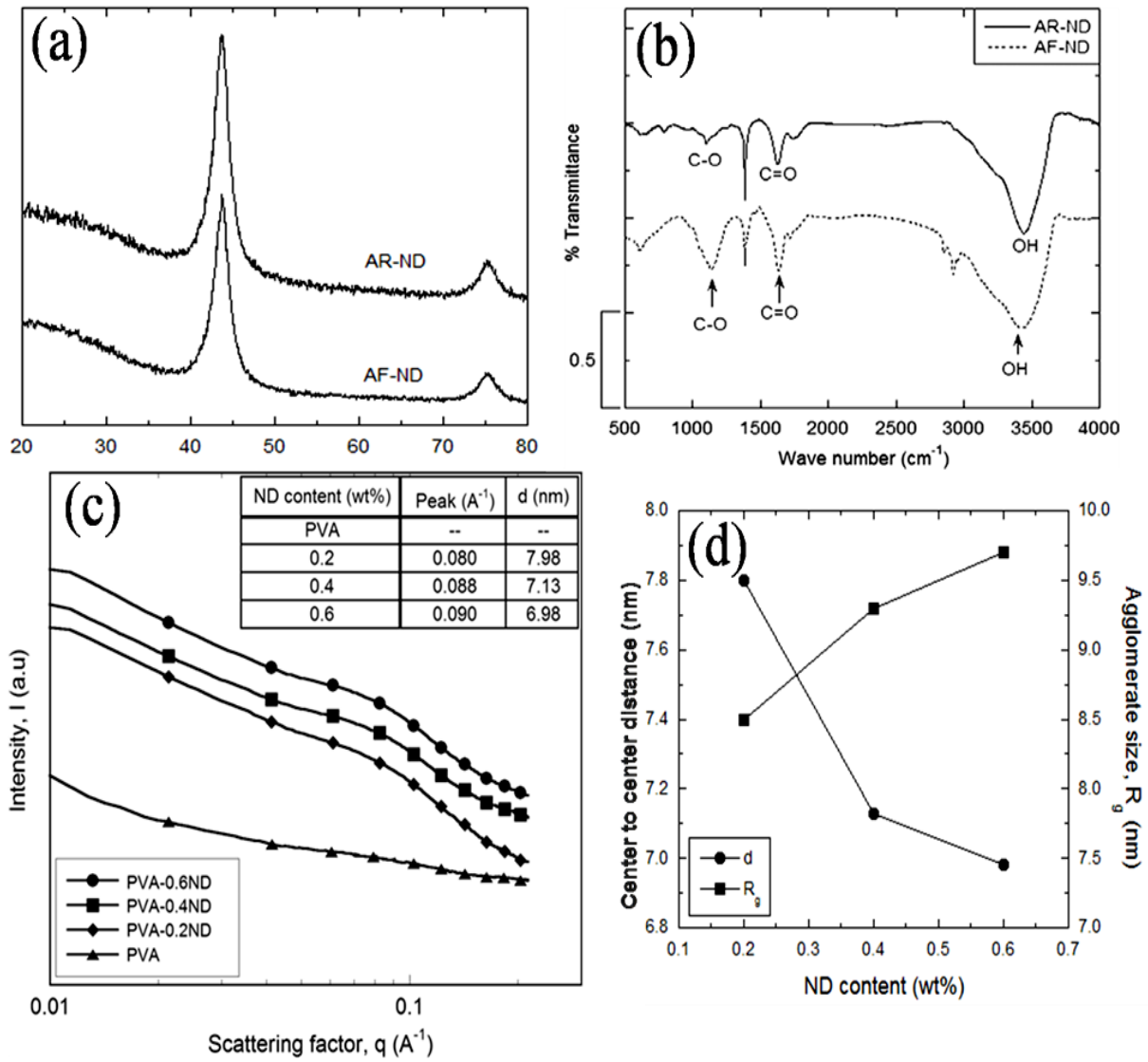

Figure 3.2 (a) XRD pattern, (b) IR-spectra of AR-ND and AF-ND, (c) SAXS curves of PVA and PVA-ND composites with table of the *q* and *d* values in the inset, (d) Variation of centre-centre distance and agglomerate size with wt% of ND.

The XRD patterns (Fig. 3. 2(a)) of the AR-ND and AF-ND yield similar results. Acid functionalization does not affect crystallinity of ND. The IR spectrum of the AR-ND shows characteristic -OH and C=O, C-O band peaks (Fig. 3.2(b)). This is because ND

during purification processes is treated with mineral acids. The intensity of these peaks increases upon acid-functionalization. Fig. 3.2(c) shows the SAXS data of the prepared films where the intensity is plotted as function of the scattering factor. The scattering factor, *q*, and the inter-particle distance, *d*, values are shown in the inset table (Fig. 3.2(c)). The inter-particle distance is calculated using the formulae $d = 2\pi/q$ and the radius of gyration is calculated using,

$$I = G\exp(\frac{-R_g^2 q^2}{3}) \qquad (1)\ [25]$$

The variation of interparticle separation and agglomerate size was plotted against wt% of ND in the polymer composite. The particle separation decreases by 11% and the agglomerate size increases by 14% with increasing ND concentration from 0.2 to 0.6 wt% (Fig. 3.2(d)).

DSC traces of the PVA-ND composites show (Fig. 3.3(a)) that there is no change in the melting temperature, T_m, of the composites with the addition of ND. The degree of crystallinity, χ, defined as the ratio of heat required to melt 1 g dry sample (obtained by integrating the area of the DSC curve between 220-235 ºC), ΔH, and the standard enthalpy of pure crystalline PVA, ΔH_C (~138.6 Jg^{-1}[6]), is plotted against the ND concentration in Fig. 3.3(b). It is seen from Fig. 3.3(b) that χ increases markedly first (by ~10% upon the addition of 0.2 wt% ND to PVA) and then increases gradually (from ~52.5 to 62% when ND concentration is increased from 0.2 to 0.6 wt%).

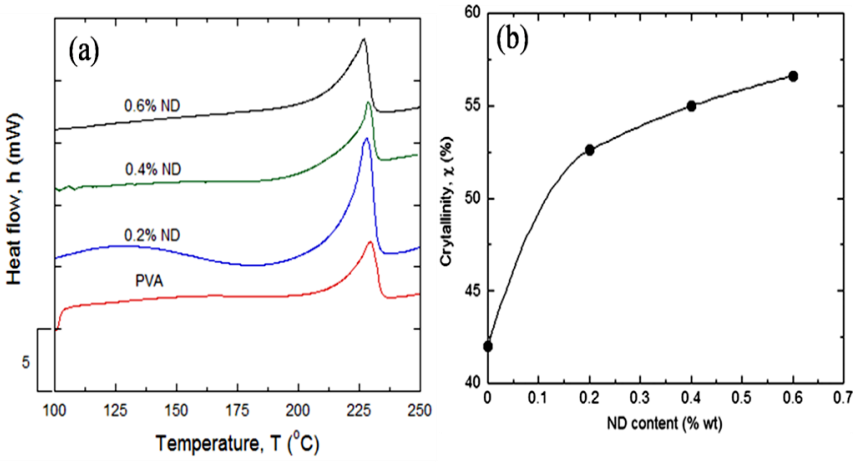

Figure 3.3 (a) DSC scans of PVA-ND composites showing the crystallization peak in the range of 220 - 235^{0}C, (b) Variation of degree of crystallinity (χ) with ND content in the polymer nanocomposites.

The hardness and elastic modulus calculated from stress strain curves are listed in Table 3.1. These values, normalized with the respective values of blank PVA (in order to highlight the relative changes in mechanical properties with the addition of ND), are plotted as against wt% ND in Fig. 3.4. It is evident that both *H* and *E* of the PVA increase significantly upon the addition of ND. In Fig. 3.4, it can be seen that the scatter in *E* is relatively large for 0.6 wt% ND composite. This is possibly due to the agglomeration of the ND particles at higher concentrations. While the average value of *H* increases by ~80%, *E* almost doubles with the addition of 0.6 wt% ND.

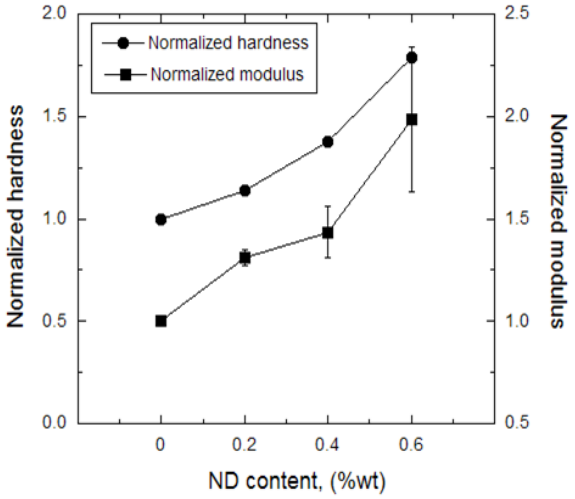

Figure 3.4
Variation of normalized hardness and modulus plotted as a function of ND content.

The mechanical response of a composite depends on many factors. These include,

(a) the size and distribution of the reinforcement phase in the matrix

(b) the characteristics of the interface between the reinforcement phase and the matrix.

Uniform distribution of the reinforcement phase is essential for obtaining high quality composites. Detailed characterization of the PVA-ND composites shows that the ND is distributed uniformly with no agglomeration. Since the size of the particle is of nm-scale, their number density (per unit volume) will be high, amplifying the strong interaction with molecular mechanisms of elastic as well as plastic deformation features of the polymer. The DSC results obtained in this study, which show increased crystallinity of the polymer with the ND addition, suggest that the adhesion between the polymer and the ND particles is strong, promoting crystallization of the matrix, which in turn enhances the mechanical response of the composite. In light of this, possible mechanisms responsible

for the enhancement in elastic and plastic properties of the PVA with the addition of ND are discussed below. Since the functionalized ND particles may form chemical bonds with the polymer chains, they affect the inter-chain bonding characteristics, making it difficult for the relative sliding to take place. In this context, it is worth noting that similar enhancements in *E* were reported PVA reinforced with few-layer graphene [7], or MWNT [5] or SiC nanowires [6]. Post fracture microscopy of the PVA-SiC nanowire composites by Vivekchand *et al.* [6] showed a thin layer of matrix on the filler material, indicating a strong interaction between the two. Similar interaction can be inferred in the present case as well, as a significant increase in the degree of crystallinity (by 14% with the additions of 0.6 wt% ND) was noted.

Similar arguments can be used to rationalize the enhancement in *H*, which reflects the resistance of the composite to plastic deformation. Again, the strong adhesion between ND and PVA due to functionalization of the former and ND crystallinity, favor effective load transfer. Another possible factor is that the hard ND resists the formation and/or propagation of shear bands, the primary mode of deformation in amorphous and semi-crystalline polymers, resulting in enhancement of hardness.

3.4.2. Binary composites:

In case of binary composites we have examined all possible combinations of the three reinforcements, ND + FG, FG + SWNT and ND + SWNT. The maximum content of the nanocarbon reinforcement was kept 0.6 wt% since higher levels of reinforcement only likely to cause agglomeration of the nanomaterials in the matrix, with different proportions of the major (0.4) and minor (0.2) nanocarbon additives. As discussed earlier better interaction of nanofillers with polymer enhances mechanical properties. To enhance interactions of the nanofillers with the matrix, surface functionalization of the the fillers was carried out. The IR-spectra of acid treated samples (Fig. 3.5(a)) shows presence of –OH and –COOH groups. In Fig. 3.5(b) DSC traces of all the composites have been plotted. Though all the samples have same melting point degree of crystallinity varies. Degree of crystallinity was determined from enthalpy of crystallization using the equation,

$$\chi = \frac{\Delta H_{exp}}{\Delta H_{fus}} \qquad (2)$$

where, χ is the degree of crystallinity, ΔH_{exp} is the experimentally determined value of change in enthalpy from the DSC curve and ΔH_{fus} is the enthalpy of fusion of the PVA (138.6 Jg^{-1}).

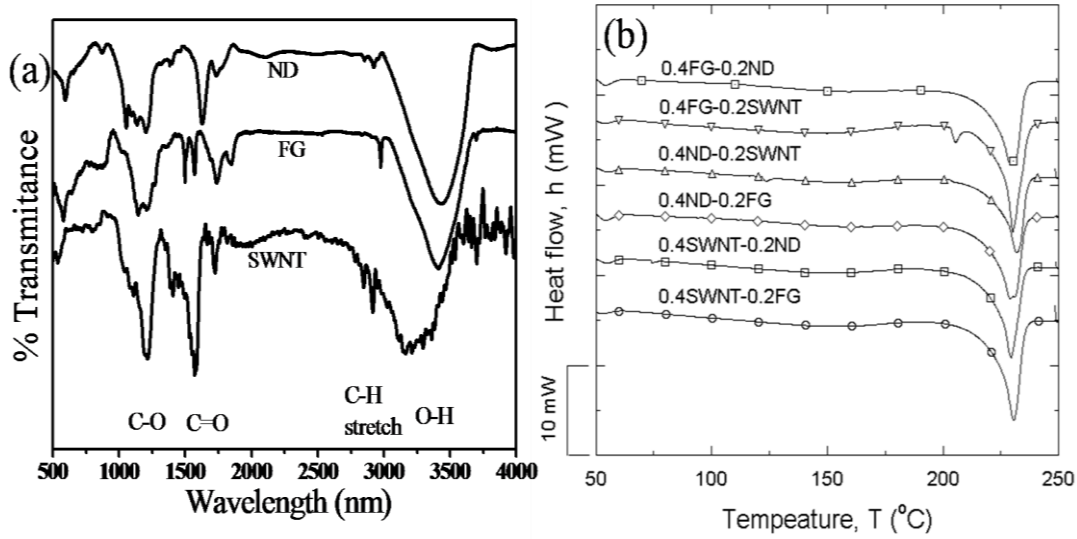

Figure 3.5 (a) IR-spectra of acid treated ND, FG, SWNT peak positions characteristic of various functional groups marked below, (b) DSC traces of the nanocomposites.

Variation of degree of crystallinity for composites containing single nanofillers has been is shown in Fig. 3.6(c). Nanocomposites containing FG show least value of χ, those with ND and SWNT have comparable values of χ. Highest degree of crystalinity is obtained in the sample with 0.6% of SWNT. In Figures 3.6 (a) and (b), we show the variation of the hardness, *H*, and the elastic modulus, *E*, of PMCs containing a single nanocarbon reinforcement as a function of the nanocarbon content. These data provide the reference for comparing the multipily reinforced composites investigated by us. All the three nanocarbons improve the mechanical properties of PVA markedly, addition of SWNT enhancing *H* by ~7 times and *E* by an order of magnitude. These enhancements are observed even with the addition of 0.2 wt% SWNT, the properties reaching a plateau on further increase in the SWNT content, probably due to the bundling of SWNTs at higher reinforcement content. Such bundling could reduce the effective interaction volume. Unlike the SWNT-PVA composites, the ND-PVA and FG-PVA composites show a

gradual increase in *E* and *H* with the increasing nanocarbon content, the rate of increase being higher in the former.

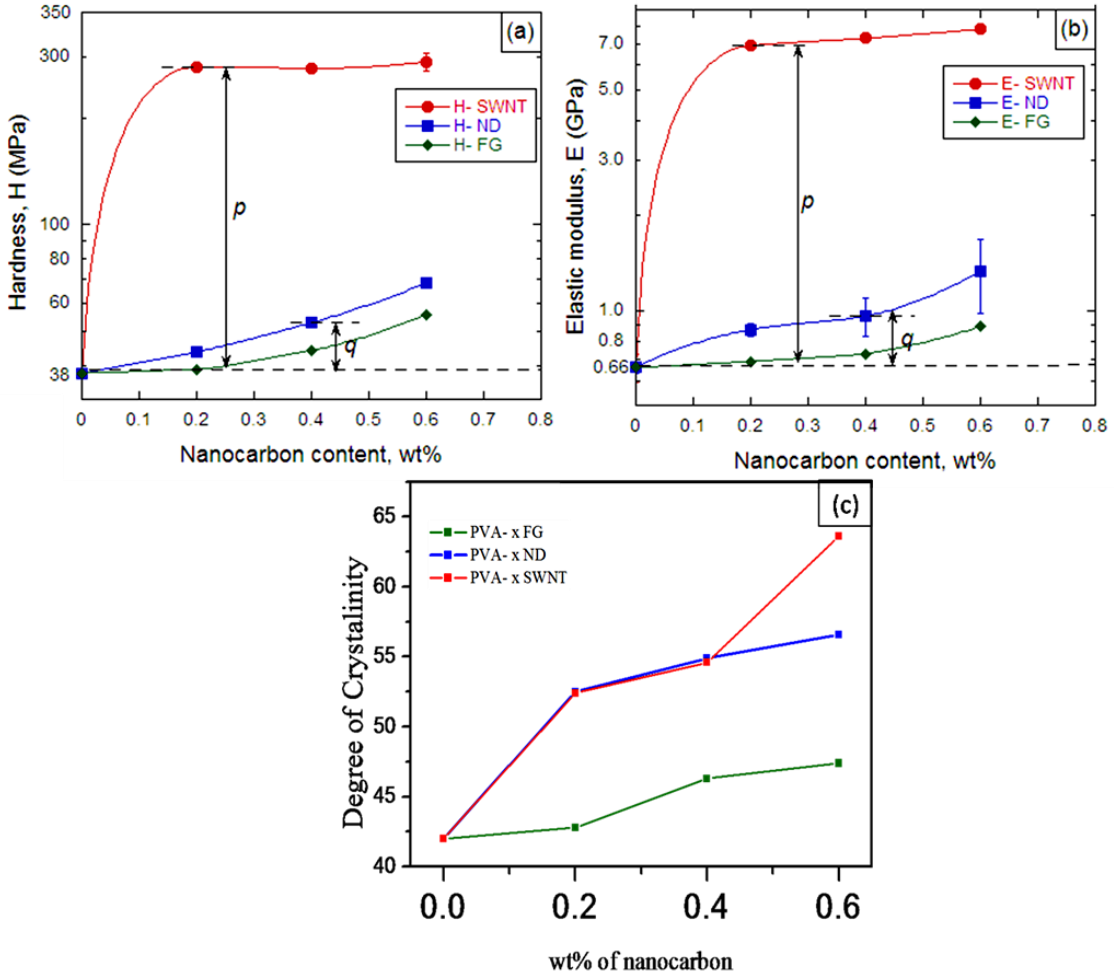

Figure 3.6 Mechanical properties of (a) hardness and (b) elastic modulus with the variation of nanocarbon content. (SWNT reinforced nanocomposites gives the superior mechanical properties compared to the FG and ND), (c) Variation of degree of crystallinity with addition of each nanocarbons to polymer matrices.

The enhancement in the mechanical properties of PVA is due to the inducement of crystallization of the polymer with the addition of the nanomaterials [5, 6, 7]. The values of mechanical properties are summarized in Table 3.1. The data reveal that the addition of a nanocarbon to PVA increases χ. To examine whether χ determines the enhancement in mechanical properties, we have plotted *E* and *H* against the relative change in χ in Fig. 3.7. The values of pure PVA (Table 3.1) , processed and evaluated under identical

conditions as those of the PMCs were used for reference. Fig 3.7 suggests that crystallinity and mechanical properties are related in ND- and FG containing PMCs. The mechanical properties of SWNT-containing PMCs seem to be independent of crystallinity.

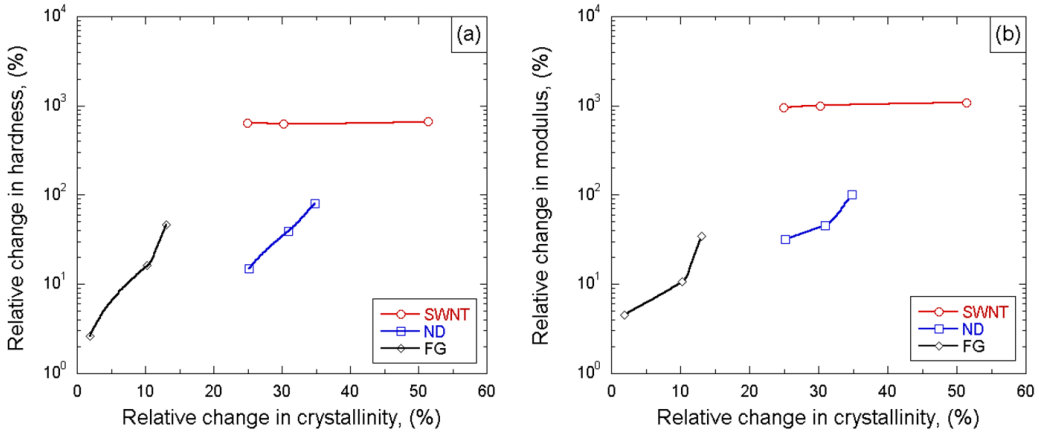

Figure 3.7 Variation of percentage relative change in the (a) hardness and (b) elastic modulus with the relative change in crystallinity.

Table 3.1. Values of Hardness (H), Ealastic modulus (E) and Degreeof crystallinity for nanocomposites with single nanocarbon filler.

Filler material	*Hardness (MPa)*	*Elastic modulus (GPa)*	*Degree of crystallinity (%)*
PVA	38.0 ± 0.01	0.66 ± 0.03	42.0
PVA-0.2 FG	39.0 ± 0.03	0.69 ± 0.03	42.8
PVA-0.4 FG	44.1 ± 0.03	0.73 ± 0.05	46.3
PVA-0.6 FG	55.7 ± 0.05	0.89 ± 0.08	47.4
PVA-0.2 ND	43.7 ± 0.01	0.87 ± 0.04	52.5
PVA-0.4 ND	52.8 ± 0.03	0.96 ± 0.13	54.9
PVA-0.6 ND	68.4 ± 0.02	1.33 ± 0.35	56.6
PVA-0.2 SWNT	277.8 ± 2.02	6.93 ± 0.05	52.4
PVA-0.4 SWNT	280.1 ± 9.82	7.30 ± 0.61	54.6
PVA-0.6 SWNT	290.2 ± 19.42	7.80 ± 0.34	63.6

Such large changes in the mechanical properties observed in SWNT-PVA composites have not been reported hitherto in the literature. There are a limited number of studies of

nanotube-polymer composites, and they generally involve high reinforcement content [17, 18, 26-30]. Furthermore, many of the studies pertain to composites reinforced by multi-walled carbon nanotubes. Liu *et al.* [27], who examined the PVA-0.8 SWNT composite, report an increase of 78% in *E* and of 48% in tensile strength, values much smaller than these observed by us in the present study. These workers did not observe any increase in crystallinity and attributed the enhancement in mechanical properties to the homogeneous distribution of fillers in the matrix. Zhang *et al.* [28] examined composites of PVA with KOH treated SWNTs and report that *H* and *E* increase by 78 and 110% respectively, whereas Li *et al.* [26] report 30% and 75% increases for the 5 wt% SWNT–epoxy composite. These workers observe that intercalation of the nanotubes is the cause for relatively poor enhancement in mechanical properties. Cadek *et al.* [5] have attributed the increase in mechanical properties of composites to the interfacial bonding between the matrix and the nanotubes as reflected by the increase in crystallinity. They also argue that the mechanical properties of the composites depend critically on the aspect ratio of the nanotubes, which in their case was ~100. In the present study, the SWNTs had aspect ratios of 700 to 1400. Furthermore acid functionalization of SWNTs could contribute to better bonding with the polymer, because of the presence of the surface carboxyl and hydroxyl groups. In Fig. 3.8 (a) and (b) the variations of hardness (*H*) and elastic modulus (*E*) has been plotted for two composite made of PVA-0.4%ND with various additions of FG and PVA-0.4FG-xND. For comparison *H* and *E* values for composites with single nanofillers has also been added. The composite PVA-0.4ND-xFG showed much improvement in properties compared to the composites made of either ND or FG. Similar trend is found in the modulus values. But *E* values reach steady state at large additions of FG. The synergistic effect is more pronounced at low concentrations of FG. To demonstrate it clearly independent effects (sum of individual effects for particular wt% of nanocarbons) and combined effect (experimental values) on *H* and *E* have been plotted in Fig. 3.8(c -f). However PVA-0.4FG-xND shows anomalous behaviour (Fig. 3.8(b)). Both *H* and *E* values increases up to 0.2% of ND and decreases with increasing ND (see highlighted parts in Fig 3.8(b), (d) and (f). On the basis of molecular dynamics simulations, Starr *et al* [31] and Smith *et a.l* [32] have shown that the high surface area of nanoparticles provides better interaction between the polymer chains and nanoparticles.

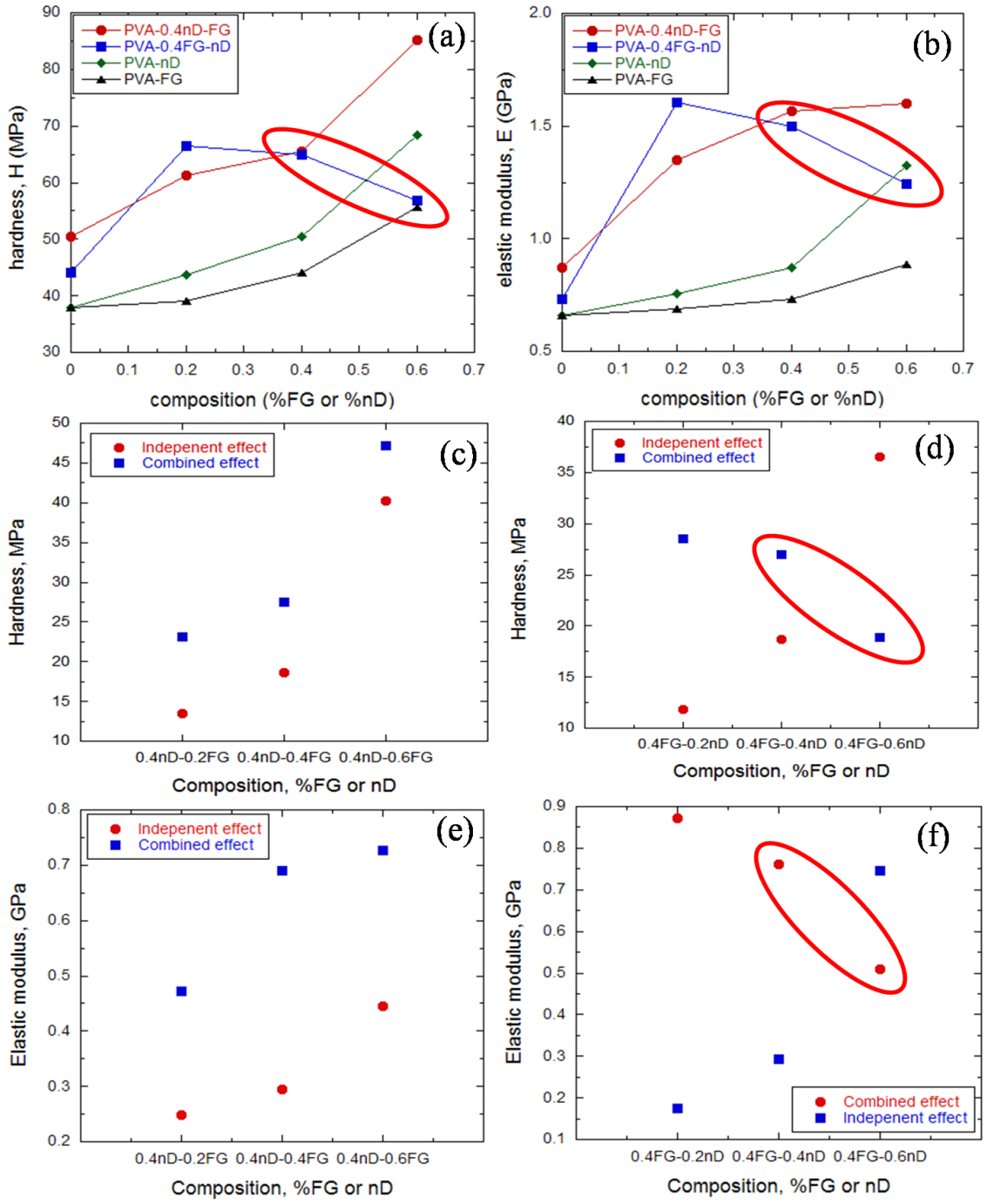

Figure 3.8 (a)Variation of hardness (*H*) and (b) Elastic modulus (*E*) for two binary composites PVA-0.4ND-xFG and PVA-0.4ND-xFG *H* and *E* values for composites with single nanofillers has been added for comparison. Comparison of (c-d) *H* and (e-f) *E* values of independent and combined effect for the two composites respectively.

This is due to the interaction of –OH and –COOH groups that are present on the acid-functionalized graphene with the –OH group present in the long chain polymers. Schniepp *et al.* [33] have found that the graphene sheets possess wrinkled structures and in between the wrinkles there are regions that have a surface roughness of ~0.4–0.5 nm. This surface roughness increases surface area of interaction wtih the phases when FG is dispersed in a polymer matrix. In the unreinforced polymer matrix, shear bands propagate unhindered as there are no barriers for their movement. In contrast, the presence of FG in the composites could offer resistance for the propagation of shear bands because of the high surface area it provides and there by greater interaction with the polymer. Inclusion of ND into the matrix reduces the effective surface area of FG interacting with the polymer. This is because some of the functional groups of FG might interact with functional groups on ND by covalent or non covalent interaction. Since interaction of the polymer matrix with graphene effectively reduces, *H* and *E* value also reduces.

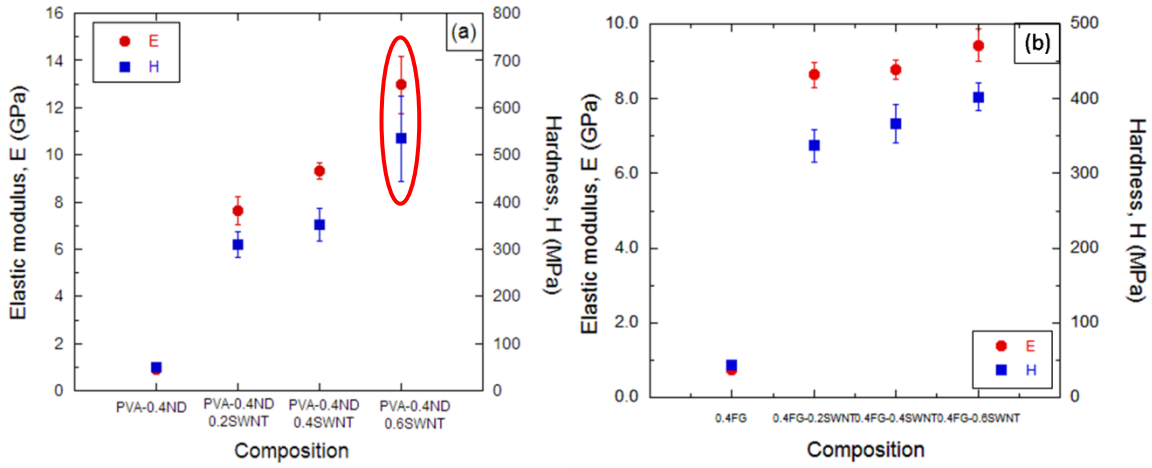

Figure 3.9 Variation of *H* and *E* for composites (a) PVA-0.4ND-xSWNT and (b) PVA-0.4FG-xSWNT.

In Fig. 3.9 we show the variation of *H* and *E* values for composites PVA-0.4ND-xSWNT and PVA-0.4FG-xSWNT. For both the cases there is significant increase in both *E* and *H* values from that of individual ones. Interestingly the *H* and *E* values of this composite PVA-0.4ND-0.6SWNT were found to be 534.3 ± 90.6 MPa and 12.96 ± 1.22 GPa, highlighted in Fig 3.9(a). These properties are superior to those of any

nanocarbon-polymer composites reported in the literature. A possible reason for the high *E* and *H* values in the PVA-0.4ND-0.6SWNT composite could be because that the ND particles prevent clustering of SWNTs due to van der Waals interactions. Surfactants are generally used to generate isolated SWNTs, here it appears ND particles are able to do the same, thereby preventing SWNT's to slide past each other.

What was notable was the fact that we gained synergistic benefits by adding two nanofillers of different diamensionalities to the polymer matrix. The synergistic benefit was estimated as follows, as exemplified in the case of the PVA-0.2SWNT-0.4ND composite. The addition of 0.2% SWNT alone to PVA leads to an enhancement in *H* or *E* of PVA by *p* as shown in Fig. 3.6. Likewise, *q* represents the enhancement in *H* or *E* of PVA due to the addition of 0.4 ND alone. The synergistic effect or % synergy attained by adding both 0.2% SWNT and 0.4% ND to PVA was computed by the relation,

$$\%\, synergy = [\, \mathrm{M_H} - \,(\mathrm{p} + \mathrm{q})] \times \frac{100}{(\mathrm{p+q})}$$

where, M_H is the measured value for the composite.

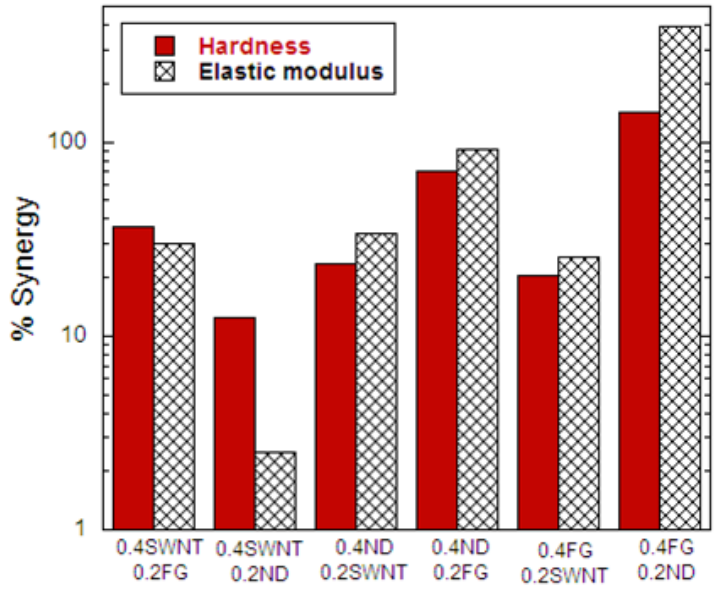

Figure 3.10 Percentage synergy in *H* and *E* for different binary composites.

In Fig. 3.10 we have plotted % synergy in hardness as well as elastic modulus for the different composites.The synergistic effect is dramatic in the ND plus FG composites, with 4 and 1.5 fold increases in *E* and *H*, respectively, in PVA-0.4FG-0.2ND composite. In the case of the PVA-0.4ND-0.2FG composite, synergistic effect is somewhat less, amounting to 92% and 71%, respectively, in *E* and *H*. The synergy is not as apparent in the SWNT plus ND composites since the addition of SWNT alone gives rise to fairly large values of *E* and *H*.

Table 3.2 Mechanical properties of the reinforced composites incorporating two nanocarbon fillers

Composite wt%	*Hardness (MPa)*	*Elastic modulus (GPa)*	*Synergy (%)*		*Degree of crystallinity (%)*
			Hardness (MPa)	*Elastic modulus (GPa)*	
0.4 SWNT + 0.2 FG	366.5 ± 23.9	9.3 ± 0.43	36.4	56.5	56.5
0.4SWNT + 0.2 ND	314.2 ± 10.15	7.5 ± 0.05	12.5	55.1	55.1
0.4FG + 0.2ND	66.4 ± 5.43	1.6 ± 0.1	141.4	55.1	55.1
0.4FG + 0.2SWNT	336.9 ± 22.21	8.6 ± 0.34	20.4	57.5	57.5
0.4ND + 0.2FG	61.18 ± 0.002	1.3 ± 0.07	71.1	54.8	54.8
0.4ND + 0.2SWNT	352.9 ± 34.78	9.3 ± 0.36	23.6	33.6	57.2

Values of *H* and *E*, % synergy and degree of crystallinity have been tabulated in Table 3.2. Variation in the percent crystallinity (%) of the PMCs with 2 nanocarbons is around ~2%, suggesting that increase in crystallinity is not the cause of the observed synergy. From Fig. 3.10, it is interesting to note that, in general, the synergistic benefits for both modulus and hardness accrue together. A possible reason for this strong correlation could be the fact that the nanocarbon reinforcements interact with the polymer chains at the molecular level. Such interaction not only enhances the polymer chain's stiffness (thereby increasing the composite's global modulus) but also its plastic flow resistance, which in turn leads to increased hardness. The present results suggest possible exciting ways of obtaining high performance polymer matrix composites. These results suggest possible new and exciting ways of obtaining high performance polymer matrix composites.

3.5 Conclusions:

We first prepared PVA polymer-matrix composites reinforced with small concentrations of functionalized ND. Detailed structural characterization, employing a variety of analytical techniques, shows that the nanoparticles are distributed uniformly and do not agglomerate. Further, they appear to interact with the polymer matrix strongly, increasing the crystallinity substantially. With only 0.6 wt% addition of ND, which is relatively small, significant enhancements to the hardness and Young's modulus of the PVA were observed. It was suggested that excellent adhesion between the matrix and the functionalized ND particles is the main reason for this marked improvement in mechanical performance. These results indicate that ND can be successfully used as a filler material for making polymer composites.

It was also possible to prepare composites of PVA with 2 nanocarbon additives. While nanodiamond, single-walled nanotubes, and graphene individually give rise to significant improvement in the mechanical properties of PVA, incorporation of binary combinations of these nanocarbons results in extraordinary synergy in mechanical properties. It was illuminating to understand that addition small amount of nanodiamond into nanocomposites of SWNT increases strength and stiffness further, simply because of the fact that ND can act like surfactant preventing bundelling of SWNT. We should point out, however, that our study has been limited to the measurements of hardness and elastic modulus and do not include ductility and toughness. In any case, our results suggest that it would indeed be profitable to explore polymer composites with such binary reinforcements.

Reference:

[1] L. H. Baekeland, *Sci. Am.* **1909**, 68, 322.

[2] C. Goodyear, *Dinglers Polytechnisches Journal* **1856**, 139, 376 .

[3] A. Usuki, M. Kojima, A. Okada, Y. Fukushima, O. Kamigaito, *J. Mater. Res.* **1993**, 8, 1179.

[4] Y. Kojma et al., *J. Mater. Res.* **1993**, 8, 1185.

[5] M. Cadek, J. N. Coleman, V. Barron, K. Hedicke, W. J. Blau, *Appl. Phys. Lett.* **2002**, 81, 1523.

[6] S.R.C. Vivekchand, U. Ramamurty, C.N.R. Rao, *Nanotechnology* **2006**, 17, 344.

[7] B. Das, K.E. Prasad, U. Ramamurty, C.N.R. Rao, *Nanotechnology* **2009**, 20, 125705.

[8] T. Ramanathan, A. A. Abdala, S. Stankovich, D. A. Dikin, M. Herrera-Alonso, R. D. Piner, D. H. Adamson, H. C. Schniepp, X. Chen, R. S. Ruoff, S. T. Nguyen, I. A. Aksay, R. K. Prud'Homme, L. C. Brinson, *Nature Nanotechnol.* **2008**, 3, 327.

[9] K.P. Ryan, M. Cadek, V. Nicolosi, S. Walker, M. Ruether, A. Fonseca, J.B. Nagy, W.J. Blau, J.N. Coleman, *Synthetic Metals* **2006**, 156, 332.

[10] T. Ramanathan, et al., *J. Polym. Sci. B* **2007**, 45, 2097.

[11] S.C. Tjong, *Mater. Sci. Eng. R* **2006**, 53, 73.

[12] V.Y. Dolmatov, *J. Superhard Mater.* 2007, 29, 65.

[13] T.S. Kurkin, et al., *Polym. Sci. Ser. A* **2008**, 50, 43.

[14] K.D. Behler, A. Stravato, V. Mochalin, G. Korneva, G. Yushin, Y. Gogotsi, *ACS Nano* **2009**, 3, 363.

[15] A.P. Korobko, N.P. Bessonova, S.V. Krasheninnikov, E.V. Konyukhova, S.N. Drozd, S.N. Chvalun, *Diam. Relat. Mater.* **2007**, 16, 2141.

[16] Z. Pitalský, et al., *Adv. Compos. Lett.* **2008**, 17, 29.

[17] *Nanomaterials Chemistry: Recent Development and New Directions* , C. N. R. Rao, A. Muller, A. K. Cheetham , Wiley-VCH, Weinheim , **2007**.

[18] *Nanotubes and Nanowires*, C. N.R. Rao, A. Govindaraj, Royal Society of Chemistry, London **2005**.

[19] C. N. R. Rao, K. Biswas, K. S. Subrahmanyam, A. Govindaraj, *J Mater Chem* **2009,** 19, 2457.

[20] S. R. C. Vivekchand, R. Jayakanth , A. Govindaraj A, C. N.R. Rao, *Small* **2005,** 1, 920.

[21] K. S. Subrahmanyam, A. Ghosh, A. Gomathi, A. Govindaraj, C. N. R. Rao, *Nanosci Nanotech Letts* **2009,** 1, 28.

[22] J.S. Pedersen, *J. Appl. Crystallogr.* **2004,** 37, 369.

[23] J. Kuljanin, M. I. C. Omor, V. Djokovic, J. M. Nedeljkovic, *Mater. Chem. Phys.* **2006,** 95, 67.

[24] W.C. Oliver, G.M. Pharr, *J. Mater. Res.* **1992**, **7,** 1564.

[25] A. Guinier, *Ann. Phys.* **1939,** 12, 161.

[26] X. Li, H. Gao, W. A. Scrivens, D. Fei, X. Xu, M.A. Sutton, A.P. Reynolds, M.L. Myrick, *Nanotechnology* **2004**, 15, 1416.

[27] L. Liu, A.H. Barber, S. Nuriel, H.D. Wagner, *Adv. Funct. Mater*. **2005**, 15, 975.

[28] X. Zhang, T. Liu, T.V. Sreekumar, S. Kumar, V.C. Moore, R.H. Hauge, R.E. Smalley, *Nano Letts* **2003**, 3, 1285.

[29] D. Qian, E.C. Dickey, R. Andrews, T. Rantell, *App. Phys. Lett.* **2000**, 76, 2868.

[30] X. Xu, M.M. Thwe, C. Shearwood, K. Liao, *App. Phys. Lett.* **2002**, 81, 2833.

[31] F.W. Starr, T.B. Schrode, S.C. Glotzer, *Macromolecules* **2002,** 35, 4481.

[32] G.D. Smith, D. Bedrov, L.W. Li, O.A. Byutner, *J. Chem. Phys.* **2002,** 117, 9478.

[33] H. C. Schniepp, J. L. Li, M. J. McAllister, *J. Phys. Chem. B* **2006,** 110, 8535.

CHAPTER 4

Surface-enhanced Raman scattering of molecules adsorbed on nanocrystalline Au and Ag films formed at the organic–aqueous interface

*Summary**

Surface-enhanced Raman scattering (SERS) of pyridine adsorbed on ultrathin nanocrystalline Au and Ag films generated at the liquid–liquid interface has been investigated. The shifts and intensification of bands formed with these films comprising metal nanoparticles are comparable to those found with other types of Au and Ag substrates. SERS of rhodamine 6G adsorbed on Ag films has also been studied. The results demonstrate that nanocrystalline metal films prepared by the simple method involving the organic–aqueous interface can be used effectively for SERS investigations.

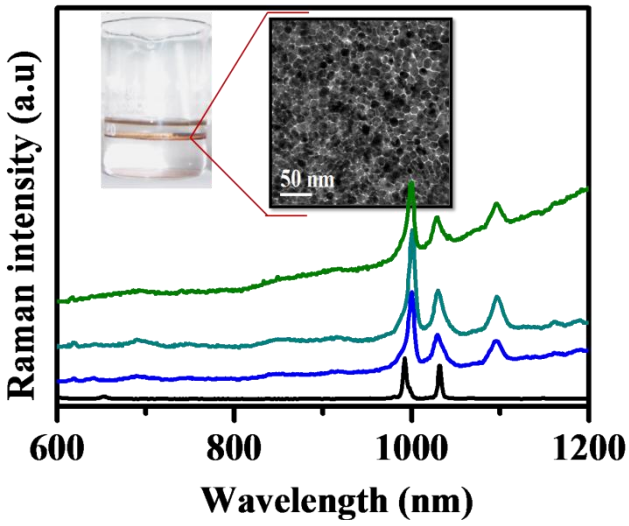

SERS obtained on films of Au nanoparticles formed at the organic-aqueous interface

A paper based on this study has appeared in: ***Chem. Phys. Lett.,* (*2009).***

4.1 Introduction:

Surface-enhanced Raman scattering (SERS) was discovered, though not recognized as such, by Fleischmann *et al.* [1] in 1974 who observed intense Raman scattering from pyridine adsorbed onto a roughened silver electrode surface from aqueous solution. Jeanmaire and Van Duyne[2] and Albrecht and Creighton[3] recognized independently that the large intensities observed could not be accounted for simply by the increase in the number of scatterers present and proposed that an enhancement of the scattered intensity occurred in the adsorbed state. Interestingly enough, these papers presaged a debate about the SERS mechanism which ran furiously for nearly a decade and about which research is still being conducted. Jeanmaire and Van Duyne tentatively proposed an electric field enhancement mechanism whereas Albrecht and Creighton speculated that resonance Raman scattering from molecular electronic states, broadened by their interaction with the metal surface, might be responsible. They were both right in concept, though not in detail.

In the next two decades SERS was observed for a variety of molecules adsorbed on the surfaces of relatively few metals in a variety of morphologies and physical environments. Silver, copper and gold have been far the dominant SERS substrates. The largest enhancements occur for surfaces which are rough on the nanoscale (10–100 nm). As a result of intense research activity mechanistic understanding of the primary observation - the 10^6 fold intensity enhancement of Raman scattering, also grew. The 1985 review article by Martin Moskovits, [4] eloquently summarizes the majority view of that time that the Raman enhancement factor, $EF = 10^6$ could be understood as the product of two major contributions: (1) an electromagnetic enhancement mechanism and (2) a chemical enhancement mechanism. Of course, there really are no other choices since the intensity of Raman scattering is directly proportional to the square of the induced dipole moment, μ_{ind} which, in turn, is the product of the Raman polarizability, α, and the magnitude of the incident electromagnetic field, E. As a consequence of exciting the localized surface plasmon resonance (LSPR) of a nanostructured or nanoparticulate metal surface, the local electromagnetic field is enhanced by say a factor of 10. Since Raman scattering approximately scales as E^4, the electromagnetic enhancement factor is of order 10^4. The chemical enhancement factor of 10^2 was viewed as arising from the excitation of adsorbate localized electronic resonances or metal-to-adsorbate charge transfer resonances (viz., resonance Raman scattering (RRS)). It is also worthwhile noting

that surface-enhanced resonance Raman scattering (SERRS) with combined SERS and RRS gives enhancement factors in the 10^9–10^{10} range.

Enormous enhancement in the Raman intensity, coupled with the suppression of fluorescence, suggests the possibility that SERS could provide an invaluable tool as a reliable, high-resolution detection technique for extremely minute quantities of target molecules. Indeed recent technical advances have shown the way to detection with enhancement factors as large as 10^{14} [5–11].

4.2 Scope of the present investigation:

Surface roughness, particle size and shape, the nature of the analyte and the wave length of laser excitation are the important factors that determine the magnitude of surface enhancement [12–17]. In early studies on SERS, roughened Au and Ag surfaces were used as substrates. SERS studies based on Ag [1,18–25], Au [18,19,26–29] and other metals such as Pt, Ru, Rh, Pd, Fe, Co and Ni [30–35] as well as the metallic oxide ReO_3 [36] have been reported. Since wider applications of SERS depend on the development of highly enhancing substrates, there have been efforts to develop improved substrates for enhancement. Thus, Yan and co-workers [37] used silver-coated zeolite crystals as SERS substrates while Wei et al. [38] found Ag films to be more Raman active than clusters or nanocrystals. Chaney et al. [39] found SERS activity of Ag nanorods arrays to depend on the length of the rods. Reproducibility of SERS signals from place to place on films is generally not satisfactory. Atomic layer deposition and template electrodeposition have been employed to obtain uniform and reproducible SERS signals from films [40, 41]. Wang and co-workers [42] have studied the effect of the morphology of Au films on the SERS signal. Bimetallic Au-Ag structures have also been employed as SERS substrates [43, 44]. Since films are desirable substrates for SERS, we considered it important to investigate SERS activity of molecules on nanocrystalline films of Au and Ag which can be readily prepared at the organic – aqueous interface [45–47]. This technique of preparing film substrates is simple and involves generating the metallic films at the interface by the reaction of a metal precursor in the organic phase with a reducing agent in the aqueous phase. The films so prepared contain nanoparticles of Au or Ag whose diameter can be varied by varying the temperature. Reaction parameters such as temperature, reaction time, concentrations of the metal precursor and the reducing agent, and the viscosity of the aqueous layer affect the nature and properties of the

nanocrystalline films [46, 47]. An additional advantage of the films generated at the interface is that they are easily transferred onto solid substrates. In this chapter, we present the results of our investigations of SERS of pyridine and rhodamine 6G on ultrathin nanocrystalline metallic films formed at the organic–aqueous interface.

4.3 Experimental Section:

4.3.1 Preparation of nanocrystalline films of Au and Ag:

Nanocrystalline films of gold were prepared using $Au(PPh_3)Cl$ (Ph = phenyl) and $Ag(PPh_3)_4NO_3$ as precursors by the literature procedure [48, 49]. Tetrakishydroxymethylphosphonium chloride (THPC) was used as the reducing agent. In a typical preparation, 10 mL of a 1.5 mM solution of $Au(PPh_3)Cl$ in toluene was allowed to stand in contact with 16 mL of 6.25 mM aqueous alkali in a 100 mL beaker at room temperature. Once the two layers stabilized, 330 μL of 50 mM THPC solution in water was injected into the aqueous layer using a syringe with minimal disturbance to the toluene layer. The onset of reduction was marked by a faint pink coloration of the toluene–water interface. The reduction was allowed to proceed without disturbance for 4 hours. With the passage of time, the color became more vivid, finally resulting in a robust elastic film at the liquid–liquid interface [35]. To vary the particle size, the films were formed at different temperatures. Films of Ag were prepared by a similar procedure [35]. Nanocrystalline films of gold were also prepared by using hydrazine hydrate (50 μL in 20 mL water) as the reducing agent, maintaining the temperature at 323 K. Au–Ag alloy films were prepared using the procedure reported in the literature [40]. Alloy formation was confirmed by changes in the visible spectra where in the plasmon band shifts with the composition. 1:1 ratio of metal precursors (1.5 mM) in 10 mL toluene formed the organic layer and 16 mL, 6.25 mM NaOH formed lower aqueous layer. 330 μL 50 mM THPC was used as reducing agent, and the temperature maintained at 348 K. The nanocrystalline films were characterized by transmission electron microscopy (TEM) and other techniques. The thickness of the films was generally around 60 nm. Properties of the films were entirely reproducible, provided the conditions of preparation were kept the same.

4.3.2 Raman measurements:

For SERS measurements, we used pyridine and rhodamine 6G (Rh6G) solutions in water. For each measurement 10 μL of the liquid analyte was dropped on nanocrystalline metallic film on a silicon wafer. Raman spectra were recorded with a LabRAM HR high-resolution Raman spectrometer (Horiba-Jobin Yvon) using a He-Ne laser (k = 632.8 or 514 nm). We have obtained relative enhancement ratios (*R*) of the adsorbate bands relative to those of the pure liquid [35, 51, 52] and have estimated the values of surface enhancement factor (*EF*). The relative enhancement ratio, *R*, is defined as the relative intensity of the Raman band of liquid analyte adsorbed on the nanocrystalline film divided by the relative intensity of corresponding band of liquid pyridine or Rh6G solution. The surface enhancement factor, *EF*, was calculated by the equation [3, 19],

$$EF = \left({}^{I_{SERS}}/_{I_{bulk}} \right) . \left({}^{N_{bulk}}/_{N_{ads}} \right) \quad (1)$$

where, I_{SERS}, I_{bulk} , N_{bulk} *and* N_{ads} respectively represent the measured SERS intensity of adsorbed molecules on the Au/Ag nanocrystalline film, the normal Raman intensity from the liquid analyte, the number of probe molecules under laser illumination in the bulk sample, and the number of probe molecules on the nanocrystalline film respectively. N_{ads} is calculated from the average radius of adsorbate nanoparticles, the surface density of the adsorbate molecule, the area of the laser spot, and surface coverage of adsorbate nanoparticles. N_{bulk} was obtained from the area of the laser spot, the penetration depth, the density of the analyte, and the molecular weight of the analyte. SERS measurements were made on different places of a given sample to ensure reproducibility of the results.

4.4 Results and discussion:

4.4.1 SERS of Pyridine on Au films:

We first carried out SERS of pyridine on nanocrystalline Au films generated at the liquid–liquid interface by using THPC as the reducing agent. In Fig. 4.1(a–c), we show TEM images of the Au nanocrystalline films formed at different temperatures. The Au particles in the films formed at 298, 313 and 348 K had average diameters of 10, 12 and 15 nm respectively. Films of Au particles were also prepared with other reducing agents

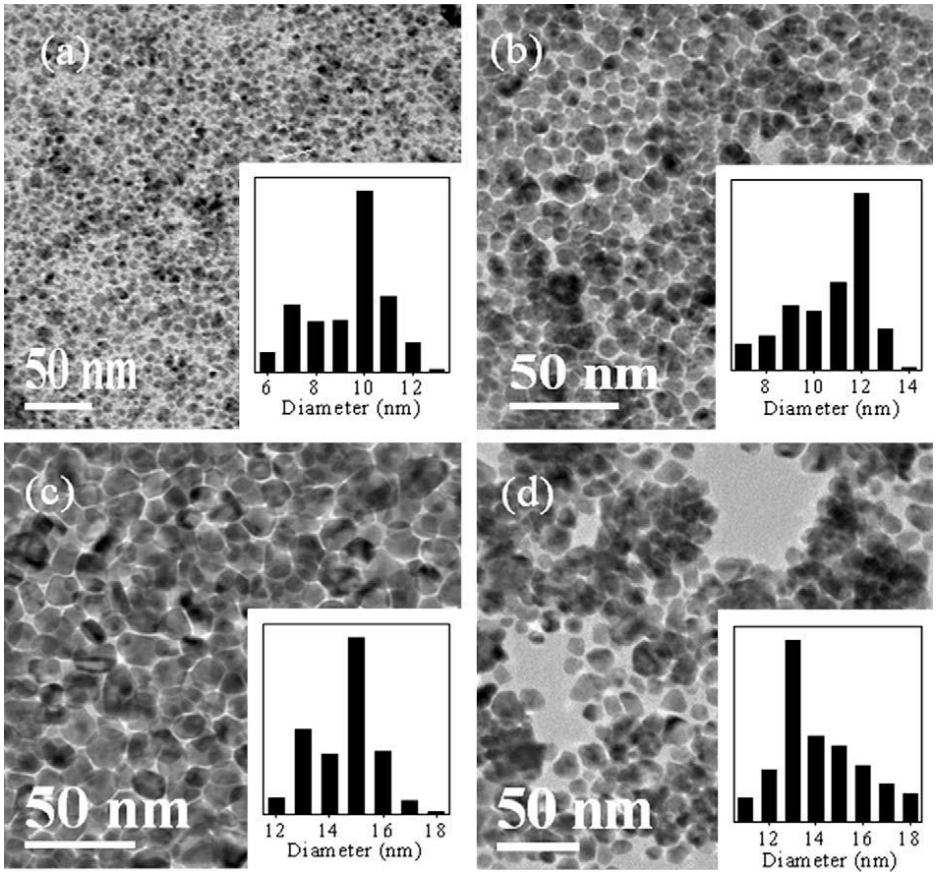

Figure 4.1 TEM images of the ultrathin nanocrystalline Au films obtained at the liquid–liquid interface using THPC as the reducing agent at (a) 298 K, (b) 313 K, (c) 348 K and of (d) with hydrazine hydrate as the reducing agent at 323 K. Histograms of particle size distribution are shown as insets.

like hydrazine hydrate formed at 323 K. TEM images of these films show that the nanocrystals had an average diameter of 13 nm. In Fig 4.2 we have plotted the Raman spectrum of pyridine on the Au nanocrystalline films containing particles of different diameters, along with the spectrum of the pure liquid. We clearly see SERS on the Au films. Thus, on adsorption of pyridine on the Au film containing particles of 15 nm diameter, we observe bands at 619 cm^{-1} (ν_{6a}, A1, asymmetric ring breathing), 689 cm^{-1} (ν_{6b}, B2, ring in plane deformation), 1001 cm^{-1} (ν_1, A1, symmetric ring breathing), 1030 cm^{-1} (ν_{12}, A1, trigonal ring breathing), 1096 cm^{-1} (ν_{18a}, A1) and 1298 cm^{-1} (ν_{9a}, A1, C–H in plane deformation) respectively. In Table 4.1, we compare the Raman band positions of pyridine on Au nanocrystalline films with different particle diameters along with their relative intensities. Data of liquid pyridine is given for comparison. We see that almost all the bands are shifted

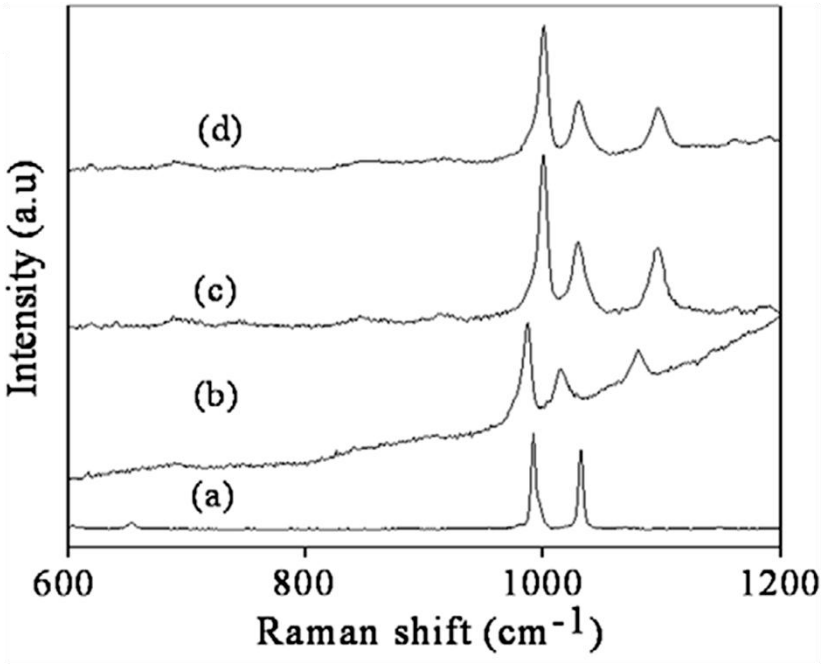

Figure 4.2 Raman spectra of pyridine (λ = 632 nm) (a) in the liquid state and on Au films with particles of diameter (b) 10, (c) 12 and (d) 15 nm prepared at toluene-water interface using THPC as the reducing agent.

to higher frequencies (relative to the positions of the pure liquid), except those at 1032, 1441 and 1482 cm^{-1}. The highest frequency shifts are exhibited by the bands at 652 (ν_{6b}, B2) and 1068 cm^{-1} (ν_{18a}, A1,). The highest intensity is found in the case of the symmetric ring breathing mode (ν_1) at 1001 cm^{-1}. The frequency of this mode is sensitive to weak σ donation and the large σ/π back donation. In the case of Au and other metals, the ν_1 mode is known to be shifted to higher frequencies, with the pyridine molecule in the end-on configuration (binding by nitrogen lone pair) [26, 35]. That we observe similar shifts of ν_1 in the present study, on adsorbing pyridine on the Au nanocrystalline films, suggests the end-on configuration for the adsorbed molecule. We also observe additional bands around 1190 and 1185 cm^{-1}. We have measured the relative enhancement ratios, R, of pyridine on the Au nanocrystalline films and found it to vary between 1.0 and 22, depending on the particle size (Table 4.1), the maximum values of R being found with the 12 nm particles. The SERS intensity is optimal when the particle size is small with respect to the wavelength of the exciting light as long as the size is not smaller than the electronic mean free path of the conduction electrons.

Table 4.1 Raman band positions (cm^{-1}) and relative enhancement ratios of pyridine on nanocrystalline Au films.

Liquid pyridine peak positions (relative intensity)	υ	*Films of 10 nm Au* [a] Peak positions (relative intensity)	R	*Films of 12 nm Au* [a] Peak positions (relative intensity)	R	*Films of 15 nm Au* [a] Peak positions (relative intensity)	R	*Films of 13 nm Au*[b] Peak positions (relative intensity)	R
604, A_1 (2)	6a	617 (7)	4	620 (3)	2	619 (4)	2	616 (1.5)	0.75
652, B_2 (5)	6b			689 (7)	1	689 (5)	1	653 (9)	2.0
992, A_1 (100)	1	692 (5)	1	1000 (100)	1	1001(100)	1	999 (100)	1
1032, A_1 (82)	12	1000 (100)	1	1029 (42)	0.5	1030 (41)	0.5	1033 (98)	1.2
1068, A_1 (2)	18a	1029 (39)	0.5	1097 (43)	22	1096 (33)	17	1096 (11.5)	6.0
1149, B_2 (2)	15	1096 (30)	15	1163 (4) 1191 (4)	2	1161 (5) 1190 (4)	3	1152 (3) 1185 (2)	1.5
1218, A_1(7)	9a					1298 (5)	0.7	1218 (8)	1
1441, B_2 (1)	19b			1437 (5)	5	1440 (3)	3	1436 (3)	3
1482, A_1 (2)	19a			1480 (3)	2	1483 (1)	0.5	1485 (2)	1
1573, B_2 (2)	8b			1572 (3)	2			1575(9)	4.5
1583, A1 (2)	8a	1586 (97)	49	1585 (21)	11	1585 (56)	28	1584(11)	5.5

a = by THPC route; b = by hydrazine hydrate route; υ = Wilson number. R = relative enhancement ratio

TEM images of Au films formed at 323 K with hydrazine hydrate as the reducing agent show that the nanocrystals had an average diameter of 13 nm (Fig. 4.1(d)). The Raman spectrum of pyridine on this nanocrystalline film is shown along with spectrum of pure pyridine in Fig. 4.3. We find the shifts and intensification of the pyridine bands on this Au film to be similar to those found with the films prepared with THPC (see Table 4.1). The R values of the pyridine bands vary in range 1–6.

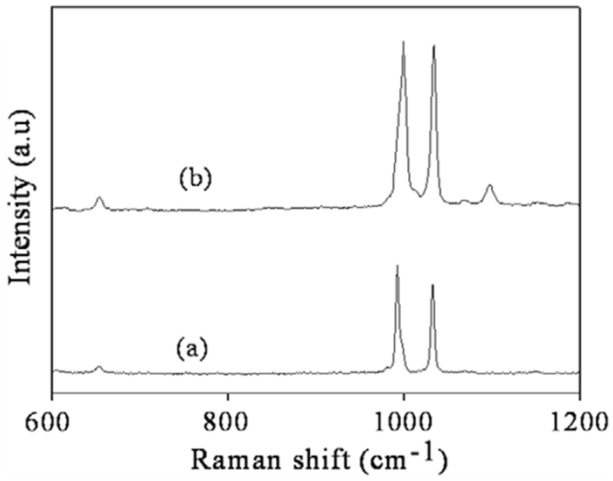

Figure 4.3 Raman spectra of pyridine (a) in liquid the state and (b) on 13 nm ultrathin nanocrystalline Au film prepared using hydrazine hydrate as the reducing agent (λ = 632 nm).

In order to calculate *EF*, we have used the value of monolayer surface density of pyridine [26] on Au as 4×10^{-10} mol.cm^{-2}. We have calculated *EF* values for the three most intense bands

in liquid pyridine spectra: ν_1 (992 cm^{-1}, A_1), ν_{12} (1332cm^{-1}, A_1) and ν_{18a} (1068 cm^{-1}, A_1). The EF values listed in Table 4.2 show that they are generally of the order of ~10^5 and comparable to those reported in other SERS studies [13].

Table 4.2 Selected Raman band positions (cm^{-1}) and enhancement factors (EF) of pyridine on nanocrystalline Au films

Liquid Pyridine peak positions (relative intensity)	υ	*Films of 10 nm Au*[a]		*Films of 12 nm Au*[a]		*Films of 15 nm Au*[a]		*Films of 13 nm Au*[b]	
		peak positions (rel intens)	EF	peak positions (relative intensity)	EF	peak positions (relative intensity)	EF	peak positions (relative intensity)	EF
992, A_1 (100)	1	1000 (100)	3.3×10^4	1000 (100)	2.3×10^4	1001(100)	4.0×10^4	999(100)	3.3×10^3
1032, A_1 (82)	12	1029 (39)	1.6×10^4	1029 (42)	1.2×10^4	1030 (41)	2.0×10^4	1033(98)	3.1×10^3
1068, A_1 (2)	18a	1096 (30)	4.6×10^5	1097 (43)	5.0×10^5	1096 (33)	6.0×10^5	1097(11.5)	2.9×10^4

a = by THPC route; b = by hydrazine hydrate route

4.4.2 SERS of Pyridine on Ag films:

We have measured SERS activity of pyridine on Ag nanocrystalline films formed at the liquid-liquid interface at 348K and containing particles with an average diameter of around 35 nm (see Fig. 4.4(a)) All the Raman bands of pyridine show shifts to higher frequencies on the Ag film (Fig. 4.4(b)), but the shifts are less than those on Au films.

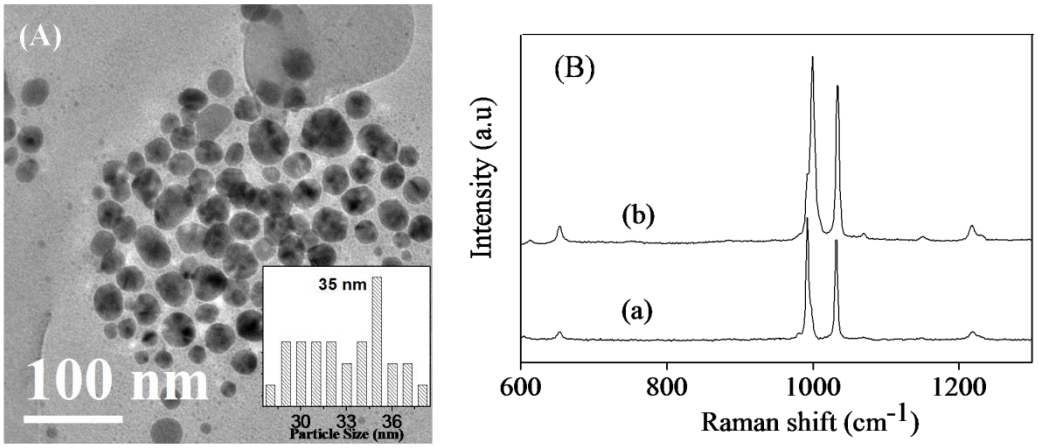

Figure 4.4 (A) TEM image of nanocrystalline film of Ag obtained at the liquid–liquid interface after 348K and particle size distribution, (B) Raman spectra of pyridine (λ=632 nm) (a) in the liquid state, and (b) on a ultrathin nanocrystalline Ag film with 35 nm particles.

The value of R varies between 1 to 3 while *EF* is 6.5×10^4 ,6.7×10^4 and 7.0×10^4 for the ν_1 (992 cm^{-1},A_1) , ν_{12}(1032 cm^{-1}) and ν_{18a} (1068 cm^{-1}, A_1) modes respectively. The intensity of the ν_{12} band gets enhanced much more on the Ag film than on the Au films. It is known that the potential energy distribution of the ν_{12} mode varies substantially for metals with different Fermi levels [13]. Unlike on the Au films where few of the pyridine bands show intensification, all the bands of pyridine show intensification in the case Ag, suggesting that EM enhancement plays a more important role and that chemical interaction between pyridine and Ag is relatively weak [13, 53]. In the case of Au films, however, both EM and chemical enhancements occur. Measurements of SERS of pyridine with films comprising nanoparticles of the 1:1 alloy of Au-Ag show *R* values comparable to those on Au and Ag films.

(A)

Liquid Pyridine peak positions (rel intens)	υ[a]	*Films of 35 nm Ag* Peak positions (rel intens)	R[b]
604, A_1 (2)	6a	612 (3)	2
652, B_2 (5)	6b	653 (9)	2
992, A_1 (100)	1	1000 (100)	1
1032, A_1 (82)	12	1033 (84)	1
1068, A_1 (2)	18a	1069 (2)	1
1149, B_2 (2)	15	1152 (2)	1
1218, A_1(7)	8a	1218 (9)	1
1441, B_2 (1)	19b		
1482, A_1 (2)	19a	1487 (3)	2
1573, B_2 (2)	8b	1576 (5)	3
1583, A_1 (2)	8a	1592 (5)	3

υ = Wilson number. R = relative enhancement ratio

(B)

Liquid Pyridine peak positions (rel intens)	υ[a]	*Films of 35 nm Ag* peak positions (rel intens)	EF[b]
992, A_1 (100)	1	1000(100)	6.5×10^4
1032, A_1 (82)	12	1033 (84)	6.7×10^4
1068, A_1 (2)	18a	1069 (2)	7.0×10^4

Table 4.3 (A) Raman band positions (cm^{-1}) and relative enhancement ratios of pyridine on nanocrystalline Ag films; (B) Selected Raman band positions (cm^{-1}) and enhancement factors (EF) of pyridine on nanocrystalline Ag films

4.4.3 SERS of Rhodamine6G on Ag films:

SERS activity of rhodamine-6G was investigated on the 35 nm Ag film, by recording the spectra with both 632 nm and 514 nm laser excitations, since the dye shows strong fluorescence with an absorbance maximum at 520 nm. Figure 4.5 shows

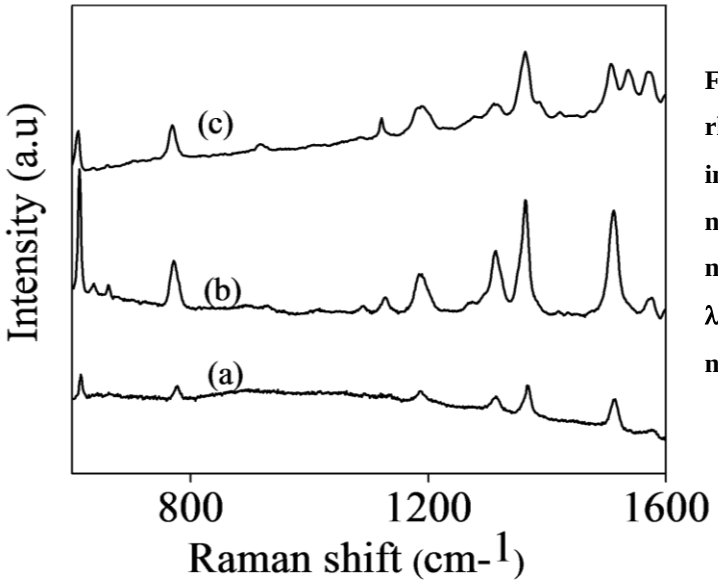

Figure 4.5 Raman spectra of rhodamine 6G (in water) (a) in the liquid state (λ= 632 nm) and on the nanocrystalline Ag film with λ of (b) 632 nm and (c) 514 nm.

Table 4.4 Raman band positions (cm^{-1}) and relative enhancement ratios of Rhodamine6G on nanocrystalline Augfilms

Liquid R6G peak positions (rel intens)	υ	*Films of 35nm Ag*			
		Peak positions (rel intens) 632nm laser	R	Peak positions (rel intens) 514nm laser	R
615 (81)	53	612(109)	1.4	610(59)	0.72
	54	636 (8)		635(3)	
662 (14)	55	661(13)	1.0	659(4)	0.28
				705(2)	
778(43)	65	771(41)	1	768(46)	1.1
				917(10)	
1091(10)	94	1091(8)	0.8	1085(4)	0.4
1133(12)	97	1127(15)	1.3	1121(28)	2.4
1187(36)	103	1184(35.5)	1	1184(37)	1
				1191(39)	
	110	1270 (1)		1277(6)	
	111	1273 (2)			
	112	1293 (2)		1310(20)	
1314(43)	115	1313(56)	1.3	1315(19)	0.4
1367(100)	117	1363(100)	1	1363(100)	1
				1385(25)	
	127	1419 (4)		1421(9)	
	128	1435 (3)		1449(4)	
	139	1476 (1)			
1515(100)	146	1512(96)	1	1508(48)	0.5
	147	1532 (0.5)		1536(35)	
1575(23)	151	1574(26)	1.1	1570(42)	1.8
1600(12)	152	1600(17)	1.4	1598(12)	1
	153	1612 (2)		1612(2)	
1654(42)	154	1651(52)	1.2	1650(126)	3

the Raman spectra of 10^{-2} M rhodamine 6G (in water) adsorbed on the Ag film using both 632 nm and 514 nm laser excitations. The spectrum of the pure liquid is shown for comparison. On adsorption of rhodamine 6G on the Ag film, we observe a large number of bands, all shifted to lower frequencies [53] .We also observe additional bands at 636 , 1270 ,1293 and 1476 cm^{-1} . The two most intense bands of rhodamine 6G 1367 cm^{-1} [υ(CC) + υ(CN)] and 1515 cm^{-1} [υ(CC)] are shifted to 1363 cm^{-1} and 1512 cm^{-1} respectively on adsorption on the Ag film. The band positions relative intensities and values of R for adsorbed R6G on Ag film is noted down in Table 4.4. The R values of rhodamine 6G on Ag vary between 1.0 to 1.4. The EF values for the four most intense bands of rhodamine 6G ν_{53} at 615 cm^{-1}, ν_{115} at 1314cm^{-1}, ν_{117} at 1367 cm^{-1} and ν_{146} at 1515cm^{-1} was found to be of the order of 10^4 (see Table 4.5).

Table 4.5 Selected Raman band positions (cm^{-1}) and enhancement factors (EF) of Rhodamine6G on nanocrystalline Ag films

Liquid R6G peak positions (rel intens)	υ	*Films of 35nm Ag*			
		peak positions (rel intens) 632nm Laser	EF	peak positions (rel intens) 514nm Laser	EF
615(81)	53	612(109)	1.4×10^4	610(59)	4.4×10^3
1314(43)	115	1313(56)	1.3×10^4	1363(100)	1.4×10^4
1367(100)	117	1363(100)	1×10^4	1508(48)	2.9×10^3
1515(100)	146	1512(96)	1×10^4	1650(126)	1.5×10^4

4.4 Conclusions :

The results of the present study show that nanocrystalline films of Au and Ag generated at the organic-aqueous interface can be used as substrates for SERS studies of molecules. The intensity enhancement and band shifts of pyridine found on these thin films are comparable to those reported for other Au and Ag substrates. The ease with which nanocrystalline metal films are prepared at the interface favour their use for SERS studies.

Reference:

[1] M. Fleischmann, P. J. Hendra , A. J. McQuillan, *Chem. Phys. Lett.* **1974**, 26, 163.

[2] D. L. Jeanmaire, R. P. Van Duyne, *J. Electroanal. Chem.* **1977**, 84, 1.

[3] M. G. Albrecht, J. A. Creighton, *J. Am. Chem. Soc.* **1977**, 99, 5215.

[4] M. Moskovits, *Rev. Mod. Phys.* **1985**, **57**, 783.

[5] S. Nie, X S. R.Emory, *Science* **1997**, 275, 1102.

[6] K. Kneipp, Y. Wang, H. Kneipp, L. Perelman, I. Itzkan, R. R. Dasari, M. S. Feld, *Phys. Rev. Lett.* **1997**, 78, 166755.

[7] H. Xu, E. Bjerneld, M. Ka¨ ll, L. Bo¨ rjesson, *Phys. Rev. Lett.* **1999**, 83, 4357.

[8] G. C. Schatz, M. A. Young, R. P. Van Duyne, *Topics in Applied Physics*, In *Surface Enhanced Raman Scattering: Physics and Applications* K. Kneipp, M. Moskovits, H. Kneipp, Eds. Springer: Berlin **2006,** 103, , p 19.

[9] A. M. Michaels, J. Jiang, L. E. Brus, *J. Phys. Chem. B* **2000**, 104, 11965.

[10] K. A. Bosnick, J. Jiang, L. E. Brus, *J. Phys. Chem. B* **2002**, 106, 8096.

[11] J. Jiang, K. Bosnick, M. Maillard, L. Brus, *J. Phys. Chem. B* **2003**, 107 , 9964.

[12] R.K. Chang, T.E. Furtak, *Surface Enhanced Raman Scattering*, New York, Plenum Press, **1982**.

[13] Z.Q. Tian, B. Ren, D.Y. Wu, *J. Phys. Chem. B* **2002** 106, 9463.

[14] M.J. Moskovits, *Raman Spectrosc.* **2005,** 36, 485.

[15] K. Kneipp, H. Kneipp, I. Itzkan, R.R. Dasari, M.S. Feld, *Chem. Rev.* **1999,** 99, 1957.

[16] C.J. Orendorff, A. Gole, T.K. Sau, C.J. Murphy, *Anal. Chem.* **2005,** 77, 3261.

[17] A. Campion, P. Kambhampati, *Chem. Soc. Rev.* **1998,** 27, 241.

[18] C. Lee, S.J. Bae, M. Gong, K. Kim, S.W. Joo, *J. Raman Spectrosc.* **2002,** 33, 429.

[19] C.J. Orendorff, L. Gearheart, N.R. Jana, C.J. Murphy, *Phys. Chem. Chem. Phys.* **2006,** 8, 165.

[20] M. Kerker, *Pure Appl. Chem.* **1984,** 56, 1429.

[21] R. Dornhaus, M.B. Long, R.E. Benner, R.K. Chang, *Surf. Sci.* **1980,** 93, 240.

[22] M.M. Miranda, N. Neto, G. Sbrana, *J. Phys. Chem.* **1988,** 92, 954.

[23] H.H. Wang et al., *Adv. Mater.* **2006,** 18, 491.

[24] A.M. Michaels, M. Nirmal, L.E. Brus, *J. Am. Chem. Soc.* **1999,** 121, 9932.

[25] K.A.B. Snick, J. Jiang, L.E. Brus, *J. Phys. Chem. B* **2002,** 106, 8096.

[26] A.G. Brolo, D.E. Irish, J. Lipkowski, *J. Phys. Chem. B* **1997,** 101, 3906.

[27] N. Félidj, S. Lau Truong, J. Aubard, G. Lévi, J. R. Krenn, A. Hohenau , A. Leitner, F. R. Aussenegg, *J. Chem. Phys.* **2004,** 120, 7141.

[28] X.C. Yang, Y. Fang, *J. Phys. Chem. B* **2003,** 107, 10100.

[29] Z. Zhu, T. Zhu, Z. Liu, *Nanotechnology* **2004,** 15, 357.

[30] B. Ren, Q.J. Huang, W.B. Chai, B.W. Mao, F.M. Liu, Z.Q. Tian, *J. Electroanal. Chem.* **1996,** 415,175.

[31] J.S. Gao, Z.Q. Tian, *Spectrochim. Acta* A **1997,** 53 1595.

[32] Q.J. Huang, J.L. Yao, R.A. Gu, Z.Q. Tian, *Chem. Phys. Lett.* **1997,** 271, 101.

[33] P. G. Cao, J. L. Yao, B. Ren, B. W. Mao, R. A. Gu, Z. Q. Tian, *Chem. Phys. Lett.* **2000,** 316 1.

[34] D.Y. Wu, Y. Xie, B. Ren, J.W. Yan, B.W. Mao, Z.Q. Tian, *Phys. Chem. Commun.* **2001,** 18 1.

[35] C. Zou, P.W. Jagodzinski, *J. Phys. Chem. B* **2005,** 109, 1788.

[36] K. Biswas, S.V. Bhat, C.N.R. Rao, *J. Phys. Chem. C* **2007,** 111, 5689.

[37] W. Yan, L. Bao, S.M. Mahurin, S. Dai, *Appl. Spectrosc.* **2006,** 58, 18.

[38] G. Wei, H. Zhou, Z. Liu, Z. Li, *Appl. Surf. Sci.* **2005,** 240, 260.

[39] S.B. Chaney, S. Shanmukh, R.A. Dluhy, Y.P. Zhao, *Appl. Phys. Lett.* **2005,** 87, 031908.

[40] J.A. Dieringer et al., *Faraday Discuss.* **2006,** 132, 9.

[41] M. E. Abdelsalam, P. N. Bartlett, J. J. Baumberg, S. Cintra, T. A. Kelf, A. E. Russell, *Electrochem. Commun.* **2005,** 7, 740.

[42] C. H. Wang, D. C. Sun, X. H. Xia, *Nanotechnology* **2006,**17, 651.

[43] S.E. Hunyadi, C.J. Murphy, *J. Mater. Chem.* **2006,** 16, 3929.

[44] Y. Wang, H. Chen, H. Dong, E. Wang, *J. Chem. Phys.* **2006,** 125, 044710.

[45] C.N.R. Rao, G.U. Kulkarni, P.J. Thomas, V.V. Agrawal, P. Saravanan, *J. Phys. Chem. B* **2003,** 107, 7391.

[46] C.N.R. Rao, G.U. Kulkarni, V.V. Agrawal, U.K. Gautam, M. Ghosh, U. Tumkurkar, *J. Colloid Interface Sci.* **2005,** 289, 305.

[47] C.N.R. Rao, K.P. Kalyanikutty, *Acc. Chem. Res.* **2008,** 41, 489.

[48] P. Braunstein, H. Lehner, D. Matt, *Inorg. Synth.* **1990,** 7, 218.

[49] M. Khan, C. Oldham, D.G. Tuck, *Can. J. Chem.* **1981,** 59, 2714.

[50] V.V. Agrawal, P. Mahalakshmi, G.U. Kulkarni, C.N.R. Rao, *Langmuir* **2006,** 22,1846.

[51] S. Astilean, M. Bolboaca, D. Mainu, T. Iliescu, *Romanian Rep. Phys.* **2004,**56, 346.

[52] P. Hildebrandt, M. Stockburger, *J. Phys. Chem.* **1984,** 88, 5935.

[53] H. Watanabe, N. Hayazawa, Y. Inouye, S. Kawata, *J. Phys. Chem. B* **2005,** 109, 5012.

CHAPTER 5

Scaling behavior of plasmon coupling in Au nanoparticles incorporated in polymer matrices

*Summary**

Polymer nanocomposite films containing different concentrations of Au nanoparticles have been prepared. Centre to centre distance between Au nanoparticles embedded in polymer matrix was determined by small angle X-ray scattering. Surface plasmon resonance band positions of these films were studied by electronic absorption spectroscopy. The variation in the surface plasmon resonance (SPR) band of Au nanoparticles with concentration is described by a scaling law.

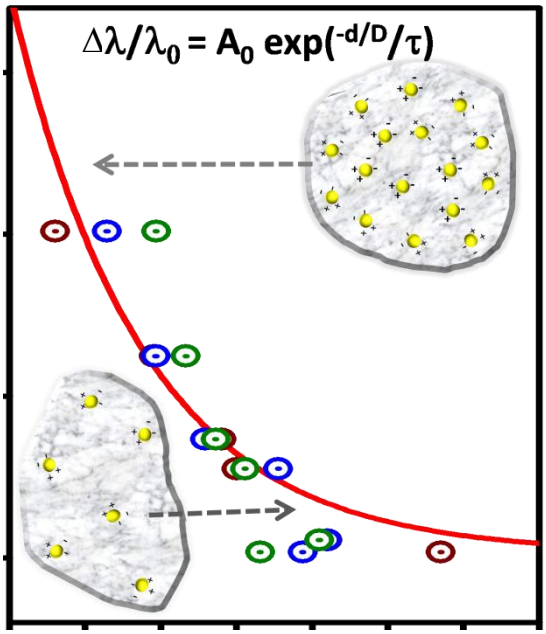

Distance dependence of plasmon coupling in polymer composites of metal nanoparticles

**** A paper been submitted for publication.***

5.1 Introduction:

All metal nanoparticles interact strongly with visible light through the resonant excitations of the collective oscillations of the conduction electrons within the particles. As a result, local electromagnetic fields near the particle can be many orders of magnitude higher than the incident fields, and the incident light around the resonant-peak wavelength is scattered very strongly. This coherent oscillation of the metal electrons in resonance with light of a certain frequency constitutes what is known as localized surface plasmon resonance (LSPR). The LSPR results in a strongly enhanced electric field (*near-field*) localized at the particle surface. For Au and Ag nanoparticles the oscillation frequency is usually in the visible region giving rise to the strong SPR absorption with absorption maxima at 520 and 420 nm respectively.

When anisotropy is added to a nanoparticle the surface geometry changes causing a shift in the electric field density on the surface. This causes a change in the oscillation frequency of the electrons, generating different cross-sections for the optical properties including absorption and scattering. Changing the dielectric constant of the surrounding material also has an effect on the oscillation frequency due to the varying ability of the surface to accommodate electron charge density from the nanoparticles. Chemically bonded molecules can be detected by the observed change they induce in the electron density on the surface, which results in a shift in the surface plasmon absorption maximum. This is the basis for the use of noble metal nanoparticles as sensors [1, 2].

The enhanced electric fields are confined within only a tiny region of the nanometer length scale near the surface of the particles and decay significantly thereafter. This localized field enhancement provides a field gradient that is much greater than that of any far-field optical tweezers; therefore, it may be possible to trap single molecules or other nanoparticles in regions near an elliptical metal nanoparticle [3-5] or between two nanoparticles[6]. The discovery of surface-enhanced Raman scattering (SERS) that is Raman scattering enhanced by resonantly excited metal nanoparticles has opened up applications to molecular detection [7-9]. SERS has reached a sensitivity of upto single molecule detection [10, 11] making possible biochemical sensing and detection of very small analyte. In typical SERS experiments, a collection of colloidal particles of various sizes are induced to aggregate, and those aggregates that happen to be resonantly

excited by the illuminating laser are called "hot spots". Therefore, from a practical point of view, it is very important to be able to fabricate optimally designed plasmon configurations of interacting nanoparticles. Plasmonic properties of assemblies of Au nanoparticles therefore generate a lot of interest.

5.2 Scope of the present investigation:

Several studies on assemblies of Au nanoprticles have established that the plasmonic properties are strongly dependent on interparticle interactions [12-17]. The magnitude of the assembly-induced plasmon shift depends on the strength of the interparticle dipolar plasmon coupling, which, in turn, depends on the proximity of the individual nanoparticles. The plasmon shift thus gives a measure of the distance between the particles [18-20]. Sonnichsen *et al.* [19] and Reinhard *et al.* [20] have utilized this feature to design a plasmon ruler equation to measure nanoscale distances in biological systems on the basis of the spectral shift resulting from the coupling of two gold nanoparticles by a defined biomolecular binding scheme. There have been a few quantitative studies on the distance dependence of dipolar plasmon coupling, observed as shift in the SPR band and a universal scaling behaviour seems to operate in systems in which metal particles are separated by a dielectric gap [21-25]. Such studies have been carried out on lithographically fabricated Au nanodiscs in polymers [21, 22], dielectric core-Au nanoshells [23, 24], head-to-tail dimers of elongated particles of different aspect ratios and curvatures and a trimer of nanospheres [25]. However it would be of interest to see if the same law holds good for metal particles frozen in polymer matrices. In order to study this we prepared Au nanoparticles synthesized in situ in polymer matrix and determined the inter-particle separation by Small Angle X-ray Scattering (SAXS). Inter-particle separation was varied simply by concentration variation. From SAXS data we also obtain other distances of the Au nanoparticle aggregates. SPR band positions were measured to study the shift in plasmon with concentration of Au nanoparticles in polymer matrix.

5.3 Experimental Section:

Au-PVA nanocomposites with 1-3.5 weight percent of Au nanoparticles were prepared in situ. For the synthesis of Au nanoparticles we followed Turkevich's method with slight modification [26, 27]. In a typical synthesis, 1 g of PVA was dissolved in 20 ml of water by warming it slightly. Calculated amounts of 1.0 mM $HAuCl_4$ solution was added to the polymer solution. 1% sodium citrate solution (1ml per 5 ml of $HAuCl_4$ solution) was then added to it and stirred at room temperature for 30 mins. The mixture was then dried in Petri dishes at 35-40°C for 3 days.

The polymer nanocomposites were characterized using x-ray diffraction (XRD), electronic absorption spectroscopy, field emission scanning electron microscopy (FESEM), energy dispersive x-ray spectroscopy (EDAX) and transmission electron microscopy (TEM). TEM studies of Au-PVA films were conducted by re-dissolving the films in water and drying a drop of this on a holey carbon-coated copper grid and were observed in a JEOL JEM 3010 microscope. FESEM images were obtained using a FEI NOVA NANOSEM 600. Samples for FESEM were prepared by directly drying the polymer-nanoparticle solution over silicon substrates. Electronic absorption spectra were recorded using a Perkin-Elmer Lambda 900 UV/VIS/NIR spectrometer. SAXS measurements were carried out with Bruker-AXS NANOSTAR instrument. The instrument has X-ray tube (Cu Kα radiation, operated at 45 kV/35 mA), cross-coupled Göbel mirrors, three-pinhole collimation, evacuated beam path, and a 2D gas-detector (HI-STAR). SAXS data were recorded in the q range of 0.007 to 0.21 $Å^{-1}$, (i.e, 2θ = 0.1 to 3°).

5.4 Results and discussion :

Figure 1(a) shows a TEM image of the 2 % Au-PVA film along with the particle size distribution. The Au nanoparticles had an average particle diameter of 9 nm. An FESEM image of the polymer Au nanocomposite film shown in Fig. 1(b)

reveals small aggregates of Au nanoparticles with an average size of 50 nm (~ 20 particles).

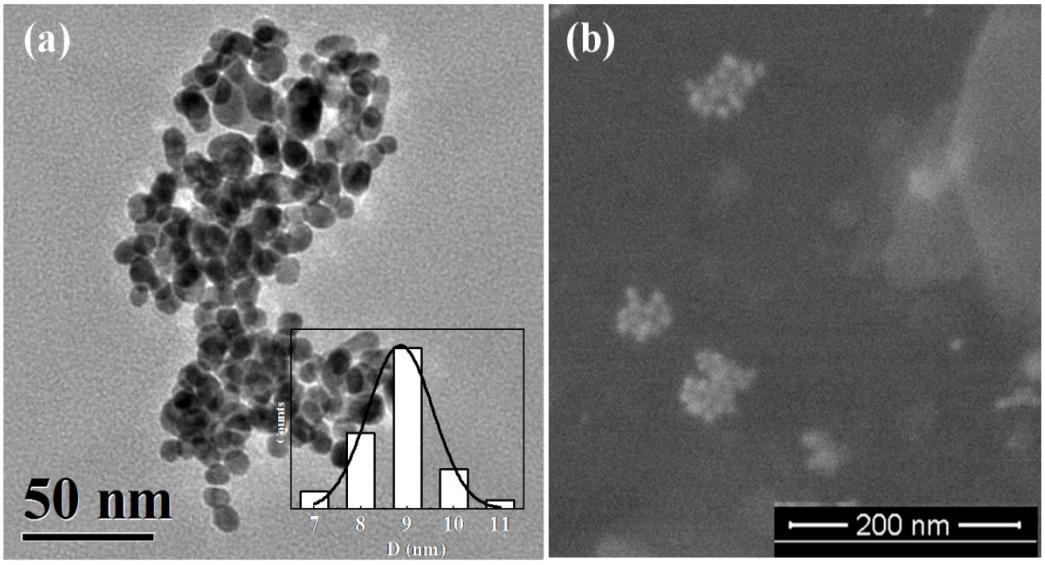

Figure 5.1 (a) TEM image with particle size distribution in inset, and (b) FESEM image of Au nanoparticle synthesized in-situ in polymer matrices.

In Fig. 5.2, we show the SAXS data of the Au-PVA films where the scattering intensity is plotted as function of the scattering factor. The scattering factor, *q*, and the inter-particle distance, *d* values for the films with different proportion of Au nanoparticles are shown in Table 5.1. The inter particle distance is calculated using the formulae $d=(2\pi/q)$. We observe three peaks in the SAXS which we believe could arise for the particles in cubic close packing (ccp). Accordingly, the ratio of the distances d_1/d_2 and d_1/d_3 obtained from the peak position are 2 and 3 respectively which can be approximated to the d_{111}/d_{222} and d_{111}/d_{422} ratio for the ccp structure. Such packing has been reported on self assembled Au nanoparticles [28-29].

From the SAXS we can obtain corresponding 2Θ values from

$$\sin\theta = {}^{q\lambda}/_{4\pi} \qquad (1)$$

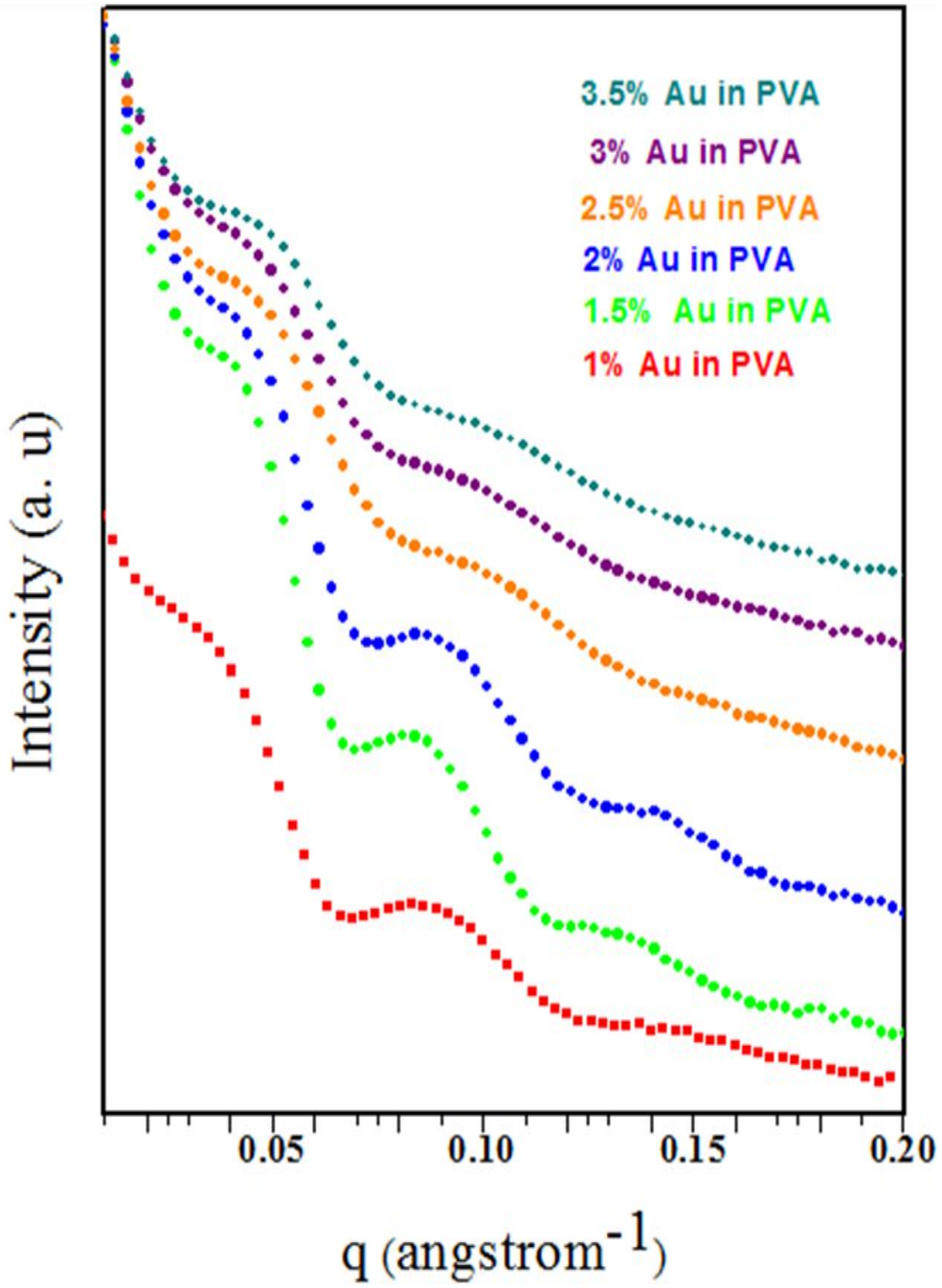

Figure 5.2 *q* vs intensity plot for various concentrations of Au nanoparticles in Au-PVA nanocomposites obtained from SAXS. Weight % of Au nanoparticles is shown against each curve.

Table 5.1 *q* and *d* values obtained from SAXS measurements and corresponding absorption maxima. Ratio of different d-values obtained from SAXS is also listed.

	From SAXS								*From UV-vis*
Au % in PVA	q_1 ($Å^{-1}$)	Distance (nm) d_1	q_2 ($Å^{-1}$)	Distance (nm) d_2	d_1/d_2	q_3 ($Å^{-1}$)	Distance (nm) d_3	d_1/d_3	λ max (nm)
1	0.038	16.7	0.086	7.3	2.2	0.138	4.6	3.6	546
1.5	0.041	15.2	0.081	7.7	2.0	0.133	4.7	3.1	548
2	0.045	14	0.087	7.2	1.9	0.139	4.5	3.1	560
2.5	0.046	13.8	0.0896	7.0	2.0	0.1489	4.2	3.2	565
3	0.048	12.9	0.0924	6.8	1.9	0.159	4	3.1	579
3.5	0.051	11.6	0.0995	6.6	1.8	0.165	3.8	3.0	600

In Fig 5.3 we have plotted scattered intensity vs 2Θ for Au-PVA 1.5% of Au nanoparticles. The peaks obtained have been indexed. We can see that as expected (111), (222) and (420) reflections appear. The first peak observed in the curve has 2Θ value of 0.14° or d ~ 60 nm. This represents distances between two clusters of Au nanoparticles in PVA.

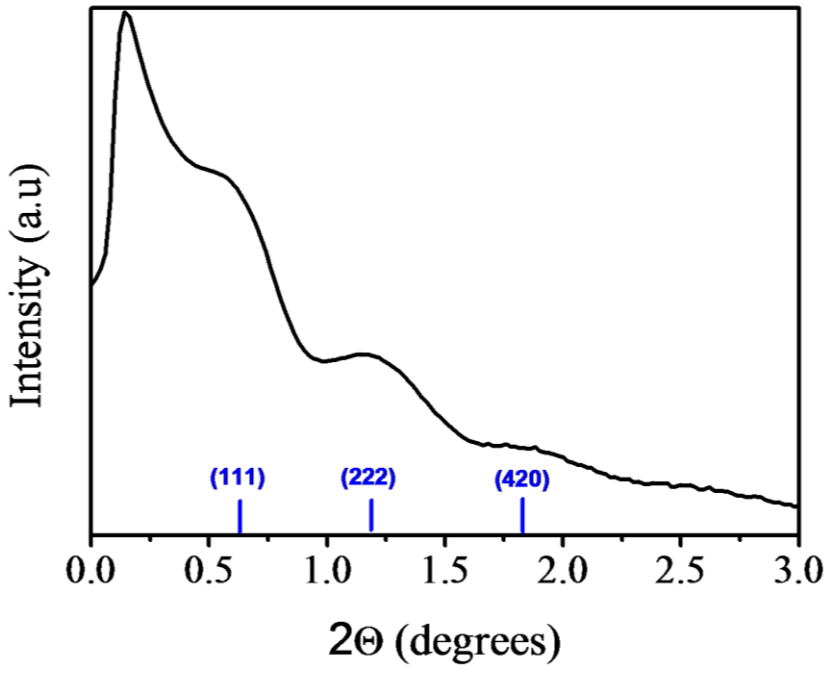

Figure 5.3 Plot of intensity vs 2Θ for Au PVA film with 1.5% of Au nanoparticles

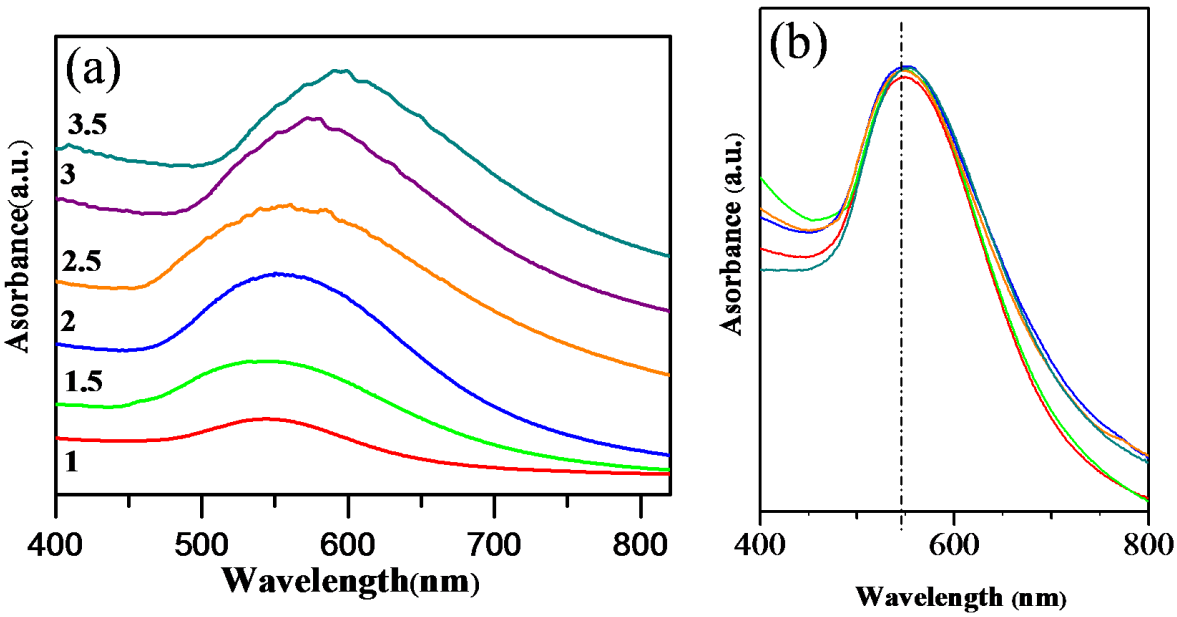

Figure 5.4 (a) Electronic absorption spectra of Au-PVA films with different weight%of Au nanoparticles. (b) The spectra of films dissolved in water.

Electronic absorption spectra of Au-PVA films of different compositions are shown in Fig. 5.4(a). We observe a continuous red shift in the absorption maximum of the SPR band with the change in concentration of the Au nanoparticles. The composite containing the highest concentration of Au nanoparticles has the maximum red shift with an absorption band centred around 600 nm. When the concentration of Au nanoparticles is least in the polymer nanocomposites, the SPR band occurs at the lowest wavelength since the interparticle distance would be largest corresponding to least dipolar plasmon coupling. At lower concentrations the value of SPR band is close to that of isolated particles in solution. As the concentration is increased, the particles come near to each other leading to more intensive coupling and hence consequent shifting of the plasmon absorption to longer wavelength. The SPR band positions of the Au-PVA nanocomposites are listed in Table 1. Fig. 5.4(b) shows the electronic absorption spectra of solutions of Au-PVA as constant with absorption maxima of 545 nm. This is because the band in solution medium is close to that of isolated Au nanoparticles of 9 nm diameter.

We have plotted the fractional plasmon shift $\Delta\lambda/\lambda_0$ as a function of increasing distance d_1 (first peak obtained in SAXS) in Fig. 5.5. The curve follows universal scaling of the

distance decay of plasmon coupling. The data was fitted to exponential decay the equation,

$$\Delta\lambda/\lambda_0 = A_0 \exp(^{-d/D}/\tau) \qquad (2)$$

where $\Delta\lambda$ is the shift in plasmon band from that for isolated Au nanoparticles (λ_0), A_0 and τ are constants (τ is called the decay constant), d is the interparticle separation and D the diameter of particle [21]. The red curve is the least-squares fit to single-exponential decay equation (2) with D= 9 nm. The R^2 value for the fit is 0.974.

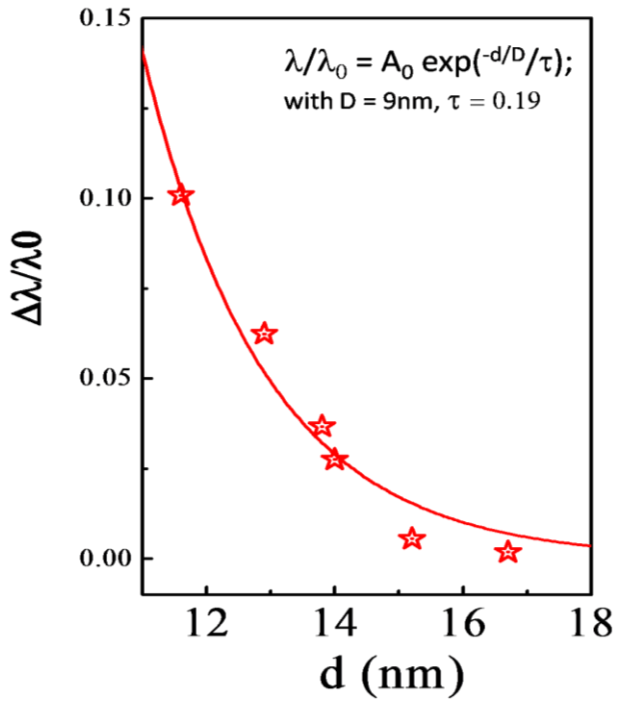

Figure 5.5 Plot of variation of relative shift in plasmon maxima as a function of inter-particle distance calculated from SAXS with the fitted curve.

The value of τ is 0.19, which agrees well with that found for lithographically fabricated Au nanoparticles (~ 0.2) [21]. Gunnarson *et al.* [31] estimated the decay constant of Ag nanodisc pairs to be ~ 0.22. Interestingly, the above equation holds good for the other distances obtained from SAXS data as well, shown in inset in Fig. 5.6. The decay length l obtained from equation,

$$y = y_0 + a.\exp(^{-d/D}/l) \qquad (2)$$

is 1.74 which is around 0.2 times that of the particle size (9 nm). This is in agreement with values reported by Jain *et al.*

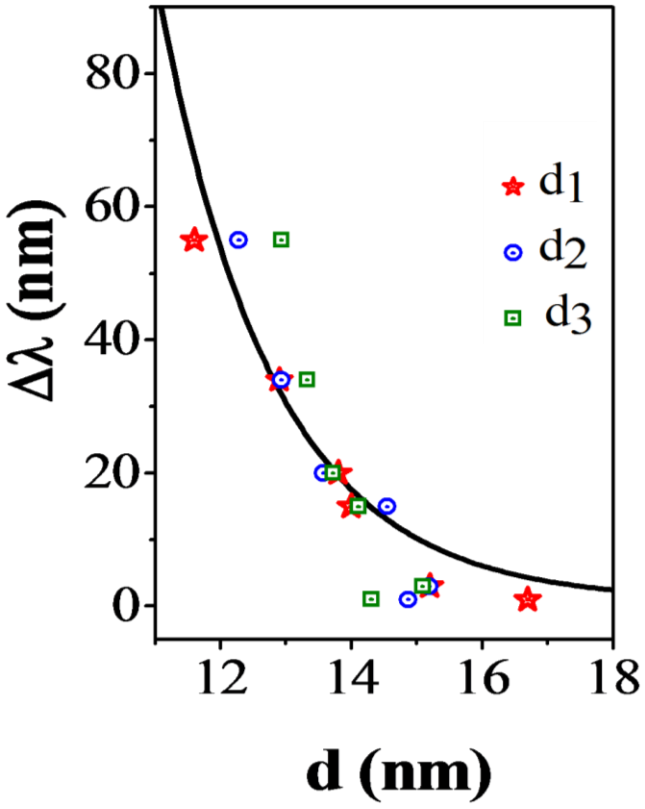

Figure 5.6 A plot of variation of shift in plasmon maxima vs. all the distances scaled as d_1, d_2×2 and d_3×3 with the fit.

5.5 Conclusions:

In conclusion we have demonstrated that Au nanoparticles and clusters embedded in polymer matrix show variation of SPR band with concentration. This results from the fact that intensity of plasmon coupling varies with concentration of Au in polymer matrix. It is noteworthy this variation of SPR band position can be described by a simple scaling law. The study establishes the universality of scaling behavior of plasmon coupling in metallic nanoparticles and allows for use of this scaling equation as a plasmon ruler to determine inter particle separation.

Reference:

[1] S. Schultz, D. R. Smith, J. J. Mock, D. A. P. Schultz, *Proc. Natl. Acad. Sci. U.S.A.* **2000**, 97, 996.

[2] Y. W. C. Cao, R. C. Jin, C. A. Mirkin, *Science* **2002**, 297, 1536

[3] L. Novotony, R. X. Bian, X. S. Xie, *Phys. Re*V. *Lett.* **1997**, 79, 645.

[4] N. Calander, M. Willander, *Phys. Re*V. *Lett.* **2002**, 89, 143603.

[5] P. C. Chaumet, A. Rahmani, M. Nieto-Vesperinas, *Phys. Re*V. *Lett.* **2002**, 88, 13601.

[6] H. X. Xu, M. Ka¨ll, *Phys. Re*V. *Lett.* **2002**, 89, 24802.

[7] S. Nie, R. Emory, *Science* **1997**, 275, 1102.

[8] K. Kneipp, Y. Wang, H. Kneipp, L. T. Perelman, I. Itzkan, R. Dasari, M. S. Feld, *Phys. Re*V. *Lett.* **1997**, 19, 1667.

[9] H. Xu, E. J. Bjerneld, M. Ka¨ll, L. Bo¨rjesson, *Phys. Re*V. *Lett.* **1999**, 83, 4357.

[10] S. Nie, S. R. Emory, *Science,* **1997**, 275, 1102.

[11] S. R. Emory, S. Nie, *Anal. Chem.*, **1997**, 69, 2631.

[12] K. H. Su, Q. H. Wei, X. Zhang, J. J. Mock, D. R. Smith, S. Schultz, *Nano Lett.* **2003,** 3 , 1087.

[13] P. K. Jain, W. Qian, M. A. El-Sayed, *J. Phys. Chem. B* **2005,** 110, 136.

[14] W. Rechberger, A. Hohenau, A. Leitner, J. R. Krenn, B. Lamprecht, F. R. Aussenegg, *Optics Commun.* **2003,** 220, 137.

[15] J. Aizpurua, G. W. Bryant, L. J. Richter, F. J. García de Abajo, B. K. Kelley, T. Mallouk, *Phys. Rev. B* **2005,** 71, 235420.

[16] F. Seker, P. R. L. Malenfant, M. Larsen, A. Alizadeh, K. Conway, A. M. Kulkarni, G. Goddard, R. Garaas, *Adv. Mater.* **2005,** 17, 1941.

[17] S. Lin, M. Li, E. Dujardin, C. Girard, S. Mann, *Adv. Mater.* **2005,** 17, 2553.

[18] J. J. Storhoff, A. A. Lazarides, R. C. Mucic, C. A. Mirkin, R. L. Letsinger, G. C. Schatz, *J. Am. Chem. Soc.* **2000,** 122, 4640.

[19] C. Sonnichsen, B. M. Reinhard, J. Liphardt, A. P. Alivisatos, *Nat. Biotechnol* **2005,** 23, 741.

[20] B. M. Reinhard, S. Sheikholeslami, A. Mastroianni, A. P. Alivisatos, J. Liphardt, *Proc. Natl. Acad.Sci*. **2007,** 104, 2667.

[21] P. K. Jain, W. Huang , M. A. El-Sayed, *Nano Lett.* **2007,** 7, 2080.

[22] W. Huang, W. Qian, P. K. Jain, M. A. El-Sayed, *Nano Lett.* **2007,** 7, 3227.

[23] P. K. Jain, M. A. El-Sayed, *Nano Lett.* **2007,** 7, 2854 .

[24] P. K. Jain, M. A. El-Sayed, *J. Phys. Chem. C* **2007,** 111,17451.

[25] P. K. Jain, M. A. El-Sayed, *J. Phys. Chem. C* **2008,** 112, 4954.

[26] J. Turkevich, P. C. Stevenson, J. Hillier, *Discuss. Faraday Soc.* **1951,** 11, 55.

[27] J. Kimling, M. Maier, B. Okenve, V. Kotaidis, H. Ballot, A. Plech, *J. Phys. Chem. B* **2006,** 110,15700.

[28] E. S. Shibu, K. Kimura, T. Pradeep, *Chem. Mater.* **2009,** 21, 3773.

[29] J. Zhuang, H. Wu, Y. Yang, Y. C. Cao, *J. Am. Chem. Soc.* **2007,** 129,14166.

[30] J. Zhuang, H. Wu, Y. Yang, Y. C. Cao, *Angew. Chemie Int. Ed.* **2008,** 47, 2208.

[31] L. Gunnarsson, T. Rindzevicius, J. Prikulis, B. Kasemo, M. Ka¨ll, S. Zou, G. C. Schatz *J. Phys. Chem. B* **2005,** 109, 1079.

CHAPTER 6

White-light emission from mixtures of GaN and ZnO nanoparticles

*Summary**

ZnO nanoparticles exhibit a broad band centred around 530 nm in the photoluminescence (PL) spectrum due to the presence of oxygen vacancies. This lies in the geen-yellow region of visible spectrum. GaN nanoparticles give its characteristic blue band edge emission in the region 404 nm. These ZnO and GaN nanoparticles when mixed in the ratio 3:1 exhibit white light emission. The quantum yields of these GaN-ZnO nanoparticle based white light sources are in the ~6.4±0.2 % range.

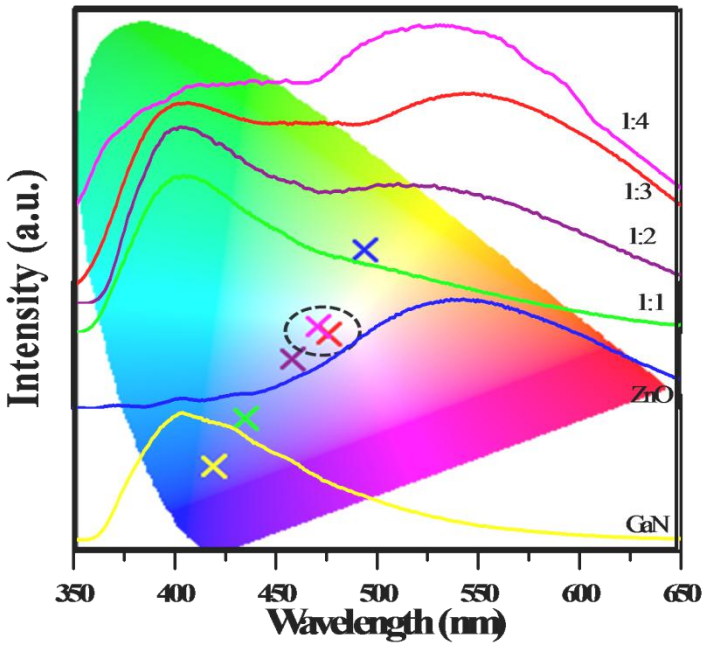

White light emission from mixtures of GaN-ZnO nanoparticles

**** A paper has been submitted for publication.***

6.1 Introduction:

In the recent years solid-state lighting technology has attracted attention as a viable and environment friendly alternative for incandescent lights. This is because it offers to save energy by producing light more efficiently. One major obstacle is producing true white light using these solid state lighting systems. The major techniques for fabricating semiconductor-based white-light devices use phosphors to convert UV or blue LED output into longer-wavelength colours to mix to form white light [1,2] . So far, the most widely used phosphor is cerium-doped yttrium aluminium garnet (YAG:Ce), which can effectively convert blue light at wavelengths around 460nm into yellow light near 560nm [3]. Because of the broad spectrum of YAG:Ce emission and the two-colour nature of such an LED, however, the colour-rendering index is not high. The conversion efficiencies of the phosphors are not very high. For this reason, technologies that avoid phosphors deserve intensive study [4].

Another approach is to use semiconductor nanocrystals such as say cadmium selenide (CdSe) core surrounded by a zinc sulfide (ZnS) shell that can convert short wavelengths to longer ones. Such crystals can effectively absorb UV-green light and emit green-red light. The absorption and emission spectra of these NCs can be tuned by controlling the diameter of the CdSe core and the thickness of the ZnS shell. Moreover, the NCs have the advantages of high quantum efficiency and photostability [5-6]. However Cd being highly toxic might seriously limit the application of such systems into practical devices.

Since the discovery of blue light emitting diodes by Nakamura, GaN has attracted much attention. GaN being a direct band gap semiconductor (with a bandgap of 3.4 eV), is thermally and environmentally stable and is also nontoxic. Ultraviolet or blue lasers and even high temperature-high power electronic devices based on GaN have become popular [7]. In general GaN based optoelectronic devices are fabricated as thin films on Si or SiC substrates by metal-organic vapor phase epitaxy [8], molecular beam epitaxy [9], or metal organic chemical vapor deposition [10,11]. High temperature processing of GaN films makes it difficult for use in applications involving large areas. GaN nanocrystals being nontoxic and air stable are ideal for use in LEDs.

GaN based large area LEDs have been fabricated by employing a combination of GaN nanocrystals with conjugated polymers [12].

ZnO is a unique electronic and photonic n-type semiconductor with a band gap of 3.37 eV and a fairly high exciton binding energy (60 meV) at room temperature [13, 14]. The lack of a centre of symmetry in wurtzite, combined with a large electromechanical coupling, results in piezoelectric and pyroelectric properties and the consequent use of ZnO in mechanical actuators and piezoelectric sensors. ZnO also exhibits a variety of other properties such as field emission and lasing [15]. Defects in ZnO give rise to characteristic bands in the photoluminescence spectrum causing a peak in green-yellow region. By taking suitable materials in combination with ZnO, it should therefore be possible to generate white light. There has been some effort in this direction, but many of these studies are incomplete [16, 17].

A mixture of blue emitting GaN and green-yellow emitting ZnO should therefore give us white light. With this in mind we have investigated PL spectra of nanocrystals of GaN and ZnO and mixtures of GaN-ZnO with various ratios of each nanoparticle. GaN-ZnO mixtures exhibit a high quality white light with good CIE coordinates along with an excellent colour rendering index.

6.2 Experimental Section:

ZnO nanoparticles with an average size of 4-5 nm were prepared by a procedure described in the literature [18]. The method involves hydrolysis of zinc acetate in methanol using KOH. In a typical synthesis, zinc acetate (0.01 mol) was dissolved in methanol (125 ml) under vigorous stirring at about 333 K. Subsequently, a solution of KOH (0.03 mol, 65 ml) in methanol was added drop wise at 333 K. The reaction mixture was stirred for 6 h at 333 K. The white precipitate thus obtained was harvested by centrifugation and washed thoroughly with ethanol and air-dried at 313 K.

GaN nanoparticles were synthesized [19] by decomposition of single source precursor, gallium-urea complex $[Ga(H_2NCONH_2)_6]Cl_3$. To prepare gallium-urea complex 2 g gallium oxide was first dissolved in conc. HCl to give $GaCl_3$, and the

excess HCl was removed by heating. A solution of 15.37 g of urea in isopropanol was then added to $GaCl_3$ and stirred for 2 hours. Thus obtained white precipitate was then filtered and washed. GaN nanocrystals were synthesized by decomposition of the complex at 600ºC in NH_3 atomsphere for two hours.

GaN-ZnO mixtures with GaN:ZnO from 1:1 to 1:5 were prepared to study emission properties. These mixtures were simply prepared by taking simply taking required amount of GaN and ZnO and grinding them thoroughly to get 6 mg of final powder. All the samples were examined by X-ray diffraction using Cu-K_α radiation (λ = 1.54056 Å) using a Rigaku-99 instrument. The morphology of the samples were studied by using a field emission scanning electron microscope (FESEM - FEI NOVA NANOSEM 600) and a transmission electron microscope (TEM - JEOL JEM 3010) images. UV–Vis absorption spectra were recorded using a Perkin-Elmer Lamda 900 UV/Vis/NIR spectrometer. Photoluminescence(PL) spectra were recorded with a Perkin-Elmer model LS55 luminescence spectrometer. Since dispersions of GaN were not very stable in ethanol or any other solvent PL spectra was taken for solid sample. It was ensured that equal amount of sample were taken for the measurements.

6.3 Results and Discussion:

ZnO nanoparticles synthesized were 5nm in diameter. Monodisperse ZnO nanoparticles were produced. TEM image of synthesized ZnO nanoparticles is shown in Fig. 6.1(a) with particle size distribution in the inset. The high resolution TEM and electron diffraction pattern show that synthesized ZnO is highly crystalline. GaN nanoparticles synthesized by us were also highly crystalline. Fig 6.2(a) shows the TEM image of GaN nanocrystals. Particle size is around 20-30 nm. Since this method of synthesis requires heating at high temperatures the particles are slightly agglomerated as seen in the TEM images. However higher temperatures are needed to make crystalline particles.

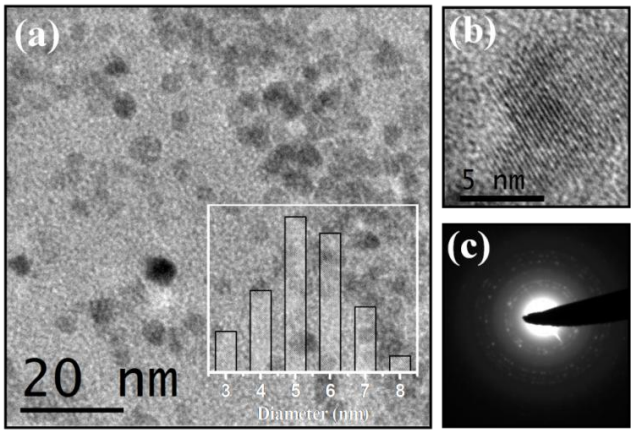

Figure 6.1 (a) TEM image of ZnO nanoparticles with particle size distribution as the inset, (b) HRTEM image, (c) ED pattern of ZnO nanoparticles.

Crystallinity is important in the present case because emission properties are highly sensitive to crystallinity. Intensity of band edge emission of GaN reduces dramatically if the sample is not very crystalline. The electron diffraction pattern shown in the inset of Fig. 6.2(b) shows that synthesized GaN Nanocrystals were highly crystalline. High resolution TEM image of GaN nanocrystals is shown in Fig. 6.2(b). The lattice fringes show a spacing of 2.8 A° due to the (100) planes of wurtzite GaN.

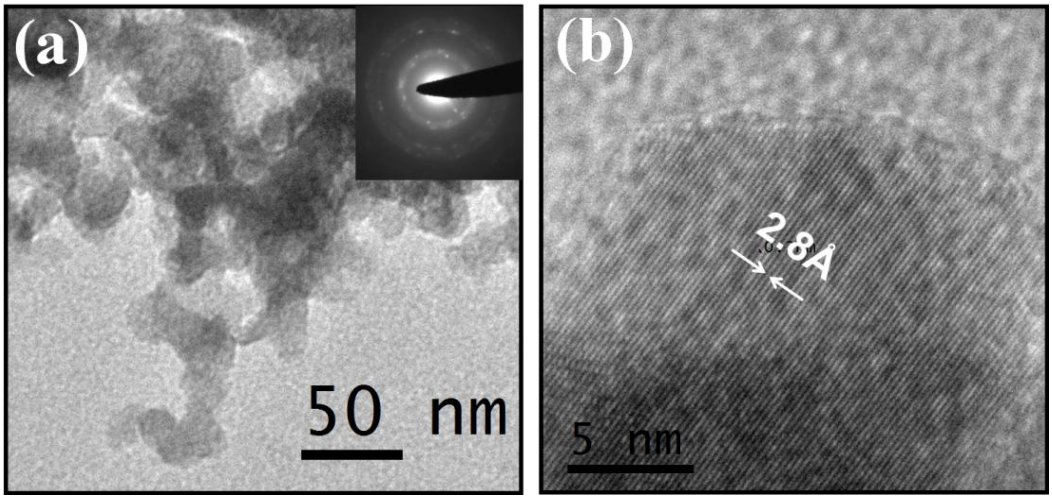

Figure 6.2 (a) TEM image of GaN nanocrystals with ED pattern in the inset, HRTEM image of the nanocrystals.

In Fig 6.3(a) we show the XRD pattern for ZnO and GaN. Both show expected peaks for wurzite structure. Absorption studies were carried out on the GaN and ZnO samples. Both show absorption edge at around 370 nm chareteristic of ZnO and GaN. Fig 6.3(b) shows electronic absorption spectra of GaN and ZnO.

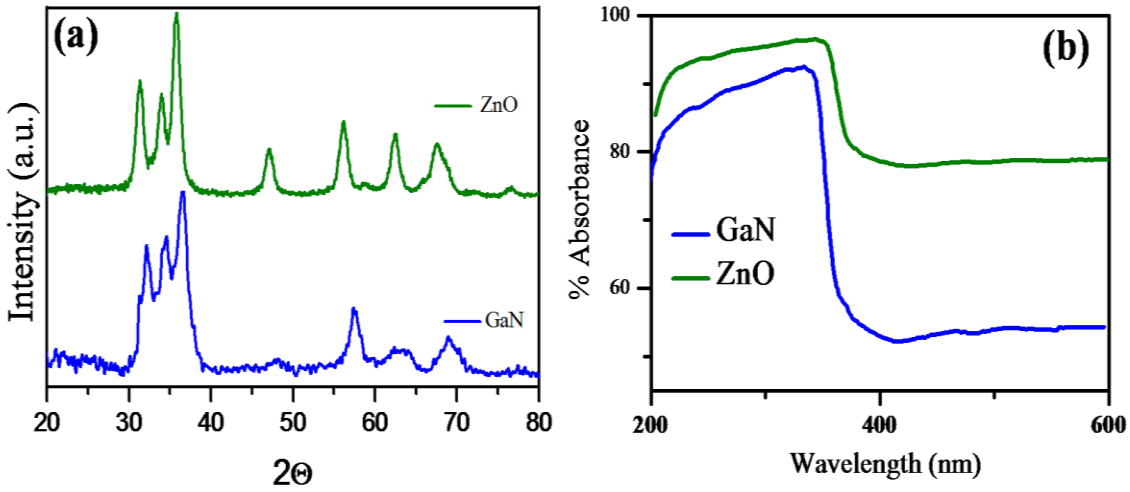

Figure 6.3 (a) XRD pattern and (b) electronic absorption spectra of GaN and ZnO Nanocrystals.

We first carried out PL measurements on the synthesized GaN and ZnO nanoparticles. All PL measurements were done with 325 nm excitation. GaN gave intense blue emission centered around 400 nm. While ZnO nanoparticles gave broad green-yellow luminescence band with an emission maxima around 545 nm (see Fig. 6.4(a)). The broad band originates from localized levels in the band gap. The most probable origin for the green emission in ZnO being the oxygen vacancies [20].This band in ZnO nanoparticles being of defect origin is sensitive to moisture and solvent. Therefore for all PL measurements either freshly prepared samples or samples well desiccated were used.

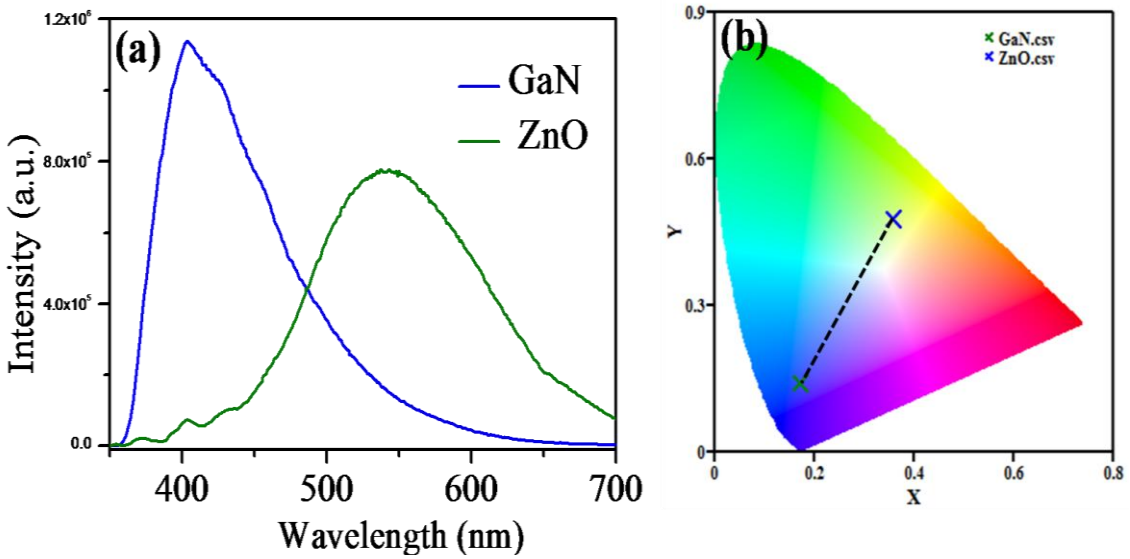

Figure 6.4 (a) PL emission spectra of ZnO and GaN (b) CIE color diagram for GaN and ZnO nanoparticles.

In Fig 6.4(b) is shown the CIE diagram for ZnO and GaN Nanocrystals. GaN lies in the deep blue region while ZnO in the green-yellow region of the spectrum. What is interesting is that the line joining the two passes very close to absolute white region. Thus mixtures of ZnO and GaN must yield white light.

With this knowledge we prepared mixtures of GaN and ZnO with GaN: ZnO ratios 1:1 to 1:5. In Fig 6.5 we have plotted the PL spectrum for GaN-ZnO mixtures with various ratios of each. Since intensity of green-yellow emission from ZnO is less intense as compared to blue emission from GaN, almost 3 times ZnO is needs to be mixed with GaN so as to cover the entire visible spectral region. The chromaticity diagram in Fig. 6.6 shows that white light is attained when GaN to ZnO weight ratio reaches 1:3. The CIE coordinates for various compositions are listed in Table as inset in Fig. 6.6. CIE co-ordinates of 1:3, 1:4 and 1:5 mixtures of GaN and ZnO show good white light characteristic. It is white with slight bluish tinge.

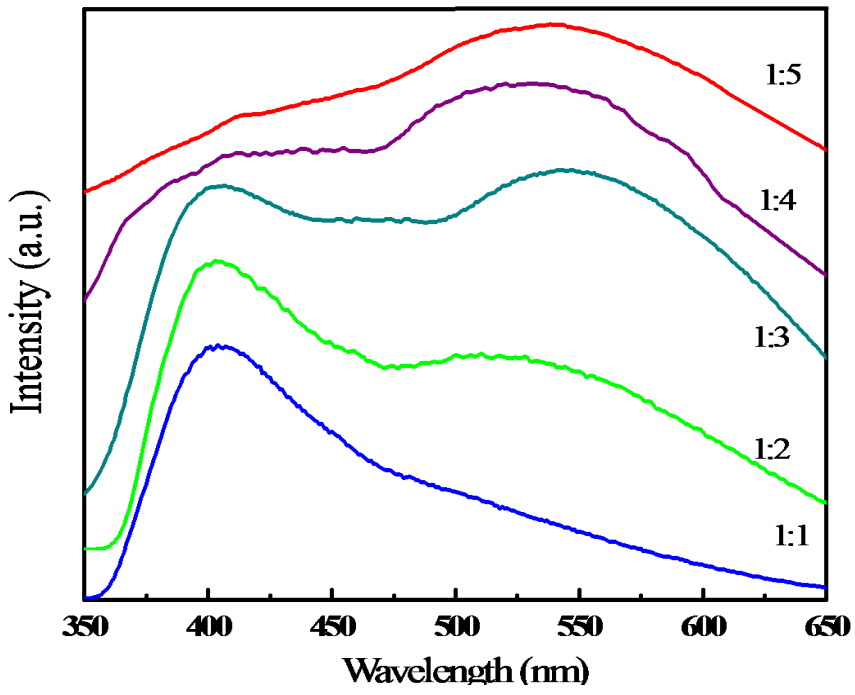

Figure 6.5 PL spectra of ZnO-GaN composites of various compositions.

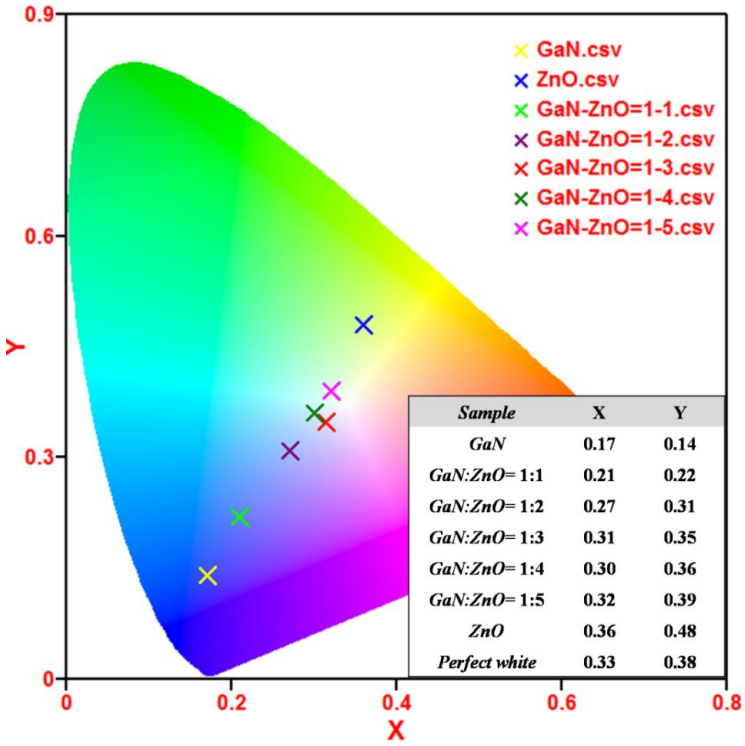

Sample	X	Y
GaN	0.17	0.14
GaN:ZnO= 1:1	0.21	0.22
GaN:ZnO= 1:2	0.27	0.31
GaN:ZnO= 1:3	0.31	0.35
GaN:ZnO= 1:4	0.30	0.36
GaN:ZnO= 1:5	0.32	0.39
ZnO	0.36	0.48
Perfect white	0.33	0.38

Figure 6.6 CIE diagram for GaN-ZnO composites of various composition with CIE co-ordinates of each listed in the table in inset.

For the various ZnO nanoparticle based materials; which emitted white light absorbance spectra were also recorded. Quantum yields for white light emission were calculated by the formula [21]:

$$\varphi_t = \varphi_s \frac{F_t}{F_s} \cdot \frac{A_s}{A_t} \cdot \left(\frac{n_t}{n_s}\right)^2 \quad (1)$$

where, *t* refers to the test sample, *s* refers to the standard sample, *F* denotes the area under PL intensity vs. wavelength curve, *A* stands for the absorbance and *n* for the refractive indices of the medium of dispersion, in the our case it was air**.** Quinine sulphate was used as the standard since it has UV excitation in the same range of wavelengths as the ZnO nanoparticle based materials. Moreover, the emission spectrum of quinine sulphate is in the same range as that of GaN- ZnO mixtures. Fig. 6.7 shows the UV-vis absorption spectra of the mixtures which emitted white light. All the mixtures have similar absorption. For comparison we have plotted the absorption spectra of quinine sulphate also.

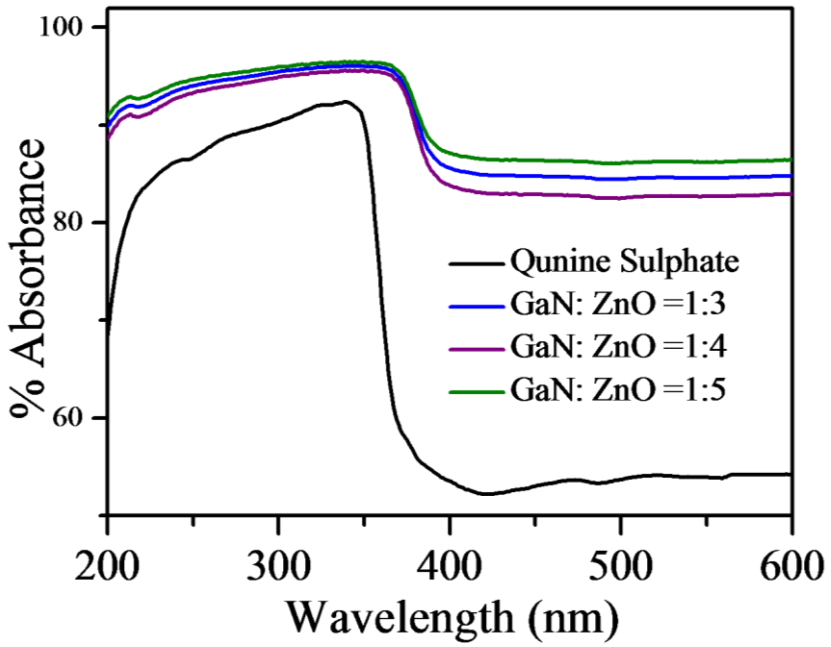

Figure 6.7 Electronic absorption spectra of mixtures of GaN-ZnO of various composition and quinine sulphate.

The quantum yield for quinine sulphate is 0.54 [in 0.1M H_2SO_4] for the spectral range of 400-600 nm [22]. Correction for the refractive indices (refractive index square dependence) of medium was incorporated in the calculations of quantum yields. For all the mixtures GaN-ZnO which emit white light the quantum yield was 6.4 ± 0.2%. These values of quantum yield are better than organic LEDs.

6.4 Conclusions:

It is significant that the PL band of ZnO nanoparticles originating from defects can be used to generate white light when mixed with materials with blue emission like GaN. The CIE co-ordinates represent high quality of white light produced. Quantum yield of the mixtures are also good. We have thus investigated simple mixtures of nanoparticles of GaN and ZnO as vaiable candidates for producing good quality white light. What is noteworthy is that such nanoparticles are easy to prepare and can thus be used as cheap and environment friendly sources for white light.

References:

[1] T. Mukai, S. Nakamura, *Oyo Buturi*, **1999**, 68, 152.

[2] S. Pimputkar, J. S. Speck, S. P.DenBaars, S. Nakamura *Nature Photonic* ,**2009,** 3,180.

[3] E.F. Schubert, *Light Emitting Diodes*, Cambridge University Press, **2006**.

[4] H. Masui, S. Nakamura, S.P. DenBaars, *Jpn. J. Appl. Phys*. **2006**,45, L910.

[5] S. Nakamura, *Science* **1998,** 281, 956.

[6] S. Nizamoglu, T. Ozel, E. Sari, H. V. Demir, *Nanotechnology* 18, pp. 065709, 2007.

[7] S.J. Pearten, F. Ren, *Adv. Mater.* **2000,** 12, 1571.

[8] F. Shaheddipour, B.W. Wessels, *Appl. Phys. Lett.* **2000,** 76, 3011.

[9] A.J. Steckl, M. Garter, D.S. Lee, J. Hekenfeld, R. Birkhahn, *Appl. Phys. Lett.* **1999,** 75 ,8184.

[10] J.M. Zawada, S.X. Jin, N. Nepal, J.Y. Lin, H.X. Jiang, P. Chow, B. Hertog, *Appl. Phys. Lett.* **1994,** 84, 1061.

[11] K. Wang, R.W. Martin, K.P. O'Donnell, V. Katchkanov, E. Nogales, K. Lorenz, E. Alwes, S. Ruffenech, O Briot, *Appl. Phys. Lett.* **2005,** 87, 112107.

[12] B. Chitara , S. V. Bhat , S.R.C. Vivekchand , A. Gomathi, C.N.R. Rao, *Solid State Communications* **2008**, 147, 409.

[13] Z. L. Wang **(2004)** *Mater. Today* 7, 26.

[14] C. N. R. Rao and A. Govindaraj, *Nanotubes and Nanowires,* In *The RSC Nanoscience & Nanotechnology series*, H. Kroto, P. O'Brien, H. Craighead Eds. Royal Society of Chemistry (London) **2005.**

[15] C. Klingshirn, *Chem Phys Chem*, **2007,** 8, 782.

[16] P. Thiyagarajan, M. Kottaisamy, N. Rama, M. Ramachandra Rao, *Scripta Materialia* **2008,** 59, 722.

[17] M. Willander, O. Nur, N. Bano and K. Sultana *New Jour. Phys.* **2009,** 11, 125020.

[18] C. Pacholski, A. Kornowski, H. Weller, *Angew. Chem. Int. Ed. Engl.* **2002**, 41, 1188.

[19] K. Sardar, M. Dan, B. Schwenzer, C.N.R. Rao, *J. Mater. Chem.* **2005,** 15, 2175.

[20] K. Vanheusden, W. L. Warren, C. H. Sesger, D. R. Tallant, J. A. Voigt, B. E. Gnage *J. Appl. Phys.* **1996,** *79,* 7983.

[21] P. Stephen , N. Rempel, *J Fluoresc.* **2006,** 16**,** 483.

[22] W.H. Melhuish, *J. Phys. Chem.* **1961,** 65**,** 229.

CHAPTER 7

Work in Progress

7.1 Magnetic properties of Au nanoparticles formed at the organic-aqueous interface

In 1999 Hori *et al.* observed magnetism in ~ 3 nm Au nanoparticles with unexpectedly large magnetic moments of about 20 spins per particle [1]. Since then several papers have reported magnetism in Au nanoparticles [2-6]. Origin ferromagnetism in Au nanoparticles however has remained a matter of controversy. In all these cases the synthesized nanoparticles stabilized using some capping agents like thiols and amines. Crespo et al. have shown by SQUID that gold NPs capped with weakly interacting reagents are diamagnetic, but those protected by thiolates become ferromagnetic due to 5d localized holes generated through Au-S bonding. In contrast, Hori and co-workers [6] have observed ferromagnetic spin coupling in weakly stabilized gold NPs, which has been ascribed to the ferromagnetic nature of the surface atoms due to the so-called Fermi hole effect. To elucidate the origin of magnetism, Negishi *et al.* [7] carried out x-ray circular dichroism study and tentatively concluded that a localized hole created by Au-S is responsible for the spin polarization of gold clusters. Thus it seems from these experiments that presence of thiol or amine capping agents are necessary for magnetic properties of Au nanoparticle. However Reich *et al.* [8] observed magnetism in 27 nm thin films of Au deposited on Pyrex glass. Thus arises the question, is presence of capping agent necessary for ferromagnetism of Au nanoparticles. To comprehend this we synthesized films of Au nanoparticles at the organic-aqueous interface without any capping agent and studied magnetic properties. We then used thiol capping agents on

these Au nanoparticles and compared the magnetic data obtained with that of films without capping agent.

Nanocrystalline films of gold were prepared using $Au(PPh_3)Cl$ (Ph = phenyl) and $Ag(PPh_3)_4NO_3$ as precursors by the literature procedure [9]. Tetrakishydroxymethylphosphonium chloride (THPC) was used as the reducing agent. In a typical preparation, 10 mL of a 1.5 mM solution of $Au(PPh_3)Cl$ in toluene was allowed to stand in contact with 16 mL of 6.25 mM aqueous alkali in a 100 mL beaker at room temperature. Once the two layers stabilized, 330 μL of 50 mM THPC solution in water was injected into the aqueous layer using a syringe with minimal disturbance to the toluene layer. The onset of reduction was marked by a faint pink coloration of the toluene–water interface. The reduction was allowed to proceed without disturbance for 12 hours. With the passage of time, the colour became more vivid, finally resulting in a robust elastic film at the liquid–liquid interface. To vary the particle size, the films were formed at different temperatures. Films with very small particles (~2nm) could be prepared using 80mM concentration of THPC as reducing agent. To obtain thiol capped nanoparticles few μmoles of dodecanethiol was added to the toluene layer. The film disappeared with colouration of the toluene layer. To see if any there is any additional effect of film on magnetism we prepared Au nanoparticles in aqueous solution using THPC as reducing agent. For this purpose 10 mL of 1.5 mM solution of $HAuCl_4.3H_2O$ in water was added to a mixture of 16 mL, 6.25 mM NaOH and 330 μL, 50 mM THPC under costant stirring [10]. Solid Au nanoparticles were precipitated from the hydrosol using excess of ethanol. Magnetic measurements were carried out in vibrating sample magnetometer in Physical properties measurement system, Quantum design, USA. All magnetic measurements were carried out with solid samples. During all synthesis steps care was taken to avoid contact with any metal.

Fig. 7.1 (a-d) are the TEM images of the films prepared at the organic-aqueous interface with 50 mM concentration of THPC as reducing agent. The particle size distribution of each is shown as inset. With increasing temperature particle size grows and thereby films with 10, 12, 13 and 15 nm were produced.

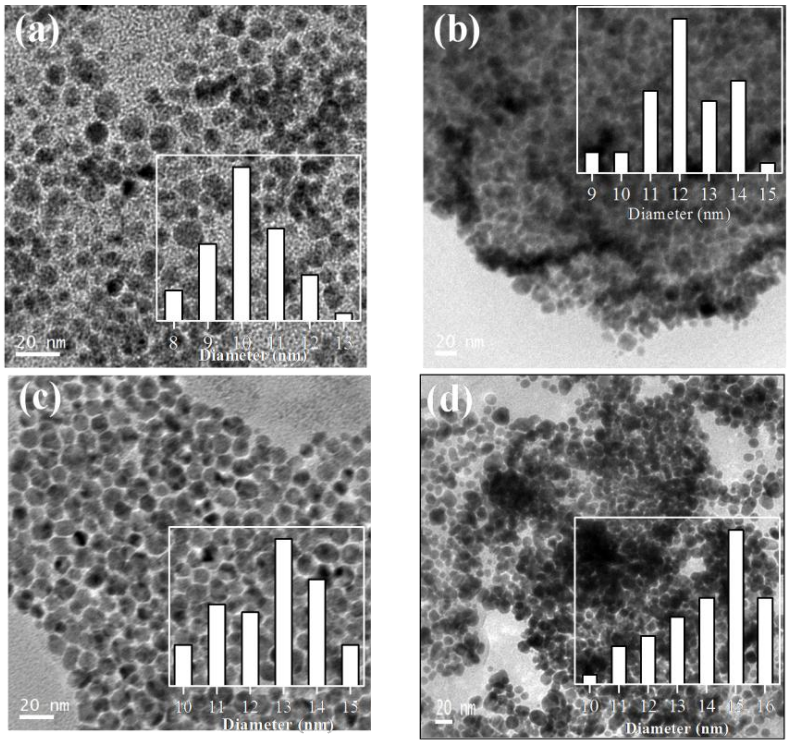

Figure 7.1 TEM images of films of Au nanoparticles formed at the organic-aqueous interface with 50 mM conc. of reducing agent.

With higher concentration of reducing agent (80 mM) smaller particles are produced. Fig. 7.2 is the TEM image of film with higher concentration of THPC with all other parameters remaining the same. Inset shows the particle size distribution. Pariticles are ~2.5 nm in size.

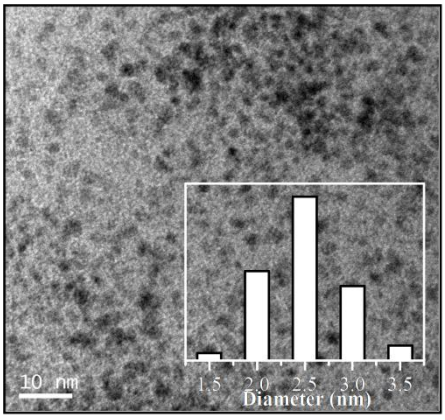

Figure 7.2 TEM image of Au nanoparticles formed at the organic aqueous interface with 80 mM conc. of reducing agent.

Room temperature magnetization data were collected for all these films For all the data collected we have substracted the diamagnic contribution from various sources like sample holder and Au diamagnetic core etc. The data after diamagnetic correction is

plotted in Fig. 7.3. To confirm all the measurements were repeated at least twice. With increasing particle size the saturation magnetization (Ms) value decreases. For films with particle size 2.5 nm the highest Ms value of 9.7×10^{-2} emu/g is reached.

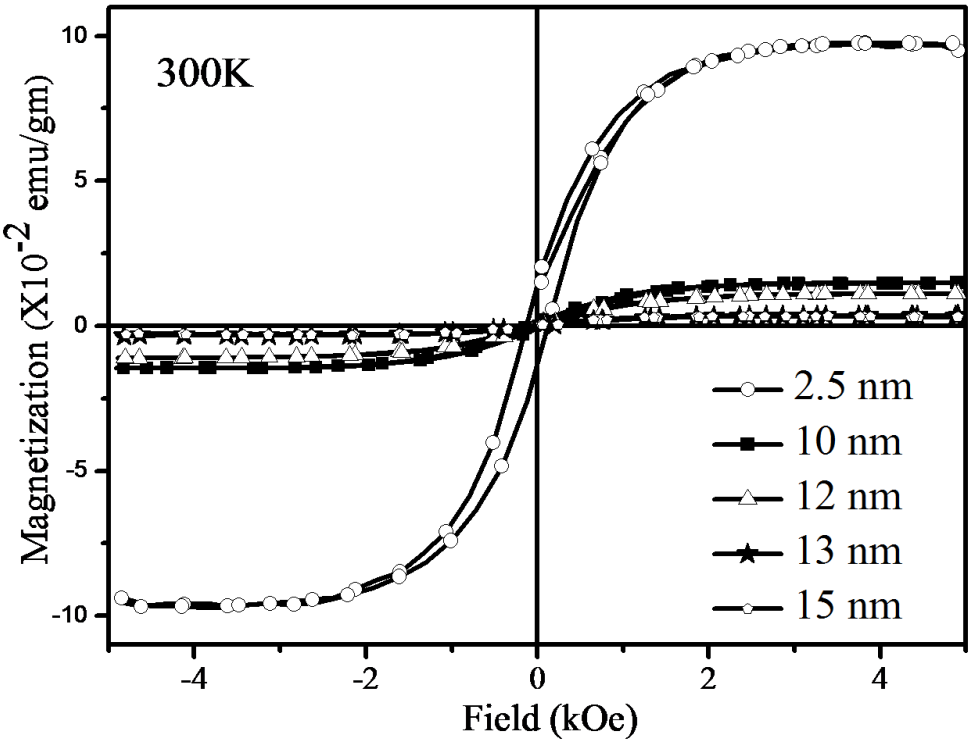

Figure 7.3 Room temperature M vs H plot of the Au films formed at the organic-aqueous interface

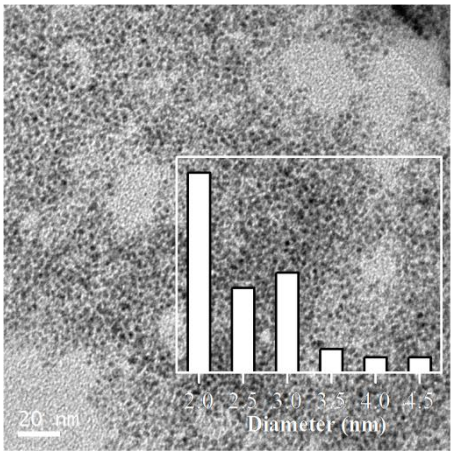

Figure 7.4 TEM image of Au nanoparticles in hydrosol with particle size distributions as inset.

To see if there is any added effect of films on magnetic properties we synthesized hydrosols of Au nanoparticles with similar concentrations of Au source ($HAuCl_4$) and reducing agent (THPC). Particles thus produced were ~ 2 nm in size. Fig. 7.4 shows the

TEM image with particle size distribution in the inset. Magnetization data of these particles are shown in Fig. 7.5. For comparison we have plotted the magnetization data of films with similar particle size.

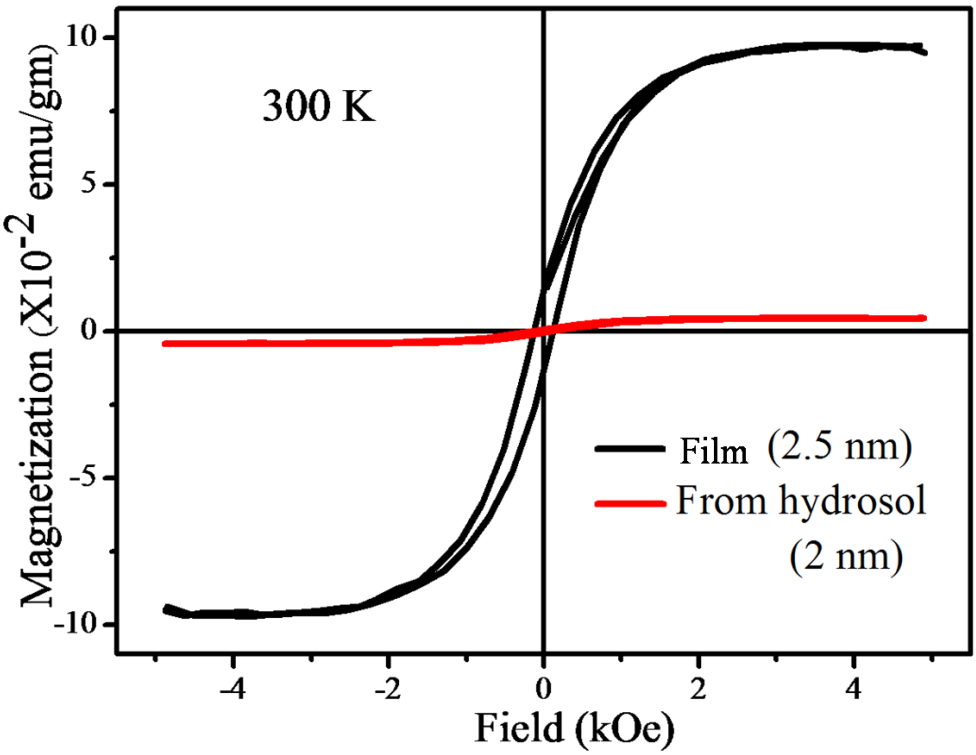

Figure 7.5 Room temperature M vs H plot for films and isolated particles of comparable size

We are preparing hydrosols of Au nanoparticles with different particle size to compare with films of other particle sizes. The effect of film formation on magnetism is yet to be understood.

We also prepared thiol capped Au nanoparticle of two particle sizes ~ 2nm and ~10nm. Magnetic properties of these were also studied. Fig 7.6(a) shows the room temperature magnetization data of these particles. For comparison we have plotted the data of particles of similar sizes with and without capping agents in Fig 7.6 (b) and (c). Thiol capping increases magnetization value slightly. We plan to study this in detail further.

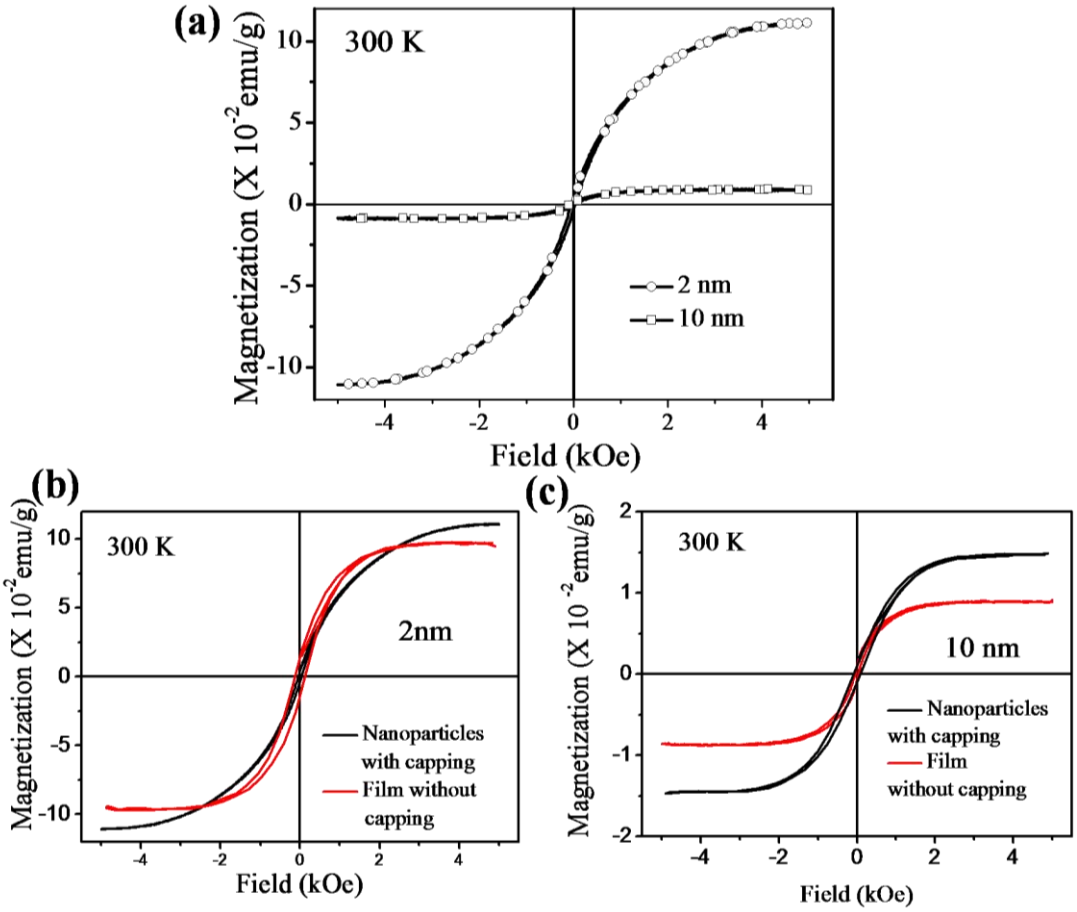

Figure 7.6 (a) Room temperature M vs H plot of thiol capped Au nanoparticles, Comparison of magnetization of Au nanoparticles of size (b) 2nm and (c) 10 nm with and without thiol capping.

We have thus studied magnetism of thin films of Au nanoparticle and compared the data with particles in hydsol and also thiol capped particles. Further study will be conducted on this problem so as to understand the origin of ferromagnetism in Au nanoparticles.

References:

[1] H. Hori, T. Teranishi, Y. Nakae, Y. Seino, M. Miyake, S. Yamada, *Phys. Lett. A.* **1999,** 263, 406.

[2] P. Crespo, R. Litra´n, T. C. Rojas, M. Multigner, J. M. de la Fuente, J. C. Sa´nchez-Lo´pez, M. A. Garcı´a, A. Hernando, S. Penade´s, A. Ferna´ndez, *Phys. Re*V. *Lett.* **2004**, 93, 087204.

[3] A. Hernando, P. Crespo, M. A. Garcı´a, *Phys. Re*V. *Lett.* **2006**, 96, 057206.

[4] C. Gonzalez, Y. Simon-Manso, M. Marquez, V. Mujica, *J. Phys. Chem. B* **2006**, 110, 687.

[5] Y. Yamamoto, T. Miura, M. Suzuki, N. Kawamura, H. Miyagawa, T. Nakamura, K. Kobayashi, T. Teranishi, H. Hori, *Phys. ReV. Lett.* **2004**, 93, 116801.

[6] H. Hori, Y. Yamamoto, T. Iwamoto, T. Miura, T. Teranishi, M. Miyake, *Phys. Re*V. *B* **2004**, 69, 174411.

[7] Y. Negishi, H. Tsunoyama, M. Suzuki, N. Kawamura, M. M. Matsushita, K. Maruyama, T. Sugawara, T. Yokoyama, T. Tsukuda, *J. Am. Chem. Soc.*, **2006**, 128, 12034.

[8] S. Reicha, G. Leitus, Y. Feldman, *Appl. Phys. Lett.* **2006,** 88, 222502.

[9] C.N.R. Rao, G.U. Kulkarni, P.J. Thomas, V.V. Agrawal, P. Saravanan, *J. Phys. Chem. B* **2003,** 107, 7391.

[10] D. G. Duff, A. Baiker, *Langmuir* **1993,** 9, 2301.

7.2 Covalently crosslinked binary composites of nanocarbons

One of the many things that determine their nature and properties or nanomaterials is dimensionality. Of the variety of nanomaterials synthesized and characterized in recent years, nanocarbons of different dimensionalities are of particular interest, as exemplified by nanodiamond, nanotubes and graphene with dimensionalities of zero, one, and two respectively Lot of research has gone into studying individual properties of these nanocarbons and modifying them to obtain desirable properties. Composites of nanocarbons with other metals, oxides, nitrides, polymers and many more have been studied and are still being pursued. We found extraordinary synergy in mechanical properties on adding two of these carbon nanofillers into polymer matrices. In this work we aim at covalently cross-linking two similar or different carbon nanostructures to prepare sandwich materials to get binary composites of carbon nanostructures. We aim to disperse these covalently crosslinked composites in polymer matrices to study the effect of covalently interacting nanocarbons filler moieties on mechanical properties.

There have been some reports in literature on covalent crosslinking of carbon nanotube. Chiu *et al.* [1] have been successful in linking two chloride terminated nanotubes via diamines. Frehill *et al.* [2] have linked two nanotubes via inorganic metal complxes. However there has not been any report so far on covalently combining two different nanocarbons. We aim prepare binary combinations of nanodiamond (ND), single walled carbon nanotube (SWNT) and graphene (G). To

date we have been successful in covalent linking of ND with G. We also linked by the similar mechanism ND with ND and G with G.

To do this we first funtionalized the carbon nanostructures to get acid groups on the surface. These acidic groups were then reacted with diamines to combine to nanostructure. We used DCC (Dicyclohexylcarbodiimide) coupling mechanism to enhance the reaction of acid functionalized moieties with diamines. In scheme 7.1 we have presented the schematics of the reaction.

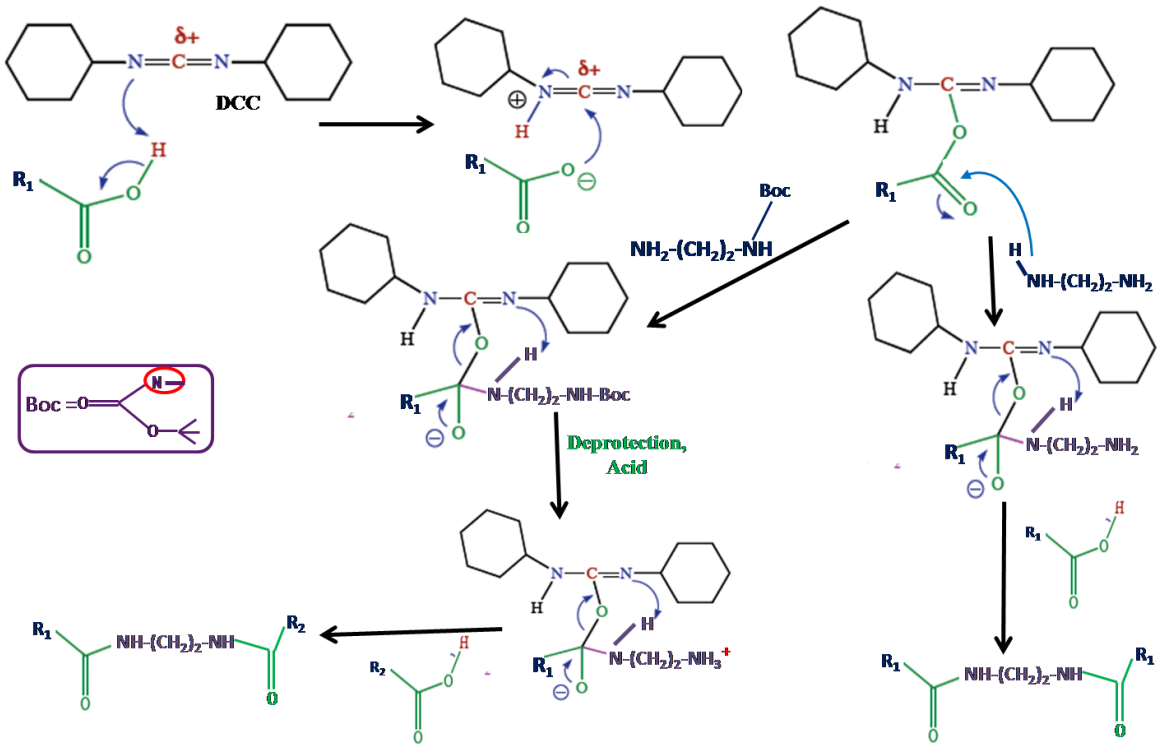

Scheme 7.1 Schematic of the reaction between two nanocarbons using DCC to enhance coupling.

***R_1 and R_2 represent two different nanocarbons; Boc = tert-butyl carbamate of alanine**.

Simple diamine like ethelyne diamine was used to link to similar nanocarbons moieties. To link two different nanocarbon moieties we used Boc protected ethylene diamine. Boc represents tert- butyl carbamate of alanine.

G and ND were first acid functionalized. For this 50 mg of each were treated with 2 ml of conc. HNO_3, 2ml of conc. sulphuric and 16 ml water in microwave. Acid treated nanocarbons were washed with water thoroughly and dried. 5 mg of each of

these were used for further reactions. To covalently link single nanocarbon moieties 5 mg of the nanocarbon was taken in 20 ml of DMF, sonicated well for 10 mins and then 1 mg of DCC and 1 ml of ethelyne diamine (ED) were added to it. Reaction was stirred for 4 hrs under inert atmosphere and later products were collected by centrifugation. It was washed several times with water, acetonitrile and ethanol and characterized.

To covalently link two different nanocarbons moieties instead of ethylene diamine Boc-protected ethylene diamine (Boc-ED) was used. 5 mg of one of the nanocarbons was first taken in DMF well sonicated and 1mg of each of DCC and Boc-ED were added to it under inert atmosphere with constant stirring. The reaction was allowed to go on for 4 hrs and the solvents were removed by centrifugation followed by one wash with 10 ml each of water, actonitrile and ethanol. The solid obtained was dispersed in DMF and 5 mg of other nanocarbons was added to it followed by sonication for 10 min. 3 ml of trichloroacetic acid was then added to this to deprotect the Boc-ED. Once deprotection of Boc-ED occurs the free $-NH_2^+$ group can now form amide bond easily with acid group of the other nanocarbon moiety. Thus the nanocarbon moieties must get covalently linked. The reaction was then stirred of 4 hrs followed by washing with water and ethanol. The product obtained was characterized by TEM, IR spectroscopy, Raman measurements and Photoluminescence spectroscopy.

The reactions of different nanocarbons can be described by the following equations.

$$\text{ND-A + DCC+ ED} \longrightarrow \text{ND-ED-ND} \quad (1)$$

$$\text{G-A + DCC + ED} \longrightarrow \text{G-ED-G} \quad (2)$$

$$\text{ND-A + DCC + Boc- ED} \longrightarrow \text{ND-EDBoc}$$

$$\text{ND-EDBoc} \xrightarrow{\text{de-protection with H+}} \text{ND-ED}^+$$

$$\text{G + DCC} \longrightarrow \text{G-DCC} \quad (3)$$

$$\text{ND-ED}^+ + \text{G-DCC} \longrightarrow \text{ND-ED-G}$$

where, ND-A and G-A represent acid treated samples and ND-ED-ND , G-ED-G represent final product of reactions single nanocarbons. ND-ED-G is used to represent product obtained after reacting nanodiamond with graphene.

In TEM images of the covalently linked nanocarbons are shown in Fig. 7.7.

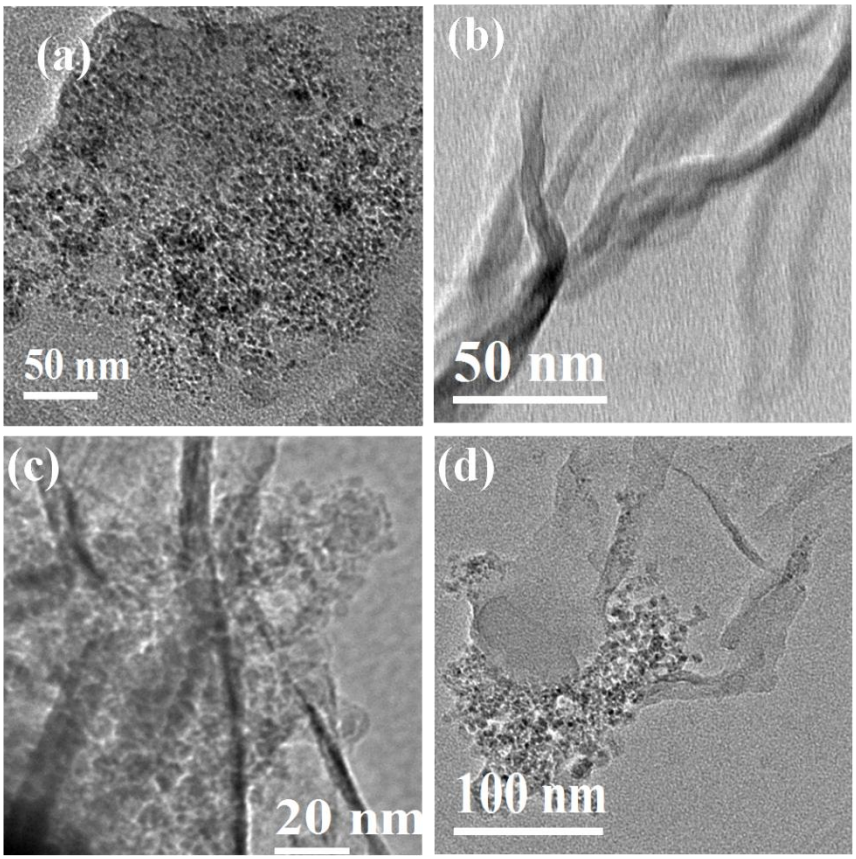

Figure 7.7 TEM image of the product (a) ND-ED-ND, (b) G-ED-G, (c) high magnification and (d) low magnification images of ND-ED-G

IR specta of the samples were recorded. Fig. 7.8 (a-c) show IR spectra of the products in comparison with starting material - acid treated nanocarbons. As is clear all the samples show distinct amide I and amide II peaks along with C-N stretching mode. O-H and N-H bond stretches can also be seen in the spectra. Some O-H can come from original acid treated samples getting partially functionalized with –OH functional groups on the surface. Other than these C-H stretches can also be recognized.

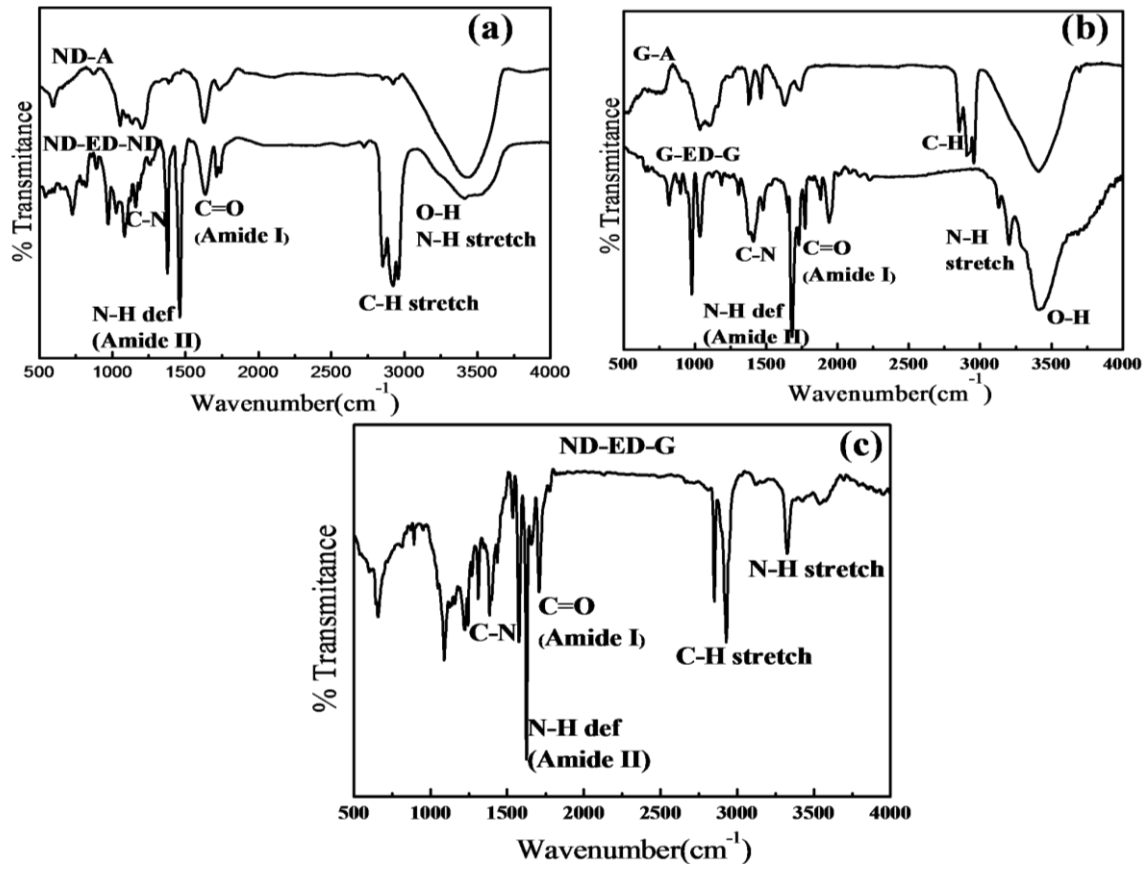

Figure 7.8 IR spectra of (a) ND-ED-ND with ND-A for comparison, (b) G-ED-G with G-A for comparison and (c) ND-ED-G.

All ND containing samples were characterized using PL spectroscopy. All samples show characteristic PL spectra of nanodiamond.

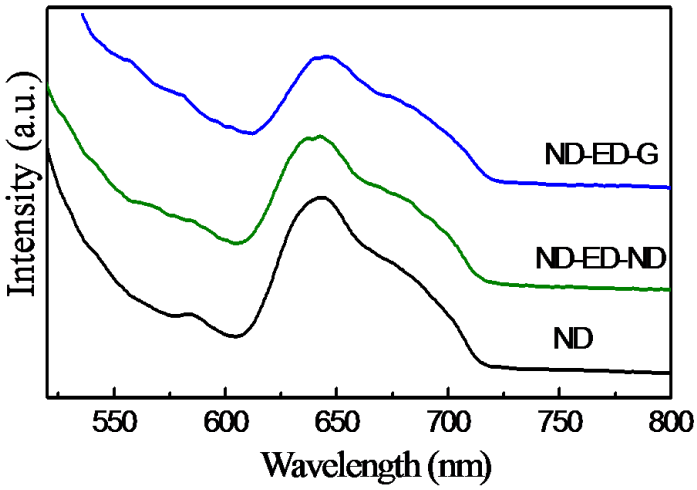

Figure 7.9 PL spectra of nanodiamond containing samples showing distinct PL spectra of ND.

In Fig. 7.10 we have plotted the Raman spectra of all the samples. For comparison we have also plotted the Raman spectra of acid treated nanodiamond and graphene.

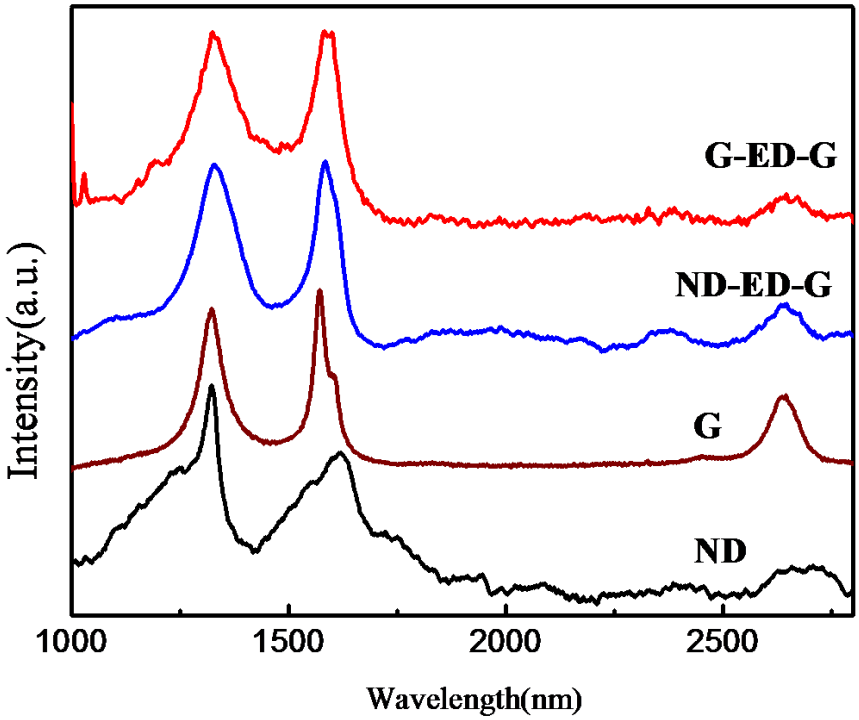

Figure 7.10 Raman spectra of the products obtained and of acid treated nanodiamond and graphene

Raman spectra show all characteristic G, D and 2D bands observed in case of graphene. It is well known that the D band also known as the defect induced band increases in intensity with introduction of defects in the graphene lattice. Keeping this in mind we compared the I_D/I_G ratios of all the samples. In Table 7.1 we have listed the I_D/I_G ratios of all the samples.

Table 7.1 Comparison of features of Raman spectra of all samples

	I_D/I_G	I_{2D}/I_G	λ_G (nm)	$\lambda_{G'}$ (nm)	$FWHM_G$ (cm^{-1})	$FWHM_{G'}$ (cm^{-1})
Graphene	0.9	0.43	1571	1605	33.8	20
Gr-ED-Gr	0.99	0.3	1580	1610	51.6	20.2
ND-ED-Gr	1.06	0.15	1581	1610	58.3	20.2

It is seen that on coupling I_D/I_G ratio increases. This indicates an increase in the defects in the Graphene lattice. Introduction of defects can be because of introduction of functional

groups on the surface. Again we see that I_{2D}/ I_G ratio decreases on coupling. Literature shows with charge transfer or by doping I_{2D}/ I_G decreases [3]. Because of amide linkage similar charge transfer can happen and thereby decrease I_{2D}/ I_G ratio. This is a clear proof of covalent linkage through amide bonds.

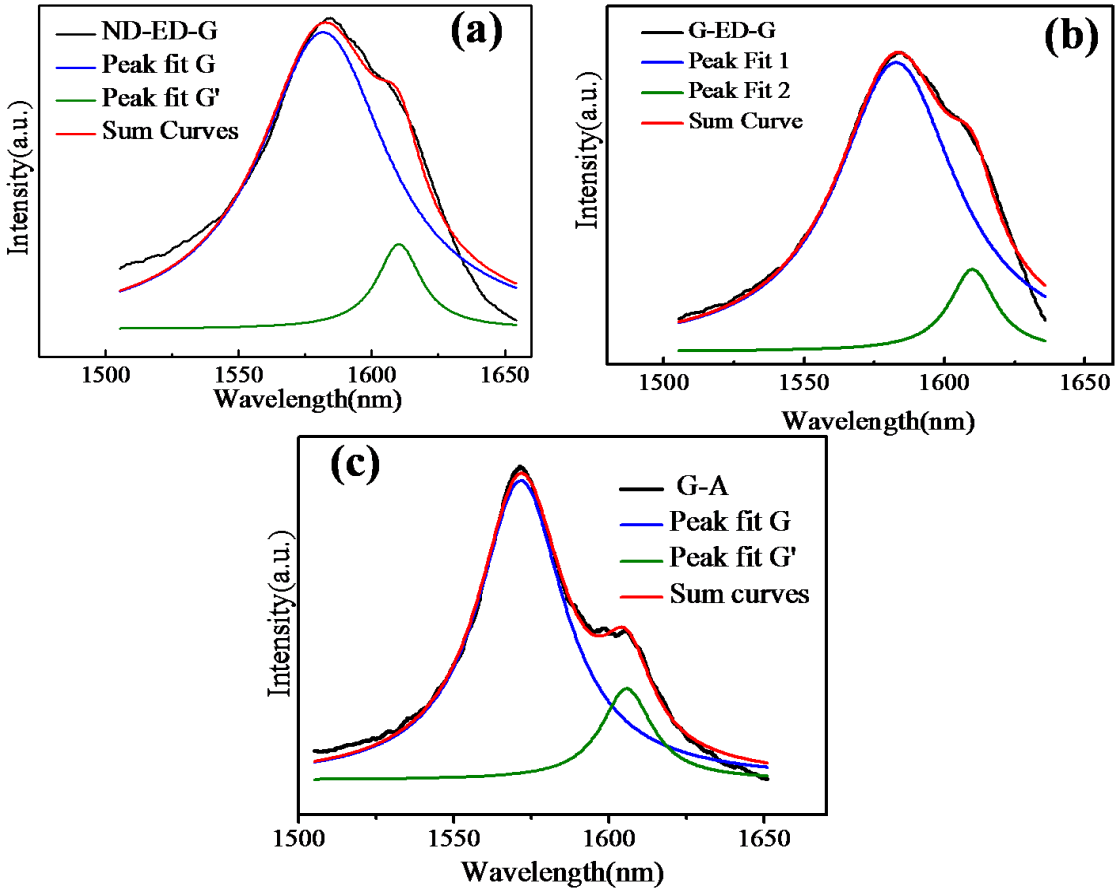

Figure 7.10 Peak fits for G and G' bands in Raman spectra of (a) ND-ED-G, (b) G-ED-G and (c) acid treated graphene

The G band in Raman spectrum of graphene can further be resolved into two bands G and G'. In Fig. 7.10 we have plotted the G and G' bands for all the samples containing graphene in them. It is clear that both G and G' bands shift considerably on coupling. While G band shifts by almost 10 nm for both the samples G' band shifts by 5nm (see Table 7.1). There is also a considerable increase in the peak width of G band but for G' the increase in width is minimal. In case of G-ED-G sample the peak width of G band increases by almost 18 cm^{-1} while for ND-ED-G sample it increases by almost 24 cm^{-1}. This again supports the fact that amide linkage has occurred.

We have thus successfully linked two nanocarbons covalently using simple amide bonds. We endeavor to achive the same with SWNT and graphene and SWNT and nanodiamond.

Reference:

[1] P. W. Chu, G. S.Duesburg, U. Dettlaff-Wegiikowska, S. Roth, *Appl. Phys. Lett.* **2002**, 80, 3811-3813.

[2] F. Frehill, J. G. Vos, S. Benrezzak, A. A. Koo´ s, Z. Ko´nya, M. G. Ru¨ther, W. J. Blau, A. Fonseca, J. B. Nagy, L. P. Biro´, A. I. Minett, M. in het Panhuis, *J. Am. Chem. Soc.* **2002**, 124, 13694.

[3] B. Das, R. Voggu, C. S. Rout, C. N. R. Rao, *Chem. Commun.*, **2008**, 5, 5155.